Development of glass optical fibers based on fluoride-phosphate for deep-UV optical transmission

**Thèse en cotutelle
Doctorat en chimie**

Gustavo Galleani

Université Laval
Québec, Canada
Philosophiae Doctor (Ph. D.)

et

Universidade Estadual Paulista "Júlio de Mesquita Filho"
Araraquara, Brasil
Doutorado

GUSTAVO GALLEANI

Development of glass optical fibers based on fluorophosphate for deep-UV optical transmission

Thesis in co-title with Université Laval – Quebec – Canada presented to the Institute of Chemistry, Universidade Estadual Paulista, to obtain the degree of Doctor in Chemistry

Brazilian advisor: Younes Messaddeq
Brazilian co-advisor: Silvia Helena Santagneli
Canadian advisor: Denis Boudreau

Araraquara

2017

unesp

UNIVERSIDADE ESTADUAL PAULISTA

Câmpus de Araraquara

CERTIFICADO DE APROVAÇÃO

TÍTULO DA TESE: "Development of glass optical fibers based on fluorophosphate for deep-UV optical transmission"

AUTOR: GUSTAVO GALLEANI
ORIENTADOR: YOUNES MESSADDEQ
COORIENTADORA: SILVIA HELENA SANTAGNELI
COORIENTADOR: DENIS BOUDREAU

Aprovado como parte das exigências para obtenção do Título de Doutor em QUÍMICA, pela Comissão Examinadora:

Prof. Dr. YOUNES MESSADDEQ
Departamento de Química Geral e Inorgânica / Instituto de Química - UNESP - Araraquara

VIDEOCONFERÊNCIA

Prof. Dr. DENIS BOUDREAU
Département de Chimie / Faculté des Sciences et de Génie - Université Laval - Québec

Prof. Dr. MARCELO NALIN
Departamento de Química Geral e Inorgânica / Instituto de Química - UNESP - Araraquara

Prof. Dr. HELLMUT ECKERT
Departamento de Físico-Química / Instituto de Química - USP - São Carlos

VIDEOCONFERÊNCIA

Prof. Dr. MARTIN BERNIER
Département de Physique / Faculté des Sciences et de Génie - Université Laval - Québec

UNIVERSIDADE ESTADUAL PAULISTA

Câmpus de Araraquara

VIDEOCONFERÊNCIA

Prof. Dr. THIERRY CARDINAL
Chimie et Photonique des Matériaux Oxydes et Fluorures / Institut de Chimie de la Matière Condensée de Bordeaux - Pessac - France

Araraquara, 09 de novembro de 2017

unesp

UNIVERSIDADE ESTADUAL PAULISTA

Câmpus de Araraquara

CERTIFICADO DE APROVAÇÃO

TÍTULO DA TESE: "Development of glass optical fibers based on fluorophosphate for deep-UV optical transmission"

AUTOR: GUSTAVO GALLEANI
ORIENTADOR: YOUNES MESSADDEQ
COORIENTADORA: SILVIA HELENA SANTAGNELI
COORIENTADOR: DENIS BOUDREAU

Aprovado como parte das exigências para obtenção do Título de Doutor em QUÍMICA, pela Comissão Examinadora:

Prof. Dr. YOUNES MESSADDEQ
Departamento de Química Geral e Inorgânica / Instituto de Química - UNESP - Araraquara

Prof. Dr. DENIS BOUDREAU
Département de Chimie / Faculté des Sciences et de Génie - Université Laval - Québec

Prof. Dr. MARCELO NALIN
Departamento de Química Geral e Inorgânica / Instituto de Química - UNESP - Araraquara

Prof. Dr. HELLMUT ECKERT
Departamento de Físico-Química / Instituto de Química - USP - São Carlos

Prof. Dr. MARTIN BERNIER
Département de Physique / Faculté des Sciences et de Génie - Université Laval - Québec

unesp UNIVERSIDADE ESTADUAL PAULISTA

Câmpus de Araraquara

Prof. Dr. THIERRY CARDINAL
Chimie et Photonique des Matériaux Oxydes et Fluorures / Institut de Chimie de la Matière Condensée de Bordeaux - Pessac - France

Araraquara, 09 de novembro de 2017

1. DATA

Name: Gustavo Galleani

Name in bibliographic citations: GALLEANI, G.

Adress: Universidade Estadual Paulista "Júlio de Mesquita Filho"

Instituto de Química

Departamento de Química Geral e Inorgânica

Rua Francisco Degni 55

Quitandinha – Araraquara – SP

CEP: 14800-900

Telefone: (16) 3301-9770

e-mail: gugalleani@yahoo.com.br

2. ACADEMIC EDUCATION.

2007-2011: Bachelor in chemistry
State of São Paulo University "Júlio de Mesquita Filho"
2011-2013: Master in Chemistry
State of São Paulo University "Júlio de Mesquita Filho"

3. BIBLIOGRAPHIC PRODUCTION.

3.1. Presentation in conferences:

Galleani, G.; Y. Ledemi; S. H. Santagneli; De Oliveira, M.; H. Eckert; Y. Messaddeq "**Ultraviolet upconversion luminescence and structural properties in triple-doped Gd^{3+}, Tm^{3+} and Yb^{3+} fluoride-phosphate glasses**", 2017. In: International Conference on Nanophotonics, Recife, Brazil

Galleani, G.; Y. Messaddeq; Y. Ledemi "**Fabrication of fluorophosphate glass fiber by the crucible method for transmission in the UV**", 2016. In: International OSA network of students, Quebec, Canada.

Galleani, G.; Y. Messaddeq; Y. Ledemi "**Ultraviolet upconversion luminescence properties of Yb^{3+}, Gd^{3+} and Tm^{3+} codoped fluorophosphate glasses**", 2016. In: Brazilian meeting on inorganic chemistry, Sao Pedro, Brazil.

Galleani, G.; Y. Messaddeq; Y. Ledemi "**Development of fluorophosphate glasses for optical fibers transmitting in the deep UV**", 2015. In: Journee du COPL, Montreal, Canada.

Galleani, G.; Manzani, D.; Ribeiro, S. J. L.; Nunes, L. A. O.; Pecoraro, E. **"Enhancement of 980 nm emission in co-doped Yb^{3+}/RE (RE=Pr^{3+},Tb^{3+}) fluoroindate glasses as potential material to improve silicon solar cell performance"**. In: 18th International Symposium of Non Oxide and New Optical Glasses ISNOG, 2012, Saint-Malo, France.

Galleani, G. ; Manzani, D. ; Ribeiro, S. J. L. ; Nunes, L. A. O. ; Pecoraro, E. **"Co-doped Yb^{3+}/Pr^{3+} fluorindate glass for enhanced silicon solar cell performance by down-conversion of high-energy photons"**. In: IX Brasilian Symposium on Glass and Related Materials , 2012, Curitiba, Brazil.

Galleani, G.; S. H. Santagneli ; RIBEIRO, S. J. L. ; Y. Messaddeq.**"Optical and Structural Properties of LiPO$_3$-WO$_3$-Na$_2$WO$_4$ Glasses"**. In:IX Brazilian MRS Meeting, 2010, Ouro Preto, Brazil.

Galleani, G.; Santagneli, S.H.; RIBEIRO, S. J. L.; Y. Messaddeq. **"Estudo Estrutural do Sistema Vítreo LiPO$_3$-WO$_3$ Através de Análise Térmica, Ressonância Magnética Nuclear e Espectroscopia Raman e de Infravermelho"**: XVII Encontro Regional da Sociedade Brasileira de Química, 2009, Araraquara, Brazil.

3.2. Publications in Journals:

G. Galleani, S.H. Santagneli, Y. Messaddeq, M. de Oliveira, H. Eckert, Rare-earth doped fluoride phosphate glasses: structural foundations of their luminescence properties, *Phys.*

Chem. Chem. Phys. (2017).

G. Galleani, S. H. Santagneli, S. J. L. Ribeiro, Y. Messaddeq, L. J. Q. Maia, L. A. O. Nunes, *Optical and structural properties of neodymium-doped KPO₃-MoO₃ glasses,* **Journal of Non-Crystalline Solids,** v. 458, p. 65 – 68, 2017.

G. Galleani, Y. Ledemi, E. S. de L. Filho, S. Morrency, G. Delaizir, S. Chenu, J. R. Duclere, Y. Messaddeq, *UV-transmitting step-index fluorophosphate glass fiber fabricated by the crucible technique,* **Optical Materials,** v. 64, p. 524 – 532, 2017

L. J. Borrero-González, G. Galleani, D. Manzani, L. A. O. Nunes, S. J. L. Ribeiro, *Visible to infrared energy conversion in Pr^{3+}-Yb^{3+} co-doped fluoroindate glasses,* **Optical Materials**, v. 35, p. 2085 – 2089, 2013.

3.2. Extendend abstracts published in conference proceedings:

S. J. L. Ribeiro, G. Galleani, L. Fortes, D. Manzani, R. A. S. Ferreira, L. D. Carlos, **Concentration dependence of the infrared photoluminescence of Pr^{3+} in fluoroindate glasses.** In: International Conference on Transparent Optical Networks (ICTON). Trento: IEEE, 2016, p. Th.B6.5.

4.   Prizes.

•   "Best Poster Award" for the contribution: Enhacement of 980 nm emission in co-doped fluoroindate glasses. In: 18th International Symposium on Non-Oxide and New Optical Glasses ISNOG in the period1-5 July, 2012, Saint-Malo, França.
•   "Honorable Mention" with the work: Ultraviolet upconversion Luminescence and Structural Properties in Triple-doped Gd^{3+}-Tm^{3+}-Yb^{3+} Fluoride-phosphate Glasses. In: T he 10th International Conference on nanophotonics, in the period 2 – 5 July, Recife, Brazil.
•

RÉSUMÉ

Le développement de nouvelles fibres optiques capables de transmettre dans les régions de l'ultraviolet moyen (200-300 nm) et lointain (120-200 nm) bénéficierait aux techniques de microlithographie, aux technologies laser, et également à la détection chimique (détection du phosphore et du soufre pour l'agriculture), ce qui représent la principale motivation de ce travail. En outre, les verres mixtes fluorure/phosphate peuvent offrir un environnement de fluorures de faible énergie de phonons qui est favorable pour l'émission avec une grande efficacité quantique lorsqu'ils sont dopés avec des ions de terre rare trivalents. Une telle propriété rend alors leur utilisation attractive pour d'autres applications également sous forme de fibres et/ou verres massifs dans le domaine de la photonique.

La seule fibre connue pouvant opérer dans l'UV (~170-300 nm) est constituée de silice pure dopée avec OH/F. Cependant, l'utilisation de telles fibres est limitée par l'effet de solarisation qui dégrade la transmission de la lumière UV après une exposition prolongée.

Les verres à base de *fluorophosphate* (FP) sont des matériaux hautement transparents dans l'UV lorsqu'ils possèdent de faibles quantités d'impuretés, offrant ainsi une alternative aux fibres de silice utilisées aujourd'hui dans cette région du spectre électromagnétique. Ces verres sont produits par le mélange de fluorures et polyphosphates et combinent ainsi leurs propriétés telles que: une excellente aptitude à vitrifier, un faible indice de réfraction et une large fenêtre de transmission (~ 160-4000 nm). Toutefois, peu d'études ont été rapportées à ce jour sur leur méthode de fabrication et par conséquent, les pertes optiques dans la région UV. En outre, lorsqu'il est dopé avec des ions de terres rares trivalentes (RE), l'environnement de faible énergie de phonon est favorable pour les efficacités quantiques élevées, ce qui permet une application photonique sous forme de fibre et/ou de verre massif.

Par conséquent, des verres FP très purs ont été préparés et utilisés pour fabriquer des fibres optiques à saut d'indice, par une technique de creuset modifiée. Dans une première étape, les verres ont été étudiés pour être très transparents dans la région VUV, jusqu'à 160 nm, et les caractéristiques des températures, la viscosité autour du point de ramollissement ont été caractérisées. Ensuite, les fibres ont été fabriquées par la technique du creuset, par l'étirage d'une préforme à travers un creuset en silice fondue. Alors que la cristallisation incontrôlée a été observée lors du tirage des fibres par le procédé classique, l'étirage à partir

d'un creuset en silice fondu s'est avéré approprié pour obtenir des fibres de verre FP exemptes de cristaux. Ensuite, des mesures d'atténuation ont été effectuées sur les fibres.

La deuxième partie de cette thèse est compose de deux parties: l'étude structurale des verres FP avec différent ratios fluorure/phosphate et la corrélation des propriétés luminescentes des verres dopés avec des ions de terres rares avec leur structure. Les verres obtenus ont été caractérisés par différentes techniques, calorimétrie différentielle à balayage (DSC), spectroscopie Raman et résonance magnétique nucléaire à l'état solide (RMN). Au cours de l'étape suivante, on a utilisé des techniques de double resonance ^{27}Al/^{31}P pour quantifier le nombre moyen de liaisons P-O-Al dans les verres et l'environnement local des espèces de fluorure a également été déterminé. Ensuite, les verres ont été dopées avec des ions de terres rares et l'environnement local a été caractérisé par spectroscopie de résonance paramagnétique électronique (RPE) de la sonde Yb^{3+} et par des expériences de photoluminescence sur des ions Eu^{3+}. Les propriétés de la luminescence ont été corrélées avec la transformation structurale en fonction de la composition.

Enfin, en raison de la haute transparence UV, nous avons préparé des verres FP dopées avec des ions Gd^{3+}, Tm^{3+} et Yb^{3+} comme candidat potentiel pour la fabrication de lasers à fibre UV. Les propriétés de photoluminescence sous excitation au laser à diode de 980 nm ont été étudiées et l'effet des différent ratios fluorure/phosphate dans les verres sur l'émission de conversion ascendante UV du Gd^{3+} a egalement été etudié. Ensuite, leurs propriétés structurales ont également été explorées par la résonance magnétique nucléaire du ^{45}Sc, incorporé pour imiter les ions de terres rares dans la matrice vitreuse.

En utilisant la technique de la double résonance ^{45}Sc/^{31}P, la distribution du ligand entourant les ions de terres rares a été quantifiée et l'efficacité de l'émission du Gd^{3+} par rapport aux ions Tm^{3+} avec la structure a été effectuée.

ABSTRACT

The development of new optical fibers capable to operate in the deep-ultraviolet (DUV, 200-300 nm) and the vacuum-ultraviolet (VUV, 120-200 nm) would benefit to laser technologies, microlithography techniques (increased spatial resolution) and elemental chemical sensing applications (phosphorous and sulfur sensing in agriculture).

The only well-established UV-transmitting fiber existing to date consists in high-OH/fluorine doped silica glass core/clad fibers. However, the utilization of such fibers is limited by solarisation effect that degrades the UV-light transmission with long time exposition.

Mixed fluoride-phosphate (FP) glasses with ultra-low content of impurities can be VUV- and/or DUV-transmitting materials, offering thus an alternative to the commercialized high-OH/fluorine doped silica fibers. These glasses are produced by mixing fluorides and polyphosphates to combine their properties as excellent glass-forming ability, low refractive index and broad optical transmission windows ranging from ~160 to 4000 nm. Also, when doped with trivalent rare-earth (RE) ions, the low phonon fluorine environment is favorable for RE high quantum efficiencies, making then suitable for photonic application in the form of fiber and/or bulk glass.

Firstly, highly pure FP glasses were prepared and utilized to fabricate step-index optical fibers, by a modified crucible technique. In a first step, the bulk glasses were studied to be highly transparent in the VUV region, down to 160 nm, and the characteristics temperatures, viscosity around softening point were characterized. Then, the fibers were fabricated by the crucible technique, drawing the as-made core-cladding preforms in a silica crucible assembly. While uncontrolled crystallization was observed during the fiber drawing by the conventional method, drawing from a fused silica crucible showed to be suitable to obtain crystal-free FP glass fibers. Additionally, the cut-back method was employed to measure the optical attenuation on the FP step-index and single index glass fibers.

The second part of this thesis involves the network structural investigation of a series of FP glasses with different fluoride/phosphate ratio. Raman and multinuclear solid-state nuclear magnetic resonance (NMR) spectroscopies were used to study the polyphosphate network transformation for the different fluoride/phosphate ratios. In the next step ^{27}Al/^{31}P

double resonance techniques were used to quantify the average number of P-O-Al linkages in the glasses and the local environment of fluoride species were also determined. Then, the glasses were doped with RE ions and the local environment was characterized by electron paramagnetic resonance (EPR) spectroscopy of Yb^{3+} ions probe and by photoluminescence experiments on Eu^{3+} dopant ions. The luminescence properties were correlated with the structural transformation as a function of composition.

Lastly, due to the high UV tansparency of the FP glasses, we prepared FP glasses doped with Gd^{3+}, Tm^{3+}, and Yb^3+ ions as a potential candidate for fabrication of UV fiber lasers. The photoluminescence properties under 980 nm diode laser excitation were studied, and the effect of fluoride/phosphate ratio in the glasses in the Gd^{3+} UV upconversion (UC) emission were verified. The effect of Gd^{3+} content in the UV UC emission was also studied. Then, by using $^{45}Sc/^{31}P$ double resonance technique, utilizing scandium as a diamagnetic mimic for the luminescent RE species, the ligand distribution surrounding the RE ions were quantified, and the efficiency of the Gd^{3+} emission, compared to the Tm^{3+} ions with structure was done.

RESUMO

O desenvolvimento de novas fibras ópticas capazes de operar na região do ultravioleta profundo (200-300 nm) e de vácuo (120-200 nm) beneficiariam aplicações em tecnologias a laser, técnicas de microlitografia (maior resolução espacial) e detecção química elementar (detecção de fósforo e enxofre na agricultura).

A única fibra de transmissão UV bem estabelecida existente até o momento consiste em fibras núcleo-casca de vidro de sílica dopado com OH/flúor. No entanto, a utilização de tais fibras é limitada pelo efeito de solarização que degrada a transmissão da luz UV apos exposição prolongada.

Os vidros mistos fluoreto-fosfato com baixas quantidades de impurezas, são materiais transmissores de luz UV-profundo e vácuo, oferecendo assim uma alternativa frente as fibras de silica utilizadas hoje. Estes vidros são produzidos pela mistura de fluoretos e polifosfatos com propriedades combinadas de ambos como, excelente capacidade de formação vítrea, baixo índice de refração e ampla janela de transmissão (~ 160 a 4000 nm). Além disso, quando dopados com íons terras-raras trivalentes, o ambiente de baixa energia de fonon dos fluoretos é favorável para emissões dos TRs com alta eficiência quântica, tornando-os então adequados para aplicações na área da fotônica na forma de fibra e/ou bulk.

Portanto, em primeiro lugar, foram preparados vidros FP altamente puros e utilizados para fabricação de fibras ópticas de índice-degrau, pela técnica do cadinho. Na primeira etapa, os vidros na forma de bulk foram estudados para serem altamente transparentes na região ultravioleta de vácuo, até 160 nm, e suas temperaturas características e a viscosidade em torno do ponto de amolecimento foram caracterizadas. Em seguida, as fibras foram fabricadas pela técnica do cadinho, preparando as preformas núcleo-casca em um conjunto de cadinho de sílica. Embora a cristalização não controlada tenha sido observada durante o puxamento das fibras pelo método convencional, o puxamento pelo método do cadinho mostrou-se adequado para obtenção de fibras de vidro FP sem cristalização. Além disso, a atenuação óptica nna fibra obtida foi medida na região UV.

A segunda parte desta tese envolveu a investigação estrutural de uma série de vidros FP com diferentes razoes fluoreto/fosfato. As espectroscopias RMN do estado solido e Raman foram utilizadas para estudar a transformação da rede de polifosfatos para as

diferentes razoes fluoreto/fosfato. Na etapa seguinte, utilizaram-se técnicas de dupla ressonância do $^{27}Al/^{31}P$ para quantificar o número médio de ligações P-O-Al nos vidros e o ambiente local das espécies fluoreto também foi determinado. Em seguida, os vidros foram dopados com íons TRs e o ambiente local foi caracterizado por espectroscopia EPR da sonda de íons Yb^{3+} e por medidas de fotoluminescência dos íons Eu^{3+}. As propriedades de luminescência foram correlacionadas com a transformação estrutural em função da composição.

Por último, devido à elevada transparência UV dos vidros FP, preparamos vidros FP dopados com íons Gd^{3+}, Tm^{3+} e Yb^{3+} como potencial candidato para fabricação de fibras laser UV. As propriedades de fotoluminescência sob excitação laser de diodo de 980 nm foram estudadas e o efeito da razão fluoreto/ fosfato nos vidros na emissão UV do íon Gd^{3+} por conversão ascendente de energia foi verificado. O efeito da concentração de Gd^{3+} nesta emissão também foi estudado. Em seguida, utilizando a técnica de ressonância dupla $^{45}Sc/^{31}P$, com o escândio como um mímico diamagnético para as espécies de terras-raras luminescentes, a distribuição dos ligantes no ambiente de coordenação dos íons TRs foi quantificada e a eficiência da emissão do Gd^{3+}, em comparação com as emissões do íon Tm^{3+} com a estrutura foi feita.

1. TABLE OF CONTENTS

LIST OF FIGURES

xvii

I dedicated this thesis to my family and friends, in whom I admire and love and have always supported me in this journey.

ACKNOWLEDGMENTS

I would like to thank those had a direct and indirect impact in my studies during these last 4 years.

I am glad of had been advised by Prof. Dr. Younes Messaddeq, who I admire for his expertise and enthusiasm. I am deeply grateful for all support, guidance, discussions and opportunities, which were essentials to my progress and learning.

Dr. Yannick Ledemi has also been an important person during all my PhD, as important as Prof. Dr. Younes Messaddeq himself. Thank you for all discussions, suggestions and teaching about science and also the valuable advices for life.

I have also many reasons to acknowledge my dear family Dr. Silvia H. Santagneli, but the one I am must thankful is for her guidance during my undergrad, master and PhD, for teaching me since the start, points of experimental science and for encourage my career and have provided me a lot of opportunities.

My gratitude to the whole Photonics Materials Group, especcialy: Professor Dr. Marcelo Nalin, Prof. Sidney Ribeiro, Prof. Edson Pecoraro and Dr. Danilo Manzani and Ferminio Cesar Polachini; and to my labmates, Karina, Moliria and Rafael. Specially Karina for her friendship here and during my stay in Quebec.

Prof. Hellmet Eckert and Dr. Marcos de Oliveira Jr. from Universidade Estadual de Sao Paulo, for had been my collaborators, providing investigation of strucutural properties of FP glasses by NMR and EPR techniques.

Concerning my stay in Quebec, I would like to thank Younes students, Maxime, Mathieu Desjardin, Mathieu Chazot, Mathieu Boivin, Guillaume, Tea, Rim, Mathilde and Mohammed, who helped during my stay, and facilitate my day to day life in the lab.

Thanks also to Steeve Morrency for the help and learning with the fiber drawing process, which we spent a lot of afternoons until succeed. It would not be possible without his help.

Also Prof. Dr. Denis Boudreau and his students from Univerté Laval – Quebec – Canada, who were always kind to me and helped in my stay in Quebec.

I would like to express my appreciation to my family and childhood friends, especially to my mom Selma, daddy Laercio and my sister Gabriela, even with all its simplicity they

provided me the chance to get here. Also, my appreciation to Aline, for her support and advices to work even harder every time i though about giving up, especially when i was far from.

Finally, my acknowledgments to São Paulo State University - Araraquara – through Institute of Chemistry – that has held all my studies since the beginning of my undergrad in 2007. I am finishing a 10-year process, which definitely changed my perspectives. And to Capes, for the financial support in all Ph. D. steps.

.

FOREWORD

The present thesis is based on three manuscritps of articles (2 published and 1 in process of submission) in peer-reviwed journals. I am the principal author in all of them.

Some details regarding the articles achieved during the years of the thesis as well as the role of the co-authors in the accomplishment of this work are given bellow.

My first article was realized in collaboration with Prof. Jean Rene Duclere, Prof. Sebastien Chenu and Prof. Gaelle Delaizir from "Laboratoire de Sciences des Procedes Ceramiques et de Traitements de Surface, Universite de Limoges", France.

Title: *UV-transmitting step-index fluorophosphate glass fiber fabricated by the crucible technique.*

Authors: G. Galleani, Y. Ledemi, E. S. de L. Filho, S. Morrency, G. Delaizir, S. Chenu, J. R. Duclere, Y. Messaddeq.

Journal: , **Optical Materials,** v. 64, p. 524 – 532, 2017.

State: Submitted in 24 october 2016. Published in 4 January 2017.

My second and article was realized in collaboration with Prof. Hellmut Eckert from "Instituto de Fisica de Sao Carlos", Brazil and "Institut fur Physikalische Chemie", WWU Munster, Germany.

Title: Rare-earth doped fluoride phosphate glasses: structural foundations of their luminescence properties

Authors: G. Galleani, S.H. Santagneli, Y. Messaddeq, M. de Oliveira, H. Eckert

Journal: *Phys. Chem. Chem. Phys*. (2017)

State: Submitted in 12 June 2017. Published. 25 July 2017.

My third article in process of evaluation was realized in collaboration with Prof. Hellmut Eckert from "Instituto de Fisica de Sao Carlos", Brazil and "Institut fur Physikalische Chemie", WWU Munster, Germany and Oliver Janka and Rainer Pöttgen from *Institut für*

Anorganische und Analytische Chemie, WWU Münster, Germany.

.

The roles of authors in these articles are the following: All the authors participated in the subject discussions. The subjects and experiment strategies were discussed with Prof. Y. Messaddeq, Prof. Hellmut Eckert, Dr. Yannick Ledemi and Dr. Silvia H. Santagneli. The preparation of glass samples and preforms was realized by me. Spectroscopic studies of glasses were principally performed by me. Structural studies of glass samples by NMR and EPR were realized by me, Prof. Hellmut Eckert, Dr. Silvia H. Santagneli and Dr. Marcos de Oliveira. Fabrication of fluoride-phosphate optical fibers were developed by me and Steeve Morency and the fiber losses measurements by me and Dr. Elton Soares. The refractive indices measured by ellipsometry were realized by Profs G. Delaizir, S. Chenu and J. R. Duclere. The experiment of luminescence measurements in doped fluoride-phosphate glass was discussed with Dr. Yannick Ledemi and realized by me. The elemental analyses were realized by Oliver Janka and Rainer Pöttgen. The writing of manuscripts was principally realized by me. After discussing the content and structure with Dr. Yannick Ledemi and Dr. S. H. Santagneli, I provided my version of manuscript to all co-authors who revised, edited and completed it.

THESIS SYNOPSES

In light of recent studies, fluoride-phosphate glasses are attractive alternatives to design highly ultraviolet transparent glasses and optical fibers for photonic applications. This is the reason why this material is the focus of the present thesis.

Therefore, the study is divided into 6 chapters, including an introduction, which gives an insertion to mixed fluoride-phosphate glasses and their fundamental properties and the motivation behind the development of optical fiber transparent in the deep-UV. The first chapter provides a necessary background regarding vitreous state and the basic theory for understanding fundamental optical properties of glass and fibers and the criteria for low losses fiber is introduced. The chapter 2 presents the millestones and objectives of this study.

Further, the Chapter 3 presents the development of ultra-high purity fluoride-phosphate (FP) glass fiber by a modified crucible technique. First, FP bulk glasses with different fluoride/phosphate ratio were prepared and characterized to determine the best ratio to fabricate FP fibers with high UV transmission. In this section, a focus is also given to the core-cladding glass preform fabrication and fiber drawing. The synthesis technologies used for the fabrication of FP glass fiber were discussed, as well as, the procedure of the fabrication of glass fibers. The need for high purity powdered precursors and their impact on optical quality for fabricated glasses is also discussed. Also we included all techniques used in the analysis of optical and thermal properties of these glasses and fibers. Chapter 4 focuses on the detailed structural investigation of a series of fluoride-phosphate glasses with different fluoride/phosphate ratio. It describes the glass network evolution by means of Raman and NMR techniques. Double resonance techniques, such as $^{31}Al\{^{27}Al\}$ REAPDOR and $^{27}Al\{^{31}P\}$ and $^{19}F\{^{31}P\}$ REDOR gives a more quantitative insight into the short and medium range order of the glass network. The local environment for RE ions in these glasses have also been characterized by EPR spectroscopy of Yb^{3+} ion spin probes and by photoluminescence experiments on Eu^{3+} dopant ions.

Finally, chapter 5, combining the high transparency and a more fluorine environment of FP glasses with high fluoride/phosphate ratio, FP glasses are proposed as host matrix for RE ions, more specifically, Gd^{3+}, Yb^{3+} and Tm^{3+}, which can have UV emissions under IR laser excitation as possible candidates for glass and fiber UV lasers applications. The effect

of Gd^{3+} content and fluoride/phosphate ratio on the UV upconversion emission were studied. Also we substituted these luminescent ions by the diamagnetic Sc^{3+}, to study the local environment by means of NMR techniques and a correlation between the glass network and the upconversion luminescence was investigated. Finally, chapter 6 summarizes the general conclusion of this PhD thesis.

1. INTRODUCTION

Glass is one of the oldest materials known from at least 7000 B.C. Its transparency ranging from the ultraviolet (UV) to the near-infrared (NIR) enables multiple applications in different fields like glazing, optics (e.g. lenses, objectives, etc.), telecommunication (e.g. optical fibers), astronomy (e.g. large mirrors for telescopes) (PHILLIPS, 1960). Among the numerous applications that rely on the emission, transport, conversion or detection of light (in the optical range of the electromagnetic spectrum), some of them involve a specific operation in the deep-ultraviolet (DUV, 200-300 nm) and vacuum-ultraviolet (VUV, 120-200 nm) regions. For instance, one can cite laser technologies for DUV microlithography equipment, microlithographic lens and photomask (EHRT; SEEBER, 1991; RAO, 2013), where fluoride crystals and vitreous silica are well-known materials traditionally used. There are also industrial and biomedical sensing applications, determination by atomic absorption spectroscopy (AAS) of chemical species that have atomic absorption in the deep-UV region as phosphorus and sulfur (DE CAMPOS et al., 2011).

Historically, UV grade silica glass has been used in the DUV and VUV down to 150 nm and for light transmission step-index silica fibers with high OH in the core and fluorine doped clad have been used down to 160 nm (SKUJA et al., 2003). However, they suffer from solarization effect caused by defects concentration increasing which leads to optical absorption in the deep-UV. As long-term stability of light transmission is highly desirable in optical systems designing, especially in high performance spectroscopy applications, the development of a new kind of DUV fibers is of major importance.

Fluoride glasses based on aluminum fluoride and other metal fluorides with wide band gap (LiF, MgF$_2$, AlF$_3$, CaF$_2$, BaF$_2$, NaF) have extended transmission in the UV with a cut-off wavelength around 160 nm, near to that of silica glass. However, their tendency to crystallize during glass manufacturing or fiber drawing strongly limits their fabrication in the form of optical fiber. Among the glass compositions and systems explored to date proposed an alternative to existing UV-transmitting optical materials, glasses based on mixed fluoride-phosphate systems appear as excellent candidates. In fluoride-phosphate glasses, the phosphate component generally improves the glass-forming ability and its glass stability

against crystallization, while the fluoride components provide some specific optical features (low-phonon energy, low refractive index, extended UV optical transmission).

A few works in the development of optical fibers based on fluoride-phosphate glasses transmitting deep-UV light have been reported in the literature, to the best of our knowledge. To date, only silica glass fiber, so-called UV-grade silica, is used for DUV optical transmission. So, in this thesis, we aim at developing and characterizing novel fluoride-phosphate glass optical fibers transmitting in the UV region.

1.1. MATERIALS WITH (LARGE AND) EXTENDED TRANSPARENCY IN THE UV

Optical materials with extended transparency in the DUV and VUV regions are of great importance for applications in high performance optics and laser technologies for medical application in angioplasty and perforation of heart muscle during bypass surgery (KHALILOV et al., 2015), microlithography equipment where deep-UV light is used to produce integrated feature sizes on a semiconductor computer chip where the resolution of the final circuits is inversely proportional to the wavelength of the laser used to photo-write the masks and special UV optics (VYDRA; SCHOETZ, 1999). Typical excimer lasers operation wavelengths are 351 nm (XeF), 308 nm (XeCl), 248 nm (KrF) and 193 nm (ArF) (RAO, 2013).

Another application is the determination of chemical species with absorption in the deep-UV region as phosphorus and sulfur that can be determined by direct AAS measurements since the primary resonance lines (most sensitive) are in the VUV at 177.5, 178.3 and 180.7 nm, respectively (DE CAMPOS et al., 2011) but is not typically determined because the VUV region is not adequate for commercial instruments since intense and stable light sources are not available (WELZ; SPERLING, 2008).

1.1.1. FLUORIDE CRYSTALS AND VITREOUS SILICA AS MATERIALS FOR UV OPTICS

Fluoride crystals, as CaF_2, LiF, MgF_2, BaF_2, BeF_2 and vitreous silica are well-known materials traditionally used for UV optics (LUCAS; SMEKTALA; ADAM, 2002). However, the production of fluoride single crystals is expensive, and not adapted for large scale manufacturing. On the other hand, glassy materials are easy to fabricate and to be obtained as optical fibers that can guide UV light and can be used for laser technologies and would facilitate the development of systems for remote sensing of chemical elements by AAS. Vitreous silica is produced in a form of multimode fibers with undoped core having high OH-content and fluorine doped cladding and is used in the UV region (OTO, 2007). Fluoride glasses are also characterised by a large transparency from the UV down to 160 nm to the infrared up to 7 μm (KITAMURA; HAYAKAWA; YAMASHITA, 1990). BeF_2 based glasses could be the best UV-transmitting glass down to 150 nm, but unfortunately, they are very toxic (WILLIAMS et al., 1981).

1.1.2. MIXED FLUORIDE-PHOSPHATE GLASSES

As an alternative to vitreous silica, fluoroaluminate glasses also presents higher transmission in the UV region. However, the lower viscosity value at the drawing temperature induces higher tendency to crystallisation. Since these advantages result primarily from the strong ionic character of fluoride glasses, considerable progress can be made by developing mixed fluoride-phosphate glasses (MÖNCKE et al., 2005).

Mixed fluoride-phosphate (FP) glasses are a compromise between the excellent phosphate properties such as high mechanical strength and glass-forming ability with fluoride properties as low refractive index, low partial dispersion, good laser properties and broad optical transmission windows ranging from ~160 nm to 4000 nm avoiding the corresponding drawbacks of each class of glass which lead in difficulties in fiber drawing.

Beyond the high transparency in the UV region and the possibility to achieve glasses with higher thermal-stability, an important parameter for drawing fibers, others important properties for photonics can be obtained by mixing fluoride and phosphate. Phosphate glasses

usually allow higher concentrations of rare earths dopants. But these glasses, present high phonon energy and OH^- species at a level that can introduce high losses to the RE's quantum efficiencies via non-radiative decay processes, contrary to fluoride glasses, with relatively low maximum phonon energy ($\sim$500 cm^{-1}), opening the possibility to design new-generation of UV lasers, optical amplifiers, radiation dosimetry (DE OLIVEIRA et al., 2015; KALNINS et al., 2013; WANG et al., 2015) and other photonic devices based in fibers.

Preliminary studies on fluoride-phosphate systems based in polyphosphates and fluorides have shown good combination of many desirable properties of the fluorides and phosphate components of the glass such as high transparency from UV to IR and low refractive index and are summarized in the Table 1.1 (EHRT, 2015).

Table 1.1. Properties of mixed fluoride-phosphate glasses; composition, glass transition temperature (Tg), refractive index (n) and UV edge (λ_0). Adapted from (EHRT, 2015).

Glass composition	$Tg(^0C)$	n	UV edge λ_0(nm)
$39AlF_3$-$23SrF_2$-$28CaF_2$-$10MgF_2$	400	1.405	150
$2Sr(PO_3)_2$-$98(AlF_3, Mg/Sr/CaF_2)$	410	1.420	153
$4Sr(PO_3)_2$-$96(AlF_3, Mg/Sr/CaF_2)$	440	1.435	155
$10Sr(PO_3)_2$-$90(AlF_3, Mg/Sr/CaF_2)$	445	1.460	160
$20Sr(PO_3)_2$-$80(AlF_3, Mg/Sr/CaF_2)$	490	1.504	165
$40Sr(PO_3)_2$-$60(AlF_3, Mg/Sr/CaF_2)$	500	1.506	178
$80Sr(PO_3)_2$-$20(AlF_3, Mg/Sr/CaF_2)$	540	1.580	-
$100Sr(PO_3)_2$	485	1.560	-
$10P_2O_5$-Al/YF_3, $Mg/Sr/Ba/CaF_2$,NaF	421	1.481	-

From the structural point of view, the short-range order of phosphate is usually described in terms of the $Q^{(n)}$ terminology, where n is the number of P next-nearest neighbors per P tetrahedron as shown schematically in Figure 1-1.
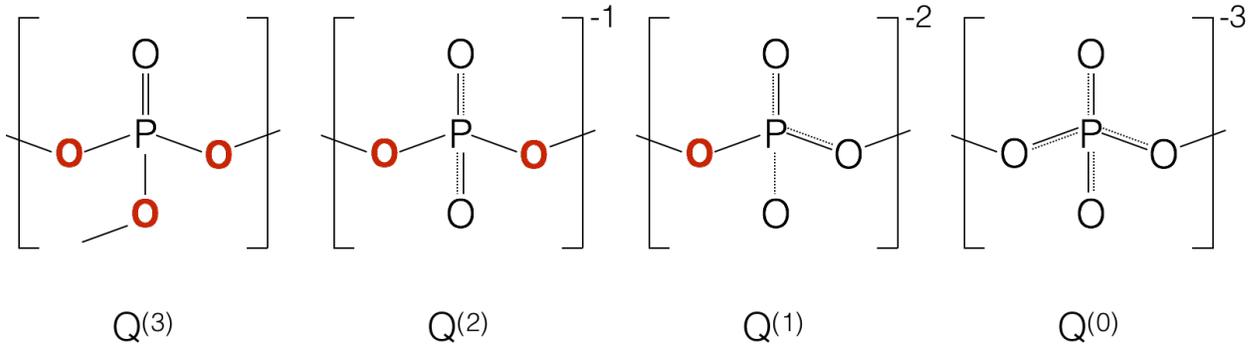
Figure 1-1. Schematic representation of Q^n phosphate tetrahedral units.

In fluoroaluminate glasses, AlF_6-octahedra connected by shared corners are proposed as the main glass forming entity (MÖNCKE et al., 2005). In the FP glasses, the structure consists of interconnected $Al(O/F)_6$-octahedra and PO_4-tetrahedra cross-linked by modifier cations, which the formation of P-O-Al linkages increases the rigidity of the structure, increasing the forming glass ability and slowing the nucleation process (DE OLIVEIRA et al., 2015). And when the efforts come to the development of highly UV transparent and RE-doped compositions, with excellent physical properties, the goal is to design a framework structure dominated by bridging oxygen links between the network formers, with the lowest amount of phosphate, resulting in high mechanical and thermal stability for fiber drawing, high UV optical transmission, while at the same time, creating a fluorine dominated low-phonon energy environment for the luminescent ions, which favours high fluorescence quantum efficiencies and long excited-state lifetime values.

In practice, manufacturing glasses with high UV transmission is difficult from a practical point of view. First, the UV absorption is dominated by electronic transitions from the valence to the conduction band. The bonds present in the structure dominate the energy gap between the valence and conduction bands, and thus the energy of the transition. The short-range structure dominates the electronic transitions (BERSUKER, 2010). In crystalline CaF_2 for example, the transition occurs at ~10 eV (124 nm) and for the SiO_2 glass, occurs at ~8.25 eV (150 nm), which is similar to that of fluoroaluminate glasses based on AlF_3 and MF_2 (M = alkaline earth metal). Their energies are comparable with those of fluoride single crystals, and the addition of phosphates decreases the band gap energy (Table 1.1).

Besides this fundamental intrinsic absorption, extrinsic absorptions caused by trace impurities restrict the practically achievable transmission. Transition metal (TM) ions as Fe^{3+}, Cr^{3+}, Cu^{2+}, are the main trace impurities present in the glass and their charge transfer bands have high absorption coefficients (EHRT, 2015). Even small amounts of TM ions (ppm range) may cause dramatic deterioration of the UV transmission and may also increase the material sensitivity to radiation damage. Charge transfer transitions $\varepsilon \geq 10^3$ $M^{-1}cm^{-1}$ are preferred over electron transitions bands with $\varepsilon = 10^{-2}$ to 10^2 $M^{-1}cm^{-1}$.

Iron is a particularly undesirable impurity which is easily introduced into the glass from the starting raw materials in small quantities (ppm) and the possible contamination from the melting technique and method of processing used (COOK; MADER, 1982). Two broad bands are observed in glasses due to Fe absorption at around 200 nm and 250 nm. The band at 250 nm is attributed to Fe^{3+} and the band at 200 nm to Fe^{2+}.

The effect of metallic impurities (Ce, Pt, Fe, Ni, Cr, Cu, Pb, Sn, Ti) in the ppm range on the UV absorption edge of fluoride-phosphate glasses were intensively investigated (EHRT, 1996; EHRT; LEISTER; MATTHAI, 2001; MATTHAI; EHRT; RÜSSEL, 1998), and Seeber at al. (EHRT, 2015) found that the UV absorption of the glass depends also on melting conditions, with variations in the observed UV absorbance intensity, when different atmospheres and container materials were used.

Glasses melted under reducing conditions (i.e. with added reducing agents or in carbon crucible) can exhibit much greater UV transmission near 250 nm than glasses melted under oxidizing conditions due to reduction from Fe^{3+} to Fe^{2+}. For small content of iron, 6 ppm, the effect is smaller (EHRT, 2015).

1.1.3. DEEP-UV FIBER AND RADIATION INDUCED DEFECTS

Another important property of optical materials is their resistance to radiation damage. Ionizing radiation produces free holes and electrons in glass which are then trapped, forming defect centers. These defects centers cause a decrease in optical transmittance in the UV and visible range of the spectrum and are commonly referred to solarization.

The silica fiber with high OH content core possesses high initial transmission, which is due to the smaller concentration of intrinsic defects, but when irradiated by UV light,

solarisation process are important and decreases considerably the UV transmission (OTO, 2007).

In FP glasses, the solarisation effect depends on iron content, melting conditions, radiation doses and heat treatment. The formation of color centers by excimer laser radiation is likely to be the result of photoionizable multivalent ions present as trace impurities, mainly iron, into the glass (JIANG et al., 2015).

Ehrt et al (EHRT et al., 1994) observed that fluoride-phosphate glasses with high iron content (27 ppm) melted in reducing conditions have a better UV-transmittance near 250 nm before irradiation since most of the iron exists in the Fe^{2+} state, but stronger solarisation effect was induced by excimer laser radiation than the same glass melted in oxidizing conditions. For low iron content (6 ppm), a weak susceptibility to solarisation was observed at low radiation density.

Unlike silica glass, FP glasses with low phosphate content possess less oxygen defects. Controlling the impurities in the glass can have greater resistance to radiation. Therefore, FP glass fibers with low content of impurities can be UV-transmitting optical materials that are complementary to silica glass fiber and fluoride crystals.

To achieve ultra-low losses in FP glass fibers, similar to those obtained sin silica fiber, which technology is pretty mature nowadays, it is not an easy task and few works in the literature report on fabrication on FP glass fibers. Step-index FP fiber were fabricated by Zou et al. drawing a preform in the system P_2O_5-AlF_3-YF_3-MgF_2-RF_2-NaF, (R = Mg, Ca, Sr and Ba) obtained by extrusion. The minimum loss they measured in the UV was 0.11 dB/m at 365 nm, while extrinsic absorption bands were observed due to the presence of transition metal impurities at 340 nm (Fe^{3+}), 520 nm (Cr^{3+}, Ni^{2+}) and 800 nm (Cu^{2+}, Fe^{2+}) (ZOU; ITOH; TORATANI, 1997; ZOU; TORATANI, 1997). Using a commercial fluoride-phosphate glass (N-FK51A), Kalnins et al. have prepared an unclad optical fiber by drawing preforms also produced by extrusion. Preform neck-down crystallization issues during fiber drawing were observed and they reported a minimum losses of 3.05 dB/m at 405 nm only after increasing the preform feed-rate and drawing speed, which decreased the time of exposure of the preform in the furnace and consequently, the surface crystallization issues (KALNINS et al., 2011). They also showed that treatment of extruded preforms prior to fiber drawing further improved optical fiber loss to 0.5-1 dB/m. Thus, in this thesis, there is an interest in the opportunities

offered by the high transparency in UV regions of mixed FP glasses for fabrication of optical fiber for technological applications.

1.2. STATE OF ART: GENERAL CONSIDERATION ON GLASSES
1.2.1. GLASS DEFINITION

In popular usage, "glass" denotes a transparent and fragile material and is often used to refer only to that based on the chemical compound silica (silicon dioxide), which is familiar from use as window glass and in glass bottles.

In scientific language, glass is a non-crystalline solid, isotropic material obtained by rapid cooling of a liquid. However, the fast cooling of liquid is not the only method for obtaining non-crystalline solids. Basically, non-crystalline solids can be obtained by fast cooling maintaining the structural disorder of the liquid phase, by mechanical compression, interrupting the order of a crystal and by evaporation, using the disorder nature of the gas phase (ZARZYCKI, 1982).

From a structural point of view, a non-crystalline solid is characterized by the absence of long-range order which defines crystalline materials and as in the amorphous solids, the atomic structure of glass lacks any long-range translational periodicity (GUPTA, 1996).

In a good glass former, the network structure is topologically disordered, because these structures possess intrinsic resistance towards crystallization, which requires topological changes (bond breakage and reformation) and the short-range order is the same as in the corresponding crystal. For example, the SiO_4 tetrahedra that form the fundamental structural units in silica glass represent a high degree of order, i.e. every silicon atom is coordinated by 4 oxygen atoms and the nearest neighbour Si-O bond length exhibits only a narrow distribution throughout the structure (GUPTA, 1996).

Not all non-crystalline solids are glasses. They can be classified as amorphous solids or glasses. The non-crystalline solid is a glass, if its short-range order is the same as that in its molten state. This condition is clearly satisfied for glasses formed by cooling a molten liquid because the structure of a melt is frozen during the transition from liquid to glass. Whether a non-crystalline solid is made by melt-cooling or by other methods (for example, evaporation) it is called glass as long as it satisfies this condition. If these conditions are

respected, but short-range order of the glass is different from the molten liquid the material will be classified as an amorphous solid. In addition, amorphous solids and glasses are distinct thermodynamically. The free energy of amorphous solids is less than that of super-cooled liquid and they do not show structural relaxation. The heating of these substances leads to rapid crystallization or decomposition of structure before their melting point is reached. Contrariwise, the glass passes progressively from a solid state to a liquid state with the successive increase of temperature. Such transition (from solid to molten state or the reverse one) is called "glass transition". So, one of the most used and cited in the literature definition of glass have been proposed by Zarzycki (ZARZYCKI, 1982): "Glass is a non-crystalline solid exhibiting the phenomenon of glass transition temperature."

1.2.2. GLASS TRANSITION TEMPERATURE (TG)

The conventional method for producing a glass is the very rapid cooling of the liquid, in order to prevent crystallization. Decreasing the temperature, an increase in viscosity of the liquid rapidly occurs, leading to the freezing of the liquid to the final solidification. Temperature decreases leads to a volume variation (contraction of the substance) and when the solidification point is reached, two distinct phenomena can occurs (Figure 1-2).
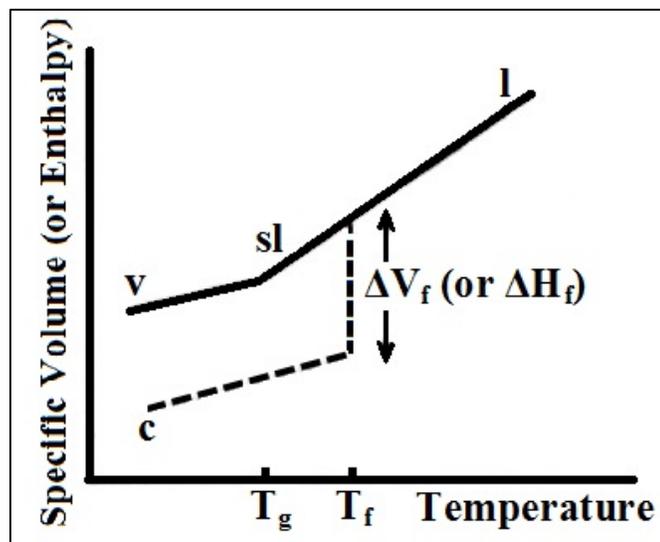
Figure 1-2. Variation of the specific volume with temperature. Adapted from (ZARZYCKI, 1982). (l – liquid; sl – super-cooled liquid; c – crystal; v - glass

9

(i)   The liquid crystallizes and a discontinuity of ΔV_f is introduced. This discontinuity is characteristic of a first order transition.

(ii)   Crystallization is prevented and the liquid passes to the super-cooled state starting from certain temperature and there is no discontinuity in the specific volume versus temperature curve shown below in proximity of the transition. The jump in the curve shows the transition from the supercooled state to the glassy state. The glass transition temperature, Tg, is defined as the point where a change in slope takes place. This is associated with a change in the thermal expansion coefficient from the glass to the liquid state. This type of transition which does not involve any discontinuity in the V-T curve (and similarly in the enthalpy versus T curve) is often called a second order transition.

1.2.3. GLASS OPTICAL PROPERTIES

Light transmission, absorption, reflection, and scattering describe the macroscopic aspects of light-glass interaction. These optical properties can be simply characterized by the spectral transmittance as a function of wavelength of the irradiating light, and depend on the elements of which it is composed, including the nature of its anions and cations.

Spectral transmittance is the ratio of the incident light leaving the glass to the light of monochromatic light radiation.

The incident light can be divided over the total interactions:

$$I = I_r + I_{abs} + I_t + I_{sc} \tag{1}$$

where I_t is the transmitted light, I_{abs} the absorbed light, I_r the reflected light and I_{sc} the scattered light. Therefore, light is part absorbed, reflected and transmitted.

Absorption in glass is characterized by a decrease in transmitted light intensity through the sample that is not accounted for by reflection losses at the surface or scattering by inclusions. The quantity used to discuss absorption as a function of wavelength in glass is the transmittance (T), which is the ratio of the transmitted light intensity (I) to the initial light intensity (I_0) after passing through a glass plate of thickness l:

$$T = \frac{I}{I_0} \tag{2}$$

The transmittance can be expressed to the more common percent transmittance (%T) through:

$$\%T = 100T \tag{3}$$

Sometimes it is more practical to look at the optical spectra in terms of absorbance rather than the transmittance. Absorbance (A) is defined as the $\log_{10}$ of (1/T):

$$A = log_{10} \frac{I_0}{I} = log_{10} \frac{1}{T} = 2 - log_{10}\%T, \tag{4}$$

$$\%T = \frac{100}{10^A} \tag{5}$$

When the absorbance changes linearly with concentration of the absorbing species (C), then Beer's law, which relates absorbance with concentration, path length (l) and extinction coefficient (ε), is applicable

$$A = \varepsilon C l \tag{6}$$

The typical units of ε are liters mole^{-1} cm^{-1} and are often omitted. From Beer's law we see that the absorbance changes with path length which light is passing through. Because of this, the spectra (in A or %T) must list the sample thickness. Therefore, absorbance can also be normalized to path length in terms of an absorption coefficient (α) (cm^{-1}).

1.2.4. REFLECTION

The total transmission of a glass is determined by reflection at the glass surfaces and optical absorption in the glass. Neglecting multiple reflections between the glass surfaces, the total transmission in air of a flat sample at a specific wavelength is approximately equal to $(1-R)^2 e^{-\alpha l}$ where α is the absorption coefficient, l the thickness of the glass, and R the air–glass reflection coefficient. Reflectance depends strongly on the quality of the glass surface, the angle of incidence, the indices of refraction of the glass and the surrounding medium, and the wavelength. Reflectance can be specular, as in polished or precision-molded surfaces, or diffuse for ground or irregularly etched ones. The fraction of light of normal incidence reflected by a single plane surface is given by: $R = [(n-1)/(n+1)]^2$, in which n is the refractive index of the glass at the wavelength of interest (the refractive index of air is assumed to be 1).

11

1.2.5. REFRACTIVE INDEX

The refractive index, denoted by *n*, is a dimensionless quantity characteristic of a medium. It depends on the measurement wavelength but also on the characteristics of the environment in which light propagates. In order to understand the propagation of light in a glass and thus the refractive index, we are interested in a simple system with two homogeneous isotropic media of respective refractive indices n_1 and n_2, as shown in Figure 1-3, Where we assume that $n_1 > n_2$. We consider an incident light beam making an angle θ_1 with the normal to the tangential plane to the boundary surface between the two media. This ray is reflected and refracted if the angle of incidence is different to zero.
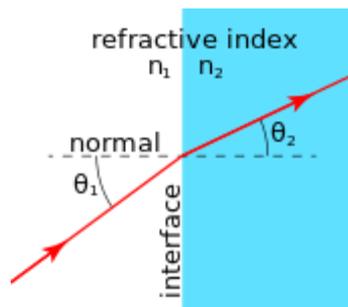
Figure 1-3. Refraction of light phenomenon in the passage through two homogeneous isotropic media of respective refractive indices n_1 and n_2. Adapted from (Bach et al., 1998)

The Snell-Descartes law specifies that: the reflected and refracted ray are in the plane defined by the radius incident and normal to the surface; the angle of reflection is equal to the angle of incidence; The relationship between the angle of refraction and the angle of incidence is $n_1 \sin\theta_1 = n_2 \sin\theta_2$

Refraction is the scientific term that applies to the deflection of light due to the variation of the refractive index. There is refraction as long as $\sin\theta_1 < \sin\theta_2 = n_2/n_1$, as long as $\theta_1 < \theta_2 = \arcsin(n_2/n_1)$, where θ is the critical angle.

When $\theta_1 > \theta_2$: there is total reflection.

1.2.6. TRANSMISSION WINDOW

Glasses can be transparent from the UV to the IR regions depending on the composition. The region of transparency is known as transmission window and is limited intrinsically by three physical phenomena: electronic absorption at short wavelengths (UV-Vis range), multiphonon absorption at long wavelengths (IR range), and scattering in between. Extrinsic losses are often observed within this window and arise from impurities in the glass. Glasses possess a characteristic energy gap, Eg. Incident photons with energy exceeding this gap, hv>Eg, will excite an electron from the valence to the conduction band creating an electron-hole pair. Thus occurs in multiple non-radiative steps generating phonons rather than photons. The electronic band gap depends on the electronic configuration and positional arrangement of the atoms in the material. In crystalline materials, the lattice positioning dictates a long-range atomic order suggesting a sharply defined band gap and steep rise in absorption at short wavelengths. However, disorder due to crystal defects, and more importantly temperature, ensures the band gap is not sharply defined and shifts the electronic edge absorption to longer wavelengths and imparts a more gradual dependence of absorption on wavelengths, resulting in the called Urbach tail (BACH; NEUROTH, 1998). In the amorphous form of the same material, the crystalline short-range atomic order is typically retained, but the long-range positioning does not keep to any crystal lattice. The electronic absorption edge therefore is usually situated in approximately the same energy (wavelength range) as for the crystalline form, but is less sharply defined and takes on a more gradual wavelength dependence.

The IR cutoff is determined by the multiphonon absorption edge and is governed by vibrational resonances of the atomic network which depend on atomic mass and bond strength. For glasses with larger atoms and weaker bonds, this vibrational resonance occurs at lower frequencies, pushing the fundamental absorption infrared cutoff to longer wavelengths (BRINKMANN et al., 2007).

The wavelength of absorption of a bond is expressed by:

$$\lambda = 2\pi c \sqrt{\frac{\mu}{\kappa}} \qquad (7)$$

where, c is the speed of light in vacuum, μ the reduced mass and κ the molecular force constant. The most common extrinsic absorption centers in the IR are OH, CO_2 and iron. The multiphonon edge is shifted to longer wavelengths (smaller frequencies) by heavier ions (greater M) and weaker bonds (smaller f), which is why chalcogenide glasses transmit further into the IR than more traditional oxide glasses.

Figure 1-4 shows the transmission window for 3 different type of glasses, oxide, fluoride and chalcogenide.
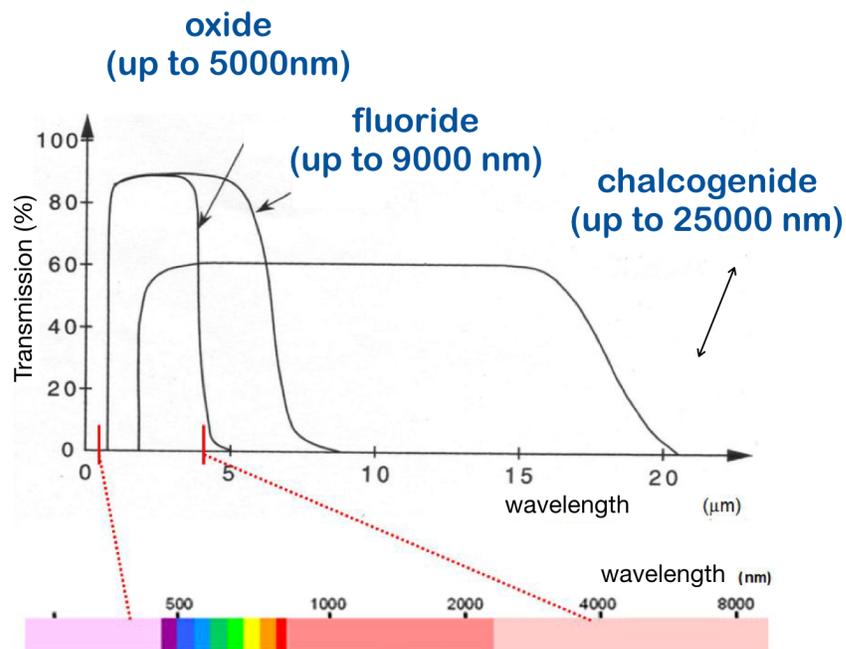
Figure 1-4. Example of transmission window for different classes of glass adapted from (NALIN et al., 2016).

1.3.   FUNDAMENTAL ASPECTS OF OPTICAL FIBERS

1.3.1.   PROPAGATION IN A CONVENTIONAL STEP-INDEX FIBER

Conventional optical fibers are cylindrical waveguides made of glass and composed of an inner part, the core, with refractive index n_{core}, surrounded by a glass cladding with slightly lower refractive index $n_{cladding}$, $n_{cladding} < n_{core}$. This structure is eventually covered

14

with a polymeric coating for mechanical protection and protection against degradation of the material by the environment, as schematized in Figure 1-5.
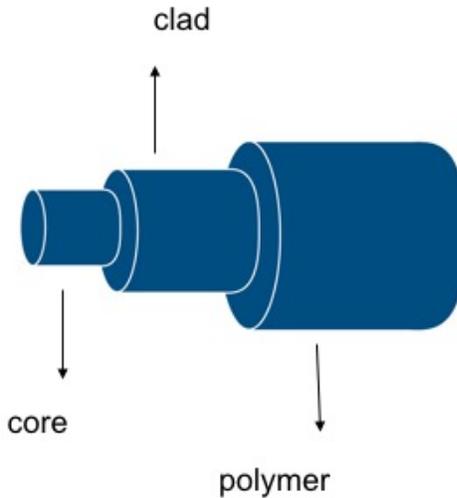
Figure 1-5. Schematic figure of a conventional optical fiber.

The light is totally reflected at the interface by total internal reflection if the angle of incidence is greater than a critical angle (θ_c). This property allows guiding light into the core of step-index optical fibers.

The total internal reflection condition at the interface between the core and the clad is limited by a maximum angle of incidence at the interface of the core to the external medium:

$$\theta_{max} = arcsin\sqrt{n_{core}{}^2 - n_{cladding}{}^2} \tag{8}$$

where n_{core}, $n_{cladding}$ are the core and cladding refractive index, respectively.

This angle determines the cone of acceptance of the fiber, and the sine of this angle is called the numerical aperture (NA), which is used to characterize the amount of light that the fiber can guide through the core:

$$\text{NA} = \frac{\sqrt{n_{core}{}^2 - n_{clad}{}^2}}{n_0} \tag{9}$$

The higher the NA, higher the angle of acceptance. Thus, the larger the NA of the fiber, the greater will be the ability to guide light into the core, which is defined by the ratio:

$$\Delta = \frac{\sqrt{n_{core}^2 - n_{clad}^2}}{n_0} = \frac{NA^2}{2n_{core}^2} \qquad (10)$$

In most optical fibers, the core and cladding refractive index are not too different. When $\Delta < 0.01$, the fiber is considered single-mode.

1.3.2. MODES OF PROPAGATION

Depending on the relative diameter of the fiber core to the total fiber, light can travel through one or more paths, such paths are called modes. Conventional fibers can be of three types: multi-mode - step-index fibers, multi-mode - graded-index fiber, and single-mode – step index fiber fibers. The step-index fibers exhibit a discontinuity of the refractive index at the core-cladding interface, while the graded-index fibers exhibit a continuous variation of the refractive index in the direction from the core to the shell. The single-mode fibers are generally of step index and have a small core diameter. Figure 1-6 shows the three types of fibers.
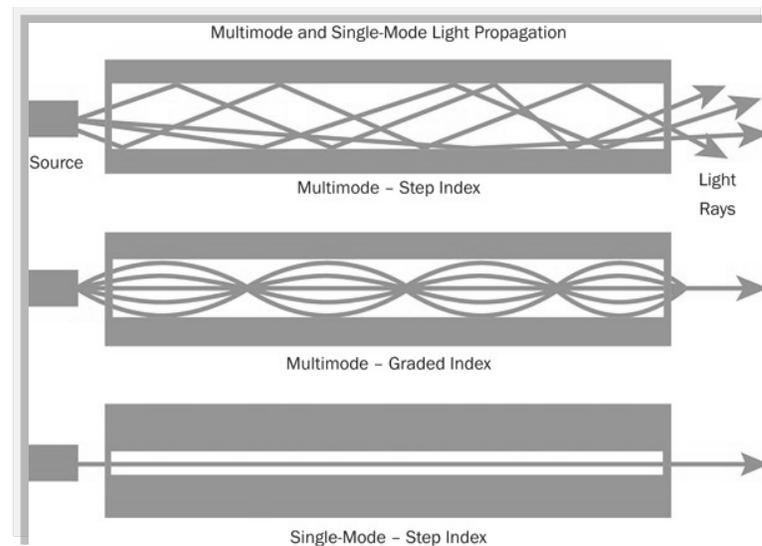
Figure 1-6. Schematic of light-ray propagation in multimode step-index, graded-index (b) and single-mode optical fiber. Adapeted from fiber optic share website (www.fiberopticshare.com)

1.3.3. OPTICAL LOSSES IN THE FIBER

Efficient light transmission at the operational wavelength(s) is the primary function of optical fibers needed for a range of applications (e.g. long-haul telecommunications, fiber lasers, optical delivery applications). Intensity loss, as light travels within the fiber is called "attenuation". To understand the attenuation mechanisms and the potential for their minimization is, thus, of great importance.

Any process that results in a reduction in the light intensity after propagation through a material contributes to the observed optical attenuation. In principle, all attenuation mechanisms can be followed back to the multilength scale structure of the glass itself, as atomic structure and point defects or structures arising from the fiber fabrication process, as interfacial structure at the core-cladding interface and uniformity of core-cladding structure along fiber length. Thus, the control of material structure through material processing, composition and fiber fabrication is the main way to reduce losses in the final optical fiber.

The global transmission of an optical fiber can be measured in terms of the input and output optical power, P_0 and P_L, respectively, observed after light propagates a distance l through the fiber length:

$$P_L = P_0 e^{-\alpha_{total} l} \tag{11}$$

where α_{total} is the total attenuation coefficient (involving all contributions). Transmitted power decreases exponentially with propagation distance (z) through the fiber, due to the losses.

The total attenuation coefficient above is often expressed in dB/Km unit:

$$\alpha_{total}(\tfrac{dB}{Km}) = \tfrac{10}{z} \log\left[\tfrac{P_0}{P_L}\right] = 4.343\alpha(Km^{-1}) \tag{12}$$

This final parameter is often referred to as the "optical fiber loss".

It is important to note that multiple contributions to a global transmission value arise from intrinsic fiber material properties as well as extrinsic attenuation mechanisms associated with fiber fabrication (preform development, drawing conditions). Therefore, the total attenuation can be divided into intrinsic and extrinsic source of losses. Each of these can be further subdivided into absorption loss and scattering loss.

1.3.3.1.   INTRINSIC OPTICAL ABSORPTION

The intrinsic optical absorption responses of core and clad glasses used were previously discussed as the primary factor dictating the transmission window in Item 1.2.6. (and ultimately the operational wavelengths) for an optical fiber. It is delimited on the long-wavelength side by absorption from multiphonon (vibrational absorptions of the chemical bonds and their harmonics) and on the short-wavelength side by the band-gap (absorptions of light through transitions of the valence band for the conduction band of the material).

Intrinsic light scattering arises from *Rayleigh scattering*, which is caused from micro-fluctuations in the refractive-index of the material, caused by changes in density and composition. The degree of scattering depends on the size of the scattering centers and the wavelength of the radiation, and the scattered intensity depends inversely on the fourth power of the wavelength: $I \propto \frac{1}{\lambda^4}$.

1.3.3.2.   EXTRINSIC OPTICAL ABSORPTION

In addition to this energy structure of the base glass that defines the transmission window, the presence of defects in the glass structure, fiber fabrication process and the presence of impurities can produce absorption in both frontiers of electromagnetic spectrum that limits the transmission window. When such absorption is localized at frequencies within the transmission window and/or at the operational wavelength of the fiber, such structural elements present a significant loss in the optical fiber systems.

Impurities, in their bonding with the primary material anion, can also give rise to impurity-driven vibrational modes which can absorb either at the fundamental or overtones frequencies. The most problematic impurities in the 1 to 10 μm range are light atoms and, in particular, hydrogen. Vibrational impurities are important not only as dissolved species but also as macroscopic heterogeneities and as surface impurities.

Similarly, impurities with metal-ion species, e.g. transitions metals, in the precursors reagents, inclusion during preform fabrication and/or drawing can also produce marked

attenuation in the UV-visible and near-IR spectral ranges. The most problematic impurities in the UV region, and very important for the scope of this thesis are TM, as mainly Fe, Cr, Co, even at small quantities in the ppm range. Such impurities come from the precursor reagents and also during the synthesis of the material.

Extrinsic light scattering arises from Mie scattering and imperfection such as bubbles, microcrystals and core-cladding boundary fluctuations. These defects arise during fiber fabrication and are responsible for the largest extrinsic losses that are sometimes observed.

1.3.4. PREDICTION OF LOSS MINIMA

The theoretical loss minimum α_{min} of an optical material as a function of λ can be determined by assessing the intrinsic attenuation process that defines the transmission window. These are usually assumed to be the multiphonon edge, the Rayleigh scattering and the electronic transition edge. The schematic of such an "intrinsic window", known as a V-plot, is shown in Figure 1-7.
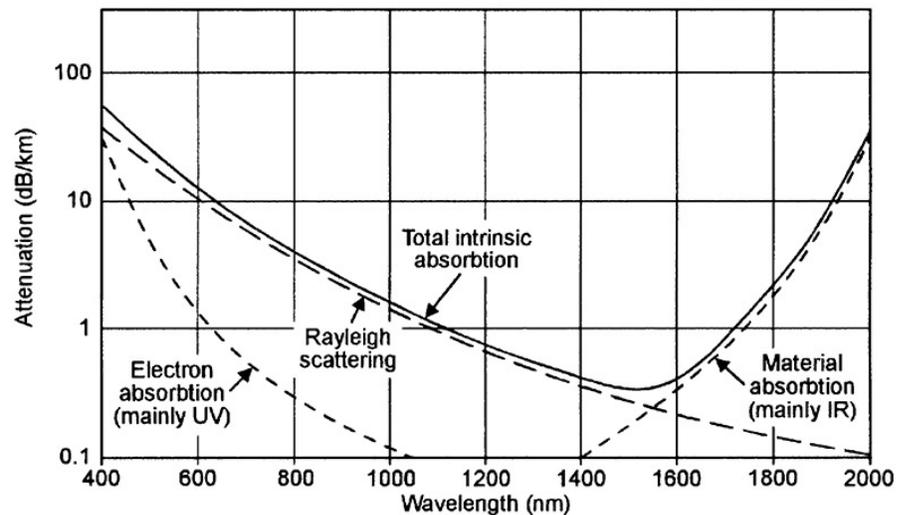
Figure 1-7. V-curve due to intrinsic optical absorption high grade silica fiber. Adapted from (MIMURA; NAKAI, 1991)

19

1.4.   FUNDAMENTAL ASPECTS OF SOLID-STATE NMR.

Nuclear Magnetic Resonance Spectroscopy (NMR) is based on the magnetic properties of atomic nucleus. This magnetism reflects their spin angular momentum, represented by the vector opearator I. Nuclear spins are subject to orientational quantization, according to $\mu_z = m\hbar$, with energetically degenerate characterized by the quantum number $m \in \{I, I-1, I-2, \ldots -I\}$, where I is the nuclear spin quantum number. Each nuclear magnetic moment (μ) is related to the nuclear spin I of the nucleus and given by

$$\vec{\mu} = \gamma\hbar\vec{I}$$

where γ is the magnetogyric ratio, and h is the Planck's constant.

In the presence of an external magnetic field B_0 the magnetic moment interacts with this field, with energy

$$E = -\vec{\mu}\vec{B_0}$$

1.4.1.   THE BASIC INTERACTIONS IN SOLID-STATE NMR.
1.4.1.1.   THE ZEEMAN EFFECT

The Zeeman effect reults from an external perturbationof the spin system. Application of an external magnetic field $\underline{B}^0$ annihilates the isotropy of space. The formerly degenerate energy levels split into (2I + 1) levels of energy.

$$E_m = -m\gamma\hbar B^0$$

where I represents the spin number os the nucleus, m = (I, I-1, …, -I) the magnetic quantum number, γ its gyromagnetic ratio, and h is Planck's constant. The difference ΔE of two neighboring levels due to the Zeeman effect is directly field dependent. It is given by

$$\Delta E = \gamma\hbar B^0$$

and determines the resonance frequency of a nucleus for a given field strength. Hence, it is one of the parameters that influence the sensitivity of a nucleus.

Owing to its magnitude, the nuclear Zeeman Interaction is in general treated as the main interaction in solid state NMR. Thus, other nuclear interactions are considered as pertubations of the Zeeman interaction.

1.4.1.2.   CHEMICAL SHIELDING – CHEMICAL SHIFT INTERACTION

Each nucleus is "chemical shielded" by a cloud of electrons. The external magnetic field $\underline{B^0}$ induces rings currents in the electron clouds at the differrents crystallographic sites. These circulating currents, in turn, generate and induce magnetic field $\underline{B^{ind}}$.

$$B^{ind} = -\sigma B^0$$

where σ is the magnetic shielding constant of the nucleus. $\underline{B^{ind}}$ is directly dependent on the external static field $\underline{B^0}$ and tend to oppose to the latter.

In solid state NMR, the chemical shielding is orientation dependent and can reveal information about the close surroundings of the nucleus. The chemical shielding is represented by a tensor (ellipsoid). The deviation of the tensor ellipsoid from spherical symmetry is an intuitive measure for the anisotropy of the chemical shielding. The isotropic chemical shielding is the average value of the three tensor components.

$$\sigma_{iso} = \frac{1}{3}(\sigma_{xx} + \sigma_{yy} + \sigma_{zz})$$

The chemical shielding anisotropy Δ_{cs} is defined as

$$\Delta_{cs} = \sigma_{zz} - \sigma_{iso}$$

The asymmetry of the chemical shielding is defined as

$$\eta = \frac{\sigma_{xx} - \sigma_{yy}}{\Delta_{cs}}$$

21

The effective field $\underline{B}^{eff}$ at the site of the nucleus is the sum of the external field $\underline{B}^0$ and the induced field $\underline{B}^{ind}$

$\underline{B}^{ind}$ is in the order of 10^{-4} of the static external field $\underline{B}^0$. However, $\underline{B}^{eff}$ is the characteristic for a given crystallographic site, resulting in a slightly shifted resonance frequency.

$$v^{eff} = v^0(1 - \sigma)$$

By introducing the definition of the chemical shift δ

$$\delta = \frac{v^{eff} - v^{ref}}{v^{ref}} * 10^6$$

The $\underline{B}^0$ dependence of the resonance shift is removed. Additionally, the originally small effect of the chemical shielding is multiplied by a factor 10^6. δ is defined in units of part per million (ppm), v^{ref} is the resonance frequency of the nucleus in a reference compound. Resonance that tend towards negative values of the δ (ppm) scale are termed shielded or shifted upfield. Resonances that tend towards positive chemical shift values (ppm) are termed deshielded shifted downfield.

1.4.1.3.   DIPOLAR COUPLING

Due to its dipolar magnetic moment, each nuclear spin I generates a magnetic field surrounding it. Neighboring nuclear spins interact with this nuclear field directly trhough space. Each spin I is the source of a magnetic field and, in turn, experiences those generated by neighboring spins S. in the case of homonuclear dipolar coupling the spins I and S are of the same species. In the case of heteronuclar dipolar coupling the spins I and S are different.

The dipolar interaction can be described by substituting the quantum mechanical magnetic moment operator into the classical expression for the interaction between two point magnetic dipoles

$$\hat{H} = -\frac{\mu_0}{4\pi}\gamma_I\gamma_S\hbar\left\{\frac{I \cdot S}{r^3} - 3\frac{(I \cdot r)(S \cdot r)}{r^5}\right\}$$

where I and S are the spin magnetic moments with their respective gyromagnetic ratios γ_I and γ_S, h is Planck´s contant and μ_0 is the permittivity of the vacuum. r is the internuclear distance between I and S.

The description of dipolar coupling illustrates best that the strength of the dipolar interaction between two nuclei depends in first approximation on the inverse of the cubic distance between them, that is $\widehat{H} \propto \frac{1}{r^3}$.

Dipolar coupling does not have any isotropic contribution. Its orientation dependence is of the form

$$(3cos^2\theta - 1)$$

and hence its averages to zero under magic angle spnning.

Since the sipolar interaction between two nuclei depends in first approximation on t he inverses of the cubic distance between them, it can be exploited to probe spatial proximities between nuclei. Therefore, the dipolar interaction can be *reintroduced* by sequences like REDOR or REAPDOR.

1.4.1.4.   SCALAR COUPLING (J-COUPLIN)

Nuclear spins interact with each olther via the bonding electrons they share. The terms scalar coupling or J-coupling are frequently used for this indirect coupling. The participation of the bonding electrons gives rises to an orientation dependence that is different from the one of dipolar coupling. As a result, there exists an isotropic component that contributes to scalar coupling and persists even under magic angle spiining conditions in solids or Brownian motion in liquids.

1.4.1.5.   ELETRIC QUADRUPOLAR COUPLING

All nuclei with a spin I>1/2 has a non-spherical charge distribution that gives rise to a nuclear electric quadrupole moment that interacts with the electric field gradient at the site of the nucleus.

Quadrupolar coupling is not completely removed by MAS. A second-order term persists, giving in many cases rise to characteristically broades resonances that can be characterized by the quadrupolar coupling constant *Cq* and the asymmetry parameter η_q.

In practice, *Cq* indicates the strength of the quadrupolar coupling between the nucleus and the electric field gradient of its proximate surroundings. It determines the linewidth of the NMR signal in the MAS dimension.

1.4.2. METHODS OF NMR SPECTROSCOPY
1.4.2.1.   MAGIC ANGLE SPINNING

Powder samples consist of many crystallites with random orientations, their high number giving rise to a large distribution of spectral frequencies. Broad powder patterns are obtained, if the spectrum is recorded under static conditions. As a result, different crystallographic sites can overlap, concealing information. As mentioned above, this loss of spectral resolution can be eliminated in great part by magic angles spinning (ANDREW; BRADBURY; EADES, 1959).

The basic principle of MAS is that most of the nuclear spin interactions present an orientation dependence of the following form:

$$(3cos^2\theta - 1)$$

where θ is the angle between the static field $\underline{B}^0$ and the principal z-axis of the tensor ellipsoid of the nuclear spin interaction (FIGURE 1-8)
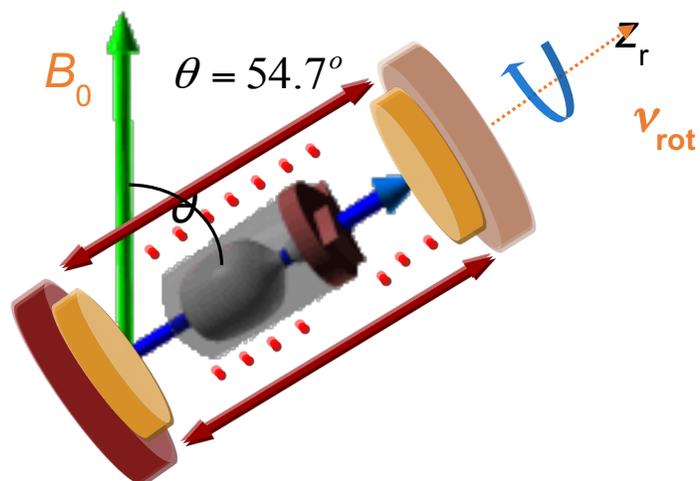
Figure 1-8. The magic angle orientation of 54.7° relative to the direction of the static field (B_0).

The aim os MAS is to average this term to zero. It takes advantage from the fact that the average of the nuclear orientation dependence under spinning can be shown to be

$$\langle 3cos^2\theta - 1 \rangle = \frac{1}{2}(3cos^2\theta_r - 1)(3cos^2\beta - 1)$$

where θ_r is the angle between the spinning axis and the static field $\underline{B}^0$ and β is the angle between the apinning axis and the principal z-axis of the tensor ellipsoid of the nuclear spin interaction. If θ_r is set to be 54.74°, the magic angle, the term $\langle 3cos^2\theta - 1 \rangle$ is zero under MAS conditions (Figure 25).

At present, MAS is the most commom technique to average out firs-order anisotropic interactions in powder samples. Second-order anisotropic interactions are not completely averaged to zero.

1.4.2.2.   STATIC DIPOLAR NMR SPECTROSCOPY

Magnetic dipole-dipole couplings between and those in their vicinity result in a modification of the measured precession frequencies. The effect is distance dependent and anisotropic, depending on the interaction of the internuclear distance vector relative to $\underline{B}^0$, contributing to the NMR line-broadening effects observed in powered samples. There are homonuclear and heteronuclear contributions.

By systems characterized by the average mean square of the local field (the secon moment), which can be related to internuclear distance contributions by the van Vleck formulae (VAN VLECK, 1948).

$$M_{2,homo} = \frac{3}{5}(\frac{\mu_0}{4\pi})^2 I(I+1)\gamma^4 \hbar^2 \sum_{i \neq j} r_{ij}^{-6},$$

$$M_{2,homo} = \frac{4}{15}(\frac{\mu_0}{4\pi})^2 S(S+1)\gamma_I^2 \gamma_S^2 \hbar^2 \sum_S r_{ij}^{-6}$$

Thus homo- or heteronuclear dipolar second moments represent quantitative criteria against which structural models can be tested in a rigorous fashion. In the following sections, various experimentaltechniques for obtaining such dipolar second moments are described and their significance for the structural analysis of glasses is highlighted.

1.4.2.3.   ROTATIONAL ECHO DOUBLE RESONANCE - REDOR

Rotational echo double resonance (REDOR), a powerful experiment is able to provide site-selective dipolar coupling information under the high-resolution conditions afforded by magic angle spinning (GULLION, 1995). In general, the dipolar coupling constant oscillates according to the term sin $\omega_r t$ and is averaged out over the rotor cycle. However if we invert the sign of the dipolar Hamiltonian by applying a π-pulse to the nonobserved I spins somewhere during the rotor cycle, this average is nonzero; the interaction is recoupled and now interferes with the ability of MAS to provide signal refocusing.

Recoupling is accomplished by 180° pulse trains applied to the I spins, while the S spin signal is detected by a rotor-synchronized Hahn spin echo sequence. One measures the normalized difference signal $\Delta S/S_0 = (S_0 - S)/S_0$ in the absence (intensity S0) and presence

(intensity S) of the recoupling pulses. A REDOR curve is then generated by plotting $\Delta S/S_0$ as a function of the dipolar evolution time NTr, i.e., the duration of one rotor period multiplied by the number of rotor cycles. In the limit $\Delta S/S_0 < 0.2$ of short dipolar evolution times, the REDOR curves is found to be geometry independent and can be approximated by

$$\frac{\Delta S}{S_0} = \frac{S_0 - S}{S_0} = \frac{4}{3\pi^2}(NTr)^2 M_2$$

where the average van Vleck second moment can be extracted from a simple parabolic fit to the experimental data.

2. OBJECTIVES

The main objective of this thesis is the development and characterization of glass and novel optical fibers transmitting in the DUV region as an alternative of existing UV silica fiber as well for other UV optical applications. Mixed vitreous compositions based on fluorides (AlF_3, SrF_2, CaF_2 and MgF_2) and phosphates [$(SrPO_3)_2$ or $(BaPO_3)_2$] were determined as the best candidate to attain this objective. In this context, the PhD research activity can be summarized in the following objectives:

a)   Preparation and characterization of fluoride-phosphate glasses with optical transmission below 200 nm, tailored refractive index to ensure light-guiding in the core by total internal reflection process, excellent thermal stability against crystallization and appropriate viscosity to enable fiber drawing.

b)   Develop a suitable methodology for preforms and core-cladding optical fibers (step-index) fabrication.

c)   Structural investigation to describe the glass network and the local environment for luminescent species, important for the development of high efficient UV devices.

3. UV-TRANSMITTING STEP-INDEX FLUOROPHOSPHATE GLASS FIBER FABRICATED BY THE CRUCIBLE TECHNIQUE

The present chapter is based on a manuscript that describes the fabrication of a UV-transmitting step-index fiber based on fluorophosphate glasses fabricated by the adapted crucible technique developed by us. High-purity fluorophosphate glasses were prepared with different phosphate/fluoride ratio and their optical and thermal properties were studied in order to select the most suitable compostion to produce the optica fiber. The fiber fabrication process is described and discussed, as well, the optical losses in the UV region.

RÉSUMÉ DE L´ARTICLE INSÉRÉ

Dans ce travail, on a préparé des verres FP de haute pureté et on a utilisé ces verres pour la fabrication de fibres optique à saut d´indice par la technique du creuset. Dans la première étape, les verres ont été étudiés pour être très transparents dans la région ultraviolette sous vide jusqu'à 160 nm, et ses caractéristiques de viscosité et des températures autour du point de ramollissement ont été caractérisês. Ensuite, les fibres ont été fabriquées par la technique du creuset, dans un assemblage de creuset en silice. Le procédé est approprié pour obtenir des fibres de verre FP sans cristallisation. En outre, les pertes optiques dans la fibre obtenue ont été mesurées dans la région UV.

UV-TRANSMITTING STEP-INDEX FLUOROPHOSPHATE GLASS FIBER FABRICATED BY THE CRUCIBLE TECHNIQUE

Gustavo Galleani*, Yannick Ledemi, Elton Soares de Lima Filho, Steeve Morency,
Gaelle Delaizir, Sebastien Chenu, Jean Rene Duclere, Younes Messaddeq

Institute of Chemistry, Sao Paulo State University/UNESP, Araraquara, SP, Brazil

Center for Optics, Photonics and Lasers, Laval University, Quebec, QC, Canada

Laboratoire de Sciences des Procedes Ceramiques et de Traitements de Surface, Universite de Limoges, Limoges, France

ABSTRACT

In this study, we report on the fabrication process of highly pure step-index fluorophosphate glass optical fibers by a modified crucible technique. High-purity fluorophosphate glasses based on 10 mol% of barium metaphosphate and 90 mol% of metal fluorides (AlF_3-CaF_2-MgF_2-SrF_2) have been studied in order to produce step-index optical fibers transmitting in the deep-ultraviolet (DUV) region. The characteristic temperatures, viscosity around softening temperature and optical transmission in the UV-visible region of the prepared bulk glasses were characterized in a first step. The selected glass compositions were then used to prepare core-cladding optical preforms by using a modified built-in casting technique. While uncontrolled crystallization of the fiber was observed during the preform stretching by using the conventional method, we successfully obtained crystal-free fiber by

using a modified crucible technique. In this alternative approach, the produced core-cladding preforms were inserted into a home-designed fused silica crucible assembly and heated at 643ºC to allow glass flowing throughout the crucible, preventing the formation of crystals. Single index fluorophosphate glass fibers were fabricated following the same process as well. The optical attenuation at 244 nm and in the interval 350-1750 nm was measured on both single index and step-index optical fibers. Their potential for using in DUV applications is discussed.

Keywords: Glass, Fibers, Fluorophosphate, Crucible method, UV transmitting materials

3.1.   INTRODUCTION

The development of new optical fibers capable of operating in the ultraviolet (UV) region would benefit the fast remote elemental analysis of non-metallic elements of first environmental or industrial importance. For instance, elemental phosphorus exhibits its principal emission lines in the vacuum-UV region (VUV, < 200 nm) at 177.50, 178.29 and 178.77 nm, or a less sensitive one in the deep-UV region (DUV, < 300 nm) at 213.62 nm [1] Laser-induced breakdown spectroscopy (LIBS) has been applied for elemental detection for solid, liquid or gas samples [2] where powerful laser pulses are used to form a microplasma or a spark on the sample to analyze. An optical fiber can be then employed to remotely collect and transmit the plasma/spark light from relatively long distances to the detection system to quantify the emitting species [3-5] The well-established commercial UV-transmitting optical fibers are based on high-OH-silica glass. However, the latter is usually rapidly damaged under UV light exposure owing to absorption by pre-existing or radiation induced defects, causing an abrupt increase of the absorption losses below 250 nm [6-8]. This restricts thus their use for a short-period and a periodic replacement is required for these fibers. As long-term stability of light transmission is highly desirable in optical system design, the development of alternative UV-transmitting optical fibers is of major importance.

Glasses based on beryllium fluoride or aluminum and alkaline earth metal fluorides with wide band gap exhibit an extended optical transmission in the UV down to 160 nm [9,10]

31

[9,10]. However, on one hand beryllium fluoride is extremely toxic and its use is discouraged. On the other hand, fluoroaluminate glasses are known for their tendency to crystallize upon heating up to drawing temperature due to reaction of the glass with moisture in the processing environmental atmosphere, limiting the fabrication of vitreous fiber [11]. Since these disadvantages result primarily from the strong ionic character of fluoride glasses, considerable progress in the glass forming ability can be made by the addition of small amount of phosphate. Fluorophosphate glasses produced by mixing fluorides (mainly, AlF_3 and MF_2, M= Sr, Ca, Mg, Ba) and phosphates ($Sr(PO_3)_2$, ($Ba(PO_3)_2$, $Al(PO_3)_3$ and $NaPO_3$), were extensively studied [12-16]. These mixed glasses have shown a combination of many desirable properties from the phosphate and fluorides components, including excellent glass-forming abilities, low refractive indices, low partial dispersion, and broad transmission window ranging from ~ 160 nm to 4000 nm. Optical transmission in the deep-UV is only achieved when the glasses are prepared from ultra-high-purity starting materials, since the main limitation is the extrinsic absorption by transition metal impurities in the ppm range [13-15]. Unlike silica glass, fluorophosphate glasses with low phosphate content and ultra-high chemical purity may exhibit low loss transmission in the UV region owing to the absence of absorption/scattering defect centers [17,18]. Achieving ultra-low losses in fluorophosphate glass fibers similar to those attained in silica fibers (whose technology is mature nowadays), might open new possibilities for UV-transmitting optical fibers for the above mentioned applications. For a better understanding, it is worth distinguishing here the terms highly pure and low loss from ultra-highly pure and ultra-low loss, respectively. The former stands for optical materials prepared from starting materials of 5N chemical purity or higher (i.e. with impurity levels in the ppm range) while the latter stands for materials of higher purity (i.e. with impurity levels in the ppb range). Moreover, ultra-highly pure fluorophosphate glasses may also show a better long-term radiation resistance to UV light [19] since their optical basicity (electron donor power of the glass matrix) is lower in comparison with silica glass, due to a lower content of non-bridging oxygens when the phosphate content is low. The UV radiation damage of such glass is known to be directly related to the amount of phosphate groups and the presence of metallic impurities within the glassy network [15,16,18-21].

Very few studies on the fabrication of fluorophosphate glass optical fibers have been reported in the literature [17,18,22,23]. Zou et al. produced step-index fibers by drawing at

32

the optical tower an ultra-highly pure core-cladding preform obtained by extrusion in the system P_2O_5–AlF_3-YF_3-MgF_2-RF_2-NaF, (R=Mg, Ca, Sr and Ba). The minimum loss they measured in the UV was 0.11 dB/m at 365 nm [17]. Kalnins et al. have prepared an unclad optical fiber by drawing preforms produced by extrusion under nitrogen of a commercial fluorophosphate glass (N-FK51A). Although they reported on preform neck-down crystallization issues during the drawing, they achieved minimum losses of 3.05 dB/m at 405 nm after increasing the preform feed-rate and drawing speed [22]. They also showed that treatment of extruded preforms prior to fiber drawing further improved optical fiber loss to 0.5-1 dB/m[23].

In this paper, we report on the fabrication of high-purity fluorophosphate glass optical fibers transmitting in the UV. We optimized the fluoride/phosphate ratio content to achieve a highly transparent glass in the DUV region with a large thermal stability against crystallization for further fiber drawing. Core-cladding preforms were first prepared by a modified built-in casting method [24,25]. As we faced surface crystallization issues during fiber drawing from the preforms, an alternative fiber fabrication process was then implemented. This approach, derived from the well-known double crucible method [26-32], consisted in drawing the core-cladding fibers from the as-prepared preforms throughout a simple crucible. Finally, the optical transmission losses in the UV and IR regions of the successfully produced fibers were measured and the potential of this new fiber fabrication process was discussed.

3.2. EXPERIMENTAL PROCEDURE
3.2.1. Bulk glass synthesis

Fluorophosphate vitreous samples of compositions $10Sr(PO_3)_2$-$90(AlF_3$-CaF_2-MgF_2-SrF_2) and $xBa(PO_3)_2$-100-$x(AlF_3$-CaF_2-MgF_2-SrF_2), with x = 5, 10 and 20 mol% were prepared by the conventional melt-quenching method from mixed high-purity fluorides, AlF_3 (MV labs, 99.999%), SrF_2 (Sigma, 99.995%), CaF_2 (Sigma 99.99%), MgF_2 (Cerac, 99.999%) and metaphosphate $M(PO_3)_2$ (M=Ba and Sr). High-purity barium and strontium phosphates were prepared from the solid state reaction of $NH_4H_2PO_4$ (Sigma, 99,999%) with MCO_3 (Alfa Aesar, 99,994%):

$$MCO_3(s) + 2(NH_4)H_2PO_4(s) \rightarrow M(PO_3)_2(s) + CO_2(g) + 3H_2O(g) + 2NH_3(g).$$
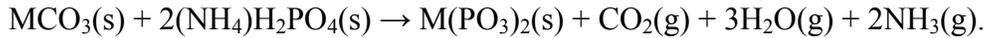
The mixed powders were loaded in a platinum crucible, heated at 250ºC at a rate of 5 °C.min^{-1} and kept at this temperature during 24 h to allow a complete reaction of the precursors. The mixture was subsequently heated at 500ºC in an electric furnace for 1 hour to eliminate the gas in excess formed during the reaction. After the reaction, the appropriate amount of the corresponding metaphosphate was mixed with the fluorides starting materials, loaded into a capped carbon crucible and melted at 1000°C in an induction furnace. The resulting liquid was kept at this temperature for 30 minutes to ensure fine homogenization. Finally, the melted glasses were cooled rapidly in a brass mold at the glass transition temperature. The glass was then placed into a resistive oven at the annealing temperature for 4 hours and subsequently cooled down to room temperature in approximately 10 hours to remove any residual stress induced during the quenching. The glass samples were polished using silicon carbide polishing paper with decreasing grit size (400, 600, 800, 1200) before using a 1 micron diamond suspension to obtain a good surface quality for optical characterization.

3.2.2. Core-cladding preform preparation and optical fiber drawing:

As mentioned in the introduction, an alternative method was implemented to produce the step-index fluorophosphate glass fibers. This method, which will be discussed in more details later, consists in two successive steps: (i) the fabrication of core-cladding preforms by the conventional build-in casting method [24,25] and; (ii) the drawing of the step-index fibers from the as-prepared preforms through a fused silica crucible. First, to prepare the core-cladding preforms, cylindrical glass tubes with the cladding composition [10Sr(PO$_3$)$_2$-90(AlF$_3$-CaF$_2$-SrF$_2$-MgF$_2$)] were first prepared. Then, cylindrical glass rods with the core composition [10Ba(PO$_3$)$_2$-90(AlF$_3$-CaF$_2$-SrF$_2$-MgF$_2$)] were prepared separately, either following in a two-step discontinuous melting system. For both glass tubes and rods, the raw

materials were first pre-melted at 1000˚C for 30 min, like for the bulk glass synthesis (see section 2.1). Then, the glasses were re-melted under vacuum at 730ºC for 1 hour and poured into a cylindrical brass mold preheated at the glass transition temperature and annealed at the same temperature for 6 hours. To produce the glass rods for the preform core, a cylindrical mold of 5 mm inner diameter was employed. To produce the glass tube for the preform cladding, a modified built-in casting technique was used [24]: (i) the glass is cast into the preheated mold of 10 mm inner diameter and begins to solidify in contact with the mold walls; (ii) a shutter placed below the mold is then opened, allowing the part of the glass which is still liquid (center of the cylinder) to flow away, forming a glass tube and; (iii) the same shutter is closed once the tube has solidified with the desired diameter and length.

Second, to produce the fibers, the glass rod was manually inserted into the glass tube and the as-assembled core-cladding preform was then loaded into the fused silica crucible, as illustrated in the figure 3-1. The assembly was then placed into the drawing furnace while argon gas was flowing around the crucible. The temperature of the furnace was raised to 672ºC (Tg + 222˚C) for a period of 20 min to allow the glass to flow to the crucible nozzle (out of the heating zone of the furnace). The furnace temperature was then lowered to 643ºC (Tg + 193˚C) and the fiber drawing process was started. It is worth mentioning that the temperature values given here are those read by the temperature controller in the furnace. The actual temperature of the glass within the crucible may be slightly different. During that process, a low-index UV-cured polymer coating (DeSolite® DF-0007) was applied to the fiber surface to improve its mechanical resistance.

A single-index fiber coated with the low-index UV-cured polymer jacketing was also produced by the same method, drawing a rod with the core composition.
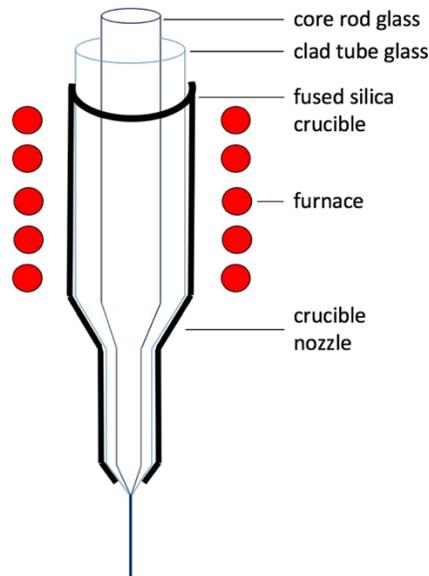
Fig. 3-1. Fused silica crucible assembly used for fiber drawing.

3.3. Material Characterization

3.3.1. Thermal characterization:

Differential scanning calorimetric (DSC) measurements were performed using a Netzsch DSC Pegasus 404F3 apparatus on 25 mg glass pieces into Pt pans at a heating rate of 10 °C.min^{-1} up to a temperature of 750ºC under nitrogen atmosphere.

Temperature dependence of viscosity in the range 10^7-10^{11} Poise was measured with a Bansbach Easylift Theta US parallel plate high temperature viscometer. Cylindrical samples were slices cut from annealed glass rods with 10 mm diameter and 6 mm thickness and sandwiched between two silica plates inside a well-insulated furnace under nitrogen flow and heated at a heating rate of 2°C/min, under a compressive load of 300g. By means of recording the rate of the thickness change of the sample as a function of time (using a linearly variable differential transformer (LVDT)), the logarithm of viscosity *vs* temperature is determined by the Dilasoft program. The estimated error was about ± 3°C on the temperature values and ~$10^{\pm0.2}$ Poise on the viscosity values.

3.3.2. Optical Characterization:

Glass sample transmission spectra have been measured by using a UV-VIS-NIR Varian Cary 5000 double beam spectrophotometer from 185 to 800 nm on polished samples. Since oxygen from ambient atmosphere absorbs in the range 185-200 nm, an adapted nitrogen purge was used in the sample chamber for the measurements.

Linear refractive index n has been extracted from ellipsometry measurements, using a Horiba Jobin-Yvon UVISEL Extended Range spectroscopic ellipsometer, operated in the 200 – 800 nm wavelength range. The angle of incidence was fixed at 60° and the light spot size was 1 mm in diameter.

The fiber transmission losses were measured at the wavelength $\lambda_1 = 244$ nm and in the range 350 nm $\leq \lambda_2 \leq$ 1750 nm. For the measurement at λ_1, a Coherent Innova 300c laser was used as optical source. The laser beam was chopped at 1 kHz using a Thorlabs MC2000 optical chopper. The input and output of the fiber were manually cleaved. A CaF_2 lens of 40 mm focal length was used to inject light into the fiber, which was placed in a clamp in a three-axis fiber coupling stage. The distal end of the fiber was clamped into a SMA adaptor, which was used both for fiber alignment, as well as to block stray light. The fiber output power was detected using a Si photodiode S120VC from Thorlabs, interrogated by a Thorlabs PM100D power meter and a Lock-in amplifier SR830 DSP, from Stanford Research. For the broadband measurement, the input of the optical fiber was clamped at the focus of an in-house built tungsten-halogen lamp housing, and the output connected directly to an optical spectrum analyzer (OSA), Yokogawa AQ-6315A. In both measurements, the fiber was cut in several sections, and the output power was measured for each section. This allows obtaining accurate transmission losses through a multiple-point cut-back method.

3.4. RESULTS AND DISCUSSION
3.4.1. Bulk glasses characterization.

In mixed fluorophosphate glass systems, it is known that an increase of the phosphate content results in decreasing the optical transmission in the UV region, since the phosphate

content decreases the band gap energy [14]. Therefore, to produce a fiber transmitting deeper in the UV, one has to consider a glass with good thermal stability with a phosphate content as low as possible. For this reason, three fluorophosphate glass samples containing 5, 10 and 20 mol% of phosphate were prepared and characterized to select the most appropriate composition for further fiber drawing tests.

Figure 3-2 shows the DSC curves obtained for the glasses $xBa(PO_3)_2$-100-x (AlF_3-CaF_2-SrF_2-MgF_2) with x = 5, 10 and 20 mol%, labelled as 5BaPF95, 10BaPF90 and 20BaPF80, respectively. An important factor to consider prior to any fiber drawing is the thermal stability against crystallization $\Delta T = Tx - Tg$, where Tg is the glass transition temperature determined from the endothermic baseline shift of the DSC curve while Tx is the onset temperature for the first crystallization exothermic peak. The larger is ΔT, the lower is the risk of observing formation of crystals while drawing the fiber, taking into account that the drawing temperature (643˚C here), which depends on the viscosity vs temperature behavior, is relatively far from the crystallization temperature Tx (748˚C here). The Tg increases from 439°C to 460°C with increasing phosphate content while the crystallization peak broadens, which can be related to an increase of the glass forming ability due to the insertion of more covalently bonded PO_4 groups in the fluoroaluminate structure. In the fluoroaluminate glasses, AlF_6-octahedra connected by shared corners are proposed as the main glass forming entity [33]. In the fluorophosphate glasses, the structure consists of interconnected $Al(O/F)_6$–octahedra and PO_4-tetrahedra cross-linked by modifier cations, which increases the rigidity of the structure, limiting and slowing the nucleation process [34,35]. For the 5BaPF95 and 10BaPF90 samples, the thermal stability is 95 ºC and 149 ºC, respectively, and for the 20BaPF80 sample, the onset of crystallization is difficult to be precisely determined, as can be seen in figure 3-2. The glass 10BaPF90, with higher thermal stability compared with 5BaPF95, has been chosen for the core-cladding step-index fiber fabrication, and $Ba(PO_3)_2$ was replaced by $Sr(PO_3)_2$ in the cladding glass composition (labelled 10SrPF90) to decrease its refractive index in view of preparing a step-index glass preform.
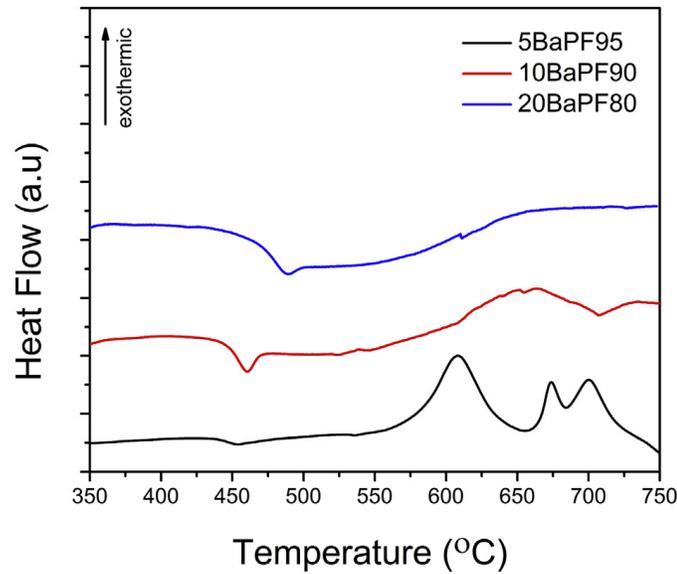
Fig. 3-2. DSC curves of the studied fluorophosphate glasses $xBa(PO_3)_2$-90-x$(AlF_3,$ $CaF_2,$ $MgF_2,$ $SrF_2),$ x = 5, 10 and 20 mol%, respectively labelled as 5BaPF95, 10BaPF90 and 20BaPF80.

The transmission spectra from the DUV-visible to the infrared region of the glass samples selected for the fabrication of the core-cladding step-index fiber are shown in figures 3-3a and 3-3b, respectively. In the literature, an intrinsic VUV edge of fluorophosphate glasses containing 10 mol% of phosphate was reported at 160 nm [36]. The same authors also pointed out the strong influence of extrinsic absorptions from transition metal impurities present in the glasses on their VUV cut-off edge. In the present work, the transmission in the UV region reaches 90% above 240 nm and is nearly 75% at 180 nm (below this wavelength, a special equipment for the vacuum ultraviolet region is needed). At 220 nm, a small absorption peak is observed, which is due to Fe^{2+} impurity absorption. Iron is the main trace impurity of fluoride and phosphate raw materials. Erht et al. have shown that glasses melted under reducing conditions possess better transmittance in the UV, since the redox state of iron traces, Fe^{3+} (absorption band at 250 nm and 185 nm), can be almost completely shifted to Fe^{2+} (absorption band at 220 nm and 170 nm) with lower molar absorption coefficient $\varepsilon_{i\lambda}$ ($cm^{-1}.ppm^{-1}$) [37]. Even small amounts of iron impurities (ppm range) can cause high optical losses in the final glass and fiber. To our knowledge, the transmission spectra presented here are comparable to the best results reported in the literature on fluorophosphate bulk glasses

of 2 mm thickness [36]. In the latter work, glasses showing about 80% of transmission at 200 nm were produced from high purity starting materials and the final iron content in the glass was measured to be 6 ppm.

The absorption coefficient α_{220nm} at 220 nm was determined from the transmittance spectrum. By using the Beer-Lambert law.

$$\alpha = \ln\left(\frac{T_0}{T}\right)/l \tag{1}$$

where l, T_0 and T represent the sample thickness, the maximum transmittance (%) of the glass matrix and the transmittance at 220 nm, respectively. For the cladding glass (10SrPF90), $\alpha_{220} = 1.25$ cm^{-1} and for the core glass (10SrPF90) and $\alpha_{220} = 1.54$ cm^{-1} (10BaPF90).

In the IR region, the transmission reaches 91% and extends up to 4000 nm. The absorption peak around 3000 nm is ascribed to O-H stretching. The infrared edge at 4500 nm is due to the P-O vibration [38].
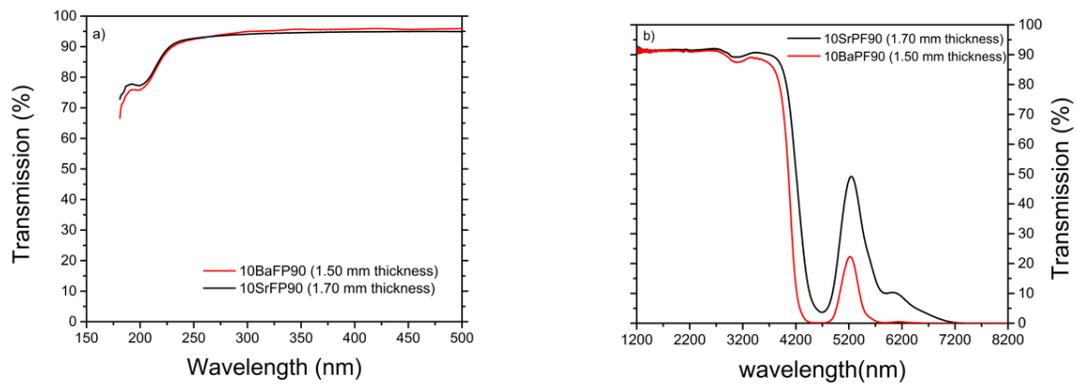
Fig. 3.3. (a) Deep-UV and (b) infrared transmission spectra, for the core and cladding glasses with 1.50 and 1.70 mm thickness, respectively.

The evolution of the refractive index measured on the core and cladding glasses as a function of wavelength is shown in figure 3-4. Measuring the refractive index in the UV region is a complex task. Here, ellipsometry that reflects polarized light from bulk sample and detects the change in polarization introduced by the sample structure was used to

reconstruct the index profile. The curve for the core and cladding glass was fitted by using the Cauchy dispersion formula:

$$n(\lambda) = A + \frac{B}{\lambda^2} + \frac{C}{\lambda^4}$$

The coefficients associated with the curve are A = 1.45599, B = 7.457x10^{-16} m^2 and C = 1.2874x10^{-28} m^4 and A = 1.44794, B = 7.2197x10^{-16} m^2 and C = 1.12542x10^{-28} m^4 for the core (10BaPF90) and cladding (10SrPF90) glass, respectively. It is worth noting that the Cauchy formula was preferred here to the Sellmeier formula which is generally used to fit the refractive index wavelength dispersion in a broader range. However, here, we measured the dispersion only in the UV-visible range of interest, and the Cauchy dispersion proved to display a better fitting than the Sellmeier dispersion, compared to the experimental data. The index difference between the core and cladding glasses is 0.013 at 244 nm, which corresponds to a numerical aperture of 0.19. Thermal and optical properties of the glasses are summarized in table 3.1.

Table 3.1. Main characteristics of the glasses under study, including glass transition temperature Tg, onset temperature of crystallization Tx, thermal stability against crystallization ΔT = Tx-Tg and linear refractive index n at 250 nm (determined from ellipsometric measurement).

Glass label	Composition (mol%)						Tg (±2°C)	Tx (±2°C)	ΔT = Tx – Tg (±4°C)	n at 250 nm
	Ba(PO$_3$)$_2$	Sr(PO$_3$)$_2$	AlF$_3$	CaF$_2$	MgF$_2$	SrF$_2$				
5BaPF95	5	-	38	25	11	21	439	534	95	-
10BaPF90	10	-	35	30	10	15	450	599	149	1.505
20BaPF80	20	-	32	21	9	18	460	-	-	-
10SrPF90	-	10	35	30	10	15	447	597	150	1.492
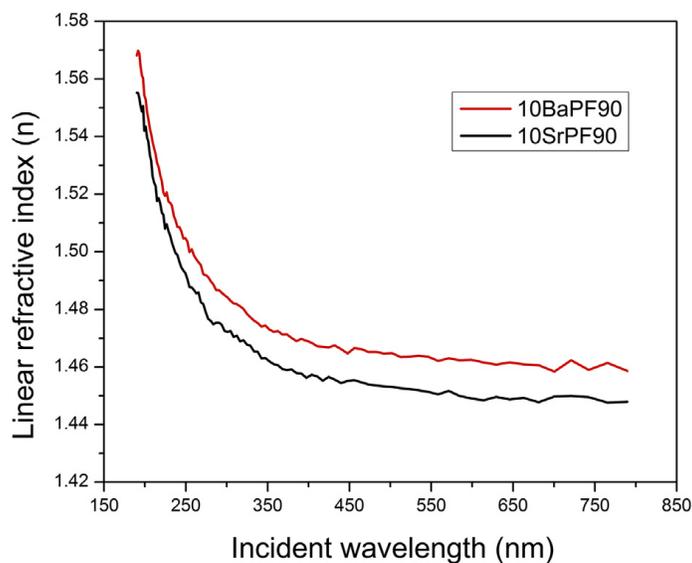
Fig. 3-4. Dispersion curves for the core (10BaPF90, red line) and cladding (10SrPF90, black line) glass compositions, determined from ellipsometry measurements.

3.4.2. Core-cladding glass preform fabrication and fiber drawing.

The two principal methods known to fabricate optical fibers are the solid glass preform drawing and the double crucible technique. The first technique requires to prepare a solid glass preform of desired dimensions, geometry, structure, etc. that will be further stretched at the optical fiber drawing tower at a temperature corresponding to a specific viscosity, as discussed later. Such technique is widely employed to draw vitreous materials which are highly stable against crystallization *vs* temperature. Nevertheless, surface crystallization or formation of bubbles issues while drawing the preform into fiber can eventually occur even with highly stable glassy materials, such as the fluorophosphate glasses under study here. In the second method, the double crucible technique, core and cladding glasses are prepared separately to feed each crucible, one for the core and the other for the cladding, where they are heated at a larger temperature than in the previous method to enable the flowing of both core and cladding glasses through the crucible. Such approach not only permits to limit the surface crystallization issues, but it may also improve the quality of core/cladding interface. This method, well-known in the field of optical fiber fabrication but rarely employed because

of its complex implementation, was first designed for fluoride glasses more than 30 years ago [27]. It was also employed to produce oxyfluoride fibers [28] and more largely for the fabrication of step-index chalcogenide soft glasses for infrared applications [29-32]. Nevertheless, such method is rather more complex to implement from a practical point of view than the first one.

To prepare solid glass preforms, a core-cladding preform in our case, the main techniques are the extrusion technique [17,39] and the rod-in-tube technique which implies the use of the rotational or the build-in casting techniques to form the cladding glass tube [24,25]. In this work, a modified build-in casting technique similar to that reported in [24] was used. Prior to the core-cladding preform fabrication, a re-melt of the glasses under vacuum step was applied, as described in section 2.2. Indeed, a release of gas followed by the formation of bubbles (probably coming from dissolved gas in the glass melt) was observed in the first attempts to draw the fibers from the preforms, causing many imperfections in the fibers. The re-melt step has permitted to decrease the amount of gas dissolved in the melt that seems to be less soluble at lower temperature (700°C in the re-melt step) than at higher temperatures (1000°C in the first melt step), improving the fiber quality. Perhaps HF gas is released at higher temperature and trapped after glass formation.

The cladding tube and the core rod glass preform used for drawing are shown in figure 3-5. The length of the preforms was about 11 cm. For the tube, the external and internal diameters are 10 and 5 mm, respectively (fig. 3.5a), for the rod the diameter was 4 mm (fig. 3.5b).
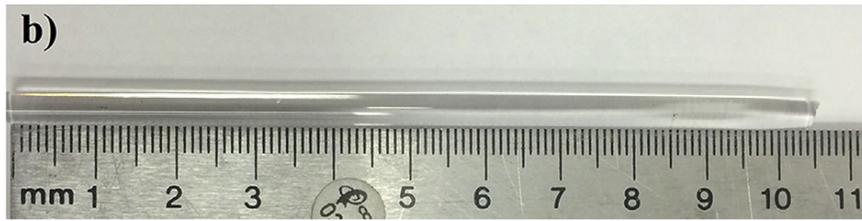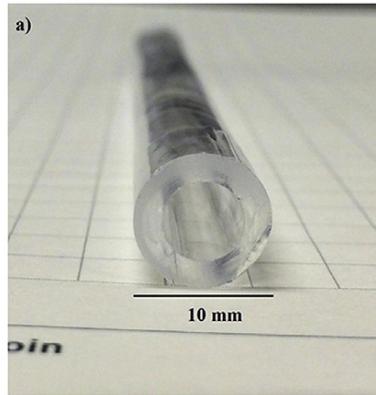
Fig. 3-5. Photographs of the cladding glass tube (a) and the core glass rod (b).

The DSC curve and the viscosity data near glass softening point recorded on the core glass (10BaPF90) and cladding glass (10SrPF90) are shown in figure 3-6. The co-drawing of two glass materials of different compositions usually requires an excellent matching of their thermal properties, including viscosity vs. temperature. Key parameters as thermal stability against crystallization and viscosity(η) vs temperature(T) are used to evaluate the glass forming ability and the range of temperature for fiber drawing [40]. The glass transition temperatures Tg measured on the 10SrPF90 glass tube and the 10BaPF90 glass rod are 447 °C and 450°C, respectively while their thermal stability against crystallization are 150 °C and 149°C, respectively. Such thermal stability is well above the 100°C usually considered as a minimum value to allow glass stretching without crystallization.
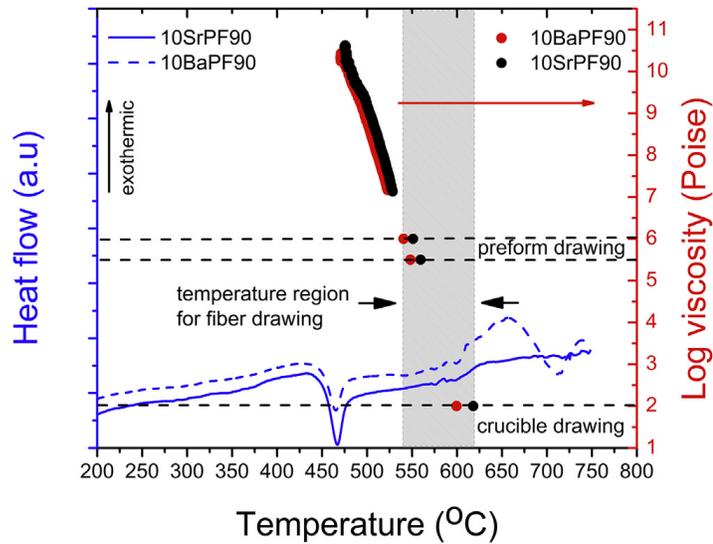
Fig. 3-6. DSC traces and viscosity recorded by the parallel plate method as a function of temperature of the core (10SrPF90, black line) and cladding (10BaPF90, red line) glass compositions. The heating rate was 10˚C/min for the thermal analysis and 2˚C/min for the viscosity measurement.

The evolution of log (η) vs T (Poise/°C) near the glass softening region is approximately linear, as the Arrhenius approximation applies and decreases rapidly with increasing temperature. Depending on the method used to draw optical fibers, i.e. preform drawing or crucible technique, the required glass viscosity is not the same. In the crucible technique, a low viscosity varying around 10^2-10^3 Poise is needed as the glass has to flow through the crucible whereas a slightly larger viscosity ranging between $10^{5.5}$-10^6 Poise enables the fiber drawing from the glass preform. After extrapolating the viscosity curves recorded as a function of temperature, we can obtain the intercepts of the temperatures accordingly with the required viscosities corresponding to each method, as depicted in figure 3-6. Fiber fabrication from preform drawing is therefore expected to be achieved around 540-560˚C whereas a temperature of about 600-620˚C will be necessary to produce fiber through the crucible technique. As can be seen in figure 3-6, these estimated temperatures for fiber drawing are very close to the onset of crystallization as determined for the core and cladding glasses by DSC, 597°C and 599°C, respectively. It is worth reminding that the heating rates used for each characterization technique were different (10°C/min for the DSC and 2°C/min

for viscosity measurements). Nevertheless, a large change of viscosity with respect to a small variation of temperature is clearly observed here. Minimizing the time spent by the preform at the drawing temperature was therefore considered as a crucial requirement to avoid crystallization during the fabrication process, as well as using a fast drawing rate and a small hot zone in the drawing furnace.

From an experimental point of view, the first avenue explored to produce the fluorophosphate fibers was by simply drawing core-cladding optical preforms. However, despite the fact that this method seemed to be successful in the work of Zou *et al.* [17,18], we were not able to draw a crystal-free optical fiber from neither a core-cladding preform nor a single index preform. On the contrary, we rapidly faced serious problems of uncontrolled crystallization at the surface of the fiber during the fiber drawing process, similar to those reported by Kalnins *et al.* [22]. Surface crystallization issues were also reported in fluoroaluminate glass fiber drawing and ascribed to moisture attack followed by surface devitrification along the drawing process [41]. It is worth mentioning that the purity of the starting materials used in the work of Zou was similar to that of our used precursors (4N or above). We can thus assume that the precursors' purity is not playing a role in the crystallization issues observed during the preform drawing. Our first attempts were conducted under dry nitrogen atmosphere around 545°C and it was not possible to draw fiber pieces longer than around 2 meters because of the formation of crystals which dramatically degrade the fiber strength.

After numerous unfruitful trials varying the process parameters (temperature, preform feeding speed, time spent in the drawing furnace, nature and pressure of gas, etc.) where crystallization traces were always observed in the preform neck-down and the drawn fibers, the use of an alternative approach was found to be more successful. This alternative method consisted in drawing the core-cladding preform through a home-made fused silica crucible. To some extent, this method combines both the techniques above described. The core-cladding preform was thus inserted in a cylindrical fused silica crucible and heated at 643°C, which is slightly above the temperature corresponding to the 10^3–10^2 Poise viscosity required for the crucible technique. The fiber was then rapidly drawn from the outflow of the nozzles at the bottom of the silica crucible. No trace of crystallization was observed to the naked eye

neither on the fiber, nor on the preform neck-down. About ten meters of crystal-free fibers were successfully and reproducibly produced from the 11 cm length preforms. Careful adjustments of the drawing process permit to control the core-cladding diameter ratio of the produced fibers. All the fibers produced were coated during the process with low index UV-cured polymer. A fiber cross-section image of the step-index fiber obtained by this modified crucible technique is shown in figure 3-7. The outer (cladding) and inner (core) diameters are 127 μm and 68 μm, respectively. Single-index fibers of same diameter made of 10BaPF90 glass were also produced by the same technique (not shown here).
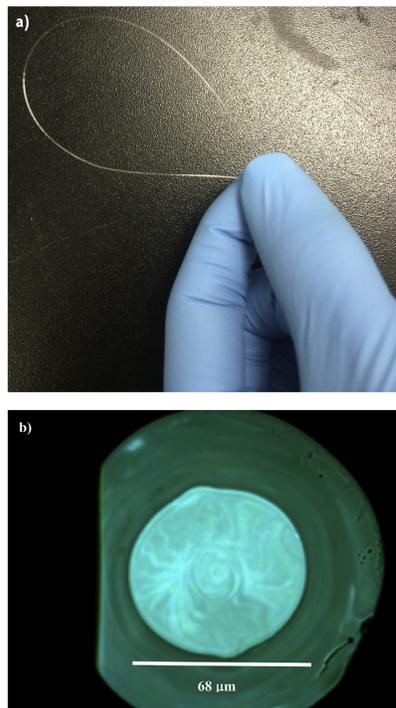
Fig. 3-7. Photograph of the fabricated optical fiber (a). Optical microscopy image of the optical step-index fiber section (127 μm diameter) without polymer coating (b).

The reason why this alternative technique has permitted to eliminate the surface crystallization during the fiber drawing still remains unclear and is currently under investigation. We believe that the risk of crystallization was strongly reduced by the combination of a higher temperature than that used in the preform drawing technique and the absence of contact of the outer preform surface with surrounding argon atmosphere.

Nonetheless, this technique paves the way for drawing optical fibers from various exotic glasses that were initially discarded because of their strong tendency to crystallize during their drawing (e.g. fluorides, fluoroaluminates, etc.). The compatibility of the preform glass with the fused silica of the crucible at relatively high temperature (glass viscoelastic regime) also has to be considered. Surprisingly, no reaction between the fluorophosphate glass and the silica crucible was evidenced. Although the reusing of the silica crucible is difficult because removing all the residual fluorophosphate glass after drawing is not possible, unless by heating it at melting temperature, which results in strong interaction with the crucible walls.

As above mentioned, about 10 meters of crystal-free step-index fiber with homogeneous diameter can be fabricated with reproducibility from one single preform. For the optical losses characterization carried out by the cut-back technique, two different sections of optical fibers were used: the first one was initially of 6.5 m for the measurements in the 350 nm $\leq \lambda_2 \leq$ 1750 nm range and the second one of 0.2 m for the measurement at $\lambda_1 =$ 244 nm. Such short piece of fiber had to be used to enable the detection of the output power in the DUV. As presented in the figure 3-8, the optical losses at 244 nm were calculated to be 63 dB/m from the output intensity measured as a function of fiber length.
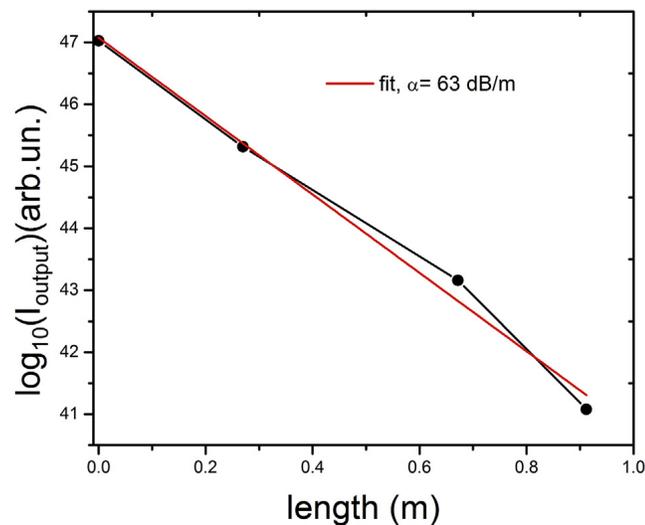
Fig. 3-8. Measured power output at 244 nm wavelength, recorded from a fiber initial section of 0.2 m. In red: best fit of the attenuation curve, weighted to the linear intensity of the signal.

The optical attenuation spectrum recorded from the step-index fiber in the range 350 nm $\leq \lambda_2 \leq$ 1750 nm is presented in figure 3-9. For comparison, the same measurements were carried out on the single-index fibers fabricated. In the latter case, the low index polymer was intended to play the role of the optical cladding to enable light guiding by total internal reflection within the FP fiber. The losses decrease monotonously from 42 to 20 dB/m in the range 407-1750 nm. At 350 nm, an abrupt increase in the losses is observed possible because of metal impurities. For the single-index fiber, a similar behavior was observed but the total losses are approximately lower by an order of magnitude, from 5 dB/m to a minimum of ~0.7 dB/m. The high losses measured on the core-cladding fiber compared to the single-index fiber are probably due to extrinsic losses caused by imperfections in the core glass/clad glass interface. Optical microscope inspection of the fiber has revealed the presence of bubbles. Moreover, glass striae can be clearly observed (figure 3-7) in the core of the fiber, causing background absorption of light and increasing thus the losses. Work is ongoing to improve the fabrication process and eliminate these striae.
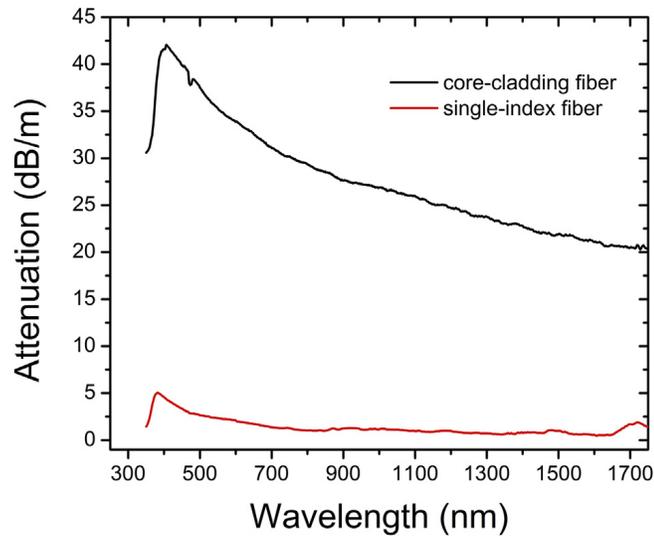
Fig. 3-9. Attenuation spectra of the single-index fiber (red curve) and core-cladding fiber (black curve) measured by the cut-back method on 3 fiber sections.

49

In the literature, as above mentioned, only four works dealing with the fabrication and optical characterization of fluorophosphate glass fibers was reported, to the best of our knowledge [17,18,22,23]. In their work, Zou *et al.* from Hoya Corporation reported ultra-low losses in their fibers with a minimum loss in the UV of 0.11 dB/m at 365 nm while extrinsic absorption bands were observed due to the presence of transition metal impurities at 340 nm (Fe^{3+}), 520 nm (Cr^{3+}, Ni^{2+}) and 800 nm (Cu^{2+}, Fe^{2+}) [17,18]. Second, Kalnins *et al.* reported in 2011 and 2016 minimum loss values in the violet at 405nm of 3.05 dB/m and 0.5-1.0 dB/m, respectively, from single-index fibers drawn from commercial fluoride-phosphate glasses (Schott N-FK51A). They systematically observed crystallization in the neck-down of the preform in each fiber drawing trial, like in our first experiments of drawing from the glass preforms. Their best results were achieved after improving the drawing process parameters [20] (e.g. by increasing the preform feed rate and drawing speed) and the preform surface quality [21]. In our work, the transmission losses measured on the single-index fiber, shown in figure 3-9, are in the same range (i.e. between 1 to 5 dB/m).

Therefore, the optical quality of the core-cladding fluorophosphate glass fibers has to be improved for the targeted applications in the VUV and DUV regions (e.g. fast remote elemental analysis of non-metallic elements as phosphorus). On one hand, the fabrication process through the modified crucible technique is still under development. On the other hand, important efforts are requested to remove specific impurities in the glass precursors: their concentration of transition metal ions like iron, nickel, copper and cobalt have to be reduced to below 10 ppb. A higher transmittance in the UV region would be then expected in these fluorophosphate glass fibers, making them suitable candidates for optical materials capable to operate in the VUV and DUV regions. In parallel, numerical simulations considering the specific optical features of the fluorophosphate glasses are also ongoing to propose a simple design of microstructured hollow core fiber exhibiting an enhanced UV-light transmission.

3.5.   CONCLUSION

Highly-pure fluorophosphate glasses with 10 mol % of barium polyphosphate and 90 mol% of fluorides have been prepared and showed to be suitable for fiber drawing thanks to their excellent thermal stability against crystallization of 149°C. The studied bulk glasses also present optical transparency extending in the deep-UV region down to 180 nm, exhibiting a small absorption peak in this region due to the presence of Fe^{2+} traces impurity. Core-cladding preforms were produced by a modified built-in casting method. Step-index and Single-index optical fibers were then successfully fabricated from the as-prepared preforms through a fused silica crucible assembly. This alternative approach has permitted to get rid of the surface crystallization issues occurring during the drawing process and may pave the way to further fiber fabrication from glasses with strong tendency to surface crystallization. An optical attenuation of 63 dB/m and 20-42 dB/m was measured on the produced step-index fibers at 244 nm and in the range 407-1750 nm, respectively. For the single-index fiber, the optical losses in the range 407-1750 nm were measured to 0.7 to 5 dB/m.

Despite the requested improvements in terms of glass chemical purity or fiber optical quality to envisage future optical applications using these fibers, the alternative fiber fabrication approach proposed in this work constitutes one avenue to address the challenges inherent to the complex fabrication of fluorophosphate glass fibers for photonics.

3.6. References

[1] B. Welz, M. Sperling, Physical Principles, in: At. Absorpt. Spectrom., Wiley-VCH Verlag GmbH, 1998: pp. 63–102.

[2] R.S. Harmon, R.E. Russo, R.R. Hark, Applications of laser-induced breakdown spectroscopy for geochemical and environmental analysis: A comprehensive review, Spectrochim. Acta - Part B At. Spectrosc. 87 (2013) 11–26.

[3] R.E. Neuhauser, U. Panne, R. Niessner, Utilization of Fiber Optics for Remote Sensing by Laser-Induced Plasma Spectroscopy (LIPS), Appl. Spectrosc. 54 (2000) 923–927.

[4] S. Palanco, C. López-Moreno, J.J. Laserna, Design, construction and assessment of a field-deployable laser-induced breakdown spectrometer for remote elemental sensing, Spectrochim. Acta - Part B At. Spectrosc. 61 (2006) 88–95.

[5] R. Noll, H. Bette, A. Brysch, M. Kraushaar, I. Mönch, L. Peter, V. Sturm, Laser-induced breakdown spectrometry — applications for production control and quality assurance in the steel industry, Spectrochim. Acta Part B At. Spectrosc. 56 (2001) 637–649.

[6] M. Oto, S. Kikugawa, N. Sarukura, M. Hirano, H. Hosono, Optical Fiber for Deep Ultraviolet Light, 13 (2001) 978–980.

[7] A.N. Gurzhiev, L.K. Turchanovich, V.G. Vasilchenko, V.A. Bogatyrjov, V.M. Mashinsky, Radiation damage in optical fibers, Nucl. Instruments Methods Phys. Res. Sect. a-Accelerators Spectrometers Detect. Assoc. Equip. 391 (1997) 417–422.

[8] K.-F. Klein, C.P. Gonschior, D. Beer, H.-S. Eckhardt, M. Belz, J. Shannon, V. Khalilov, M. Klein, C. Jakob, Silica-based UV-fibers for DUV applications: current status, in: Proc. SPIE, 2013: p. 87750B.

[9] R.T. Williams, Vacuum ultraviolet properties of beryllium fluoride glass, J. Appl. Phys. 52 (1981) 6279.

[10] N. Kitamura, J. Hayakawa, H. Yamashita, Optical properties of fluoroaluminate glasses in the UV region, J. Non. Cryst. Solids. 126 (1990) 155–160.

[11] H. Hefang, L. Fengying, Y. Yibo, F. Jitian, Crystallization of fluoroaluminate glasses, J. Non. Cryst. Solids. 112 (1989) 306–308.

[12] U. Bärenwald, M. Dubiel, W. Matz, D. Ehrt, Structural models of the fluoroaluminate glass system $Ba(PO_3)_2$-CaF_2-AlF_3, J. Non. Cryst. Solids. 130 (1991) 171–181.

[13] D. Ehrt, M. Leister, A. Matthai, Polyvalent elements iron, tin and titanium in silicate, phosphate and fluoride glasses and melts, Phys. Chem. Glas. 42 (2001) 231–239.

[14] D. Ehrt, REVIEW: Phosphate and fluoride phosphate optical glasses — properties, structure and applications, Phys. Chem. Glas. Eur. J. Glas. Sci. Technol. Part B. 56 (2015) 217–234.

[15] D. Ehrt, P. Ebeling, U. Natura, UV transmission and radiation-induced defects in phosphate and fluoride-phosphate glasses, J. Non. Cryst. Solids. 263 (2000) 240–250.

[16] D. Möncke, D. Ehrt, L.L. Velli, C.P.E. Varsamis, E.I. Kamitsos, Structure and properties of mixed phosphate and fluoride glasses, Phys. Chem. Glas. J. Glas. Sci. Technol. Part B. 46 (2005) 67–71.

[17] X. Zou, K. Itoh, H. Toratani, Transmission loss characteristics of fluorophosphate optical fibers in the ultraviolet to visible wavelength region, J. Non. Cryst. Solids. 215 (1997) 11–20.

[18] X. Zou, H. Toratani, Radiation resistance of fluorophosphate glasses for high performance optical fiber in the ultraviolet region, J. Appl. Phys. 81 (1997) 3354–3362.

[19] D. Feng, Q. He, M. Lu, W. Li, W. Song, P. Wang, B. Peng, Investigations on the photoluminescence spectra and its defect-related nature for the ultraviolet transmitting fluoride-containing phosphate-based glasses, J. Non. Cryst. Solids. 425 (2015) 130–137.

[20] U. Natura, T. Feurer, D. Ehrt, Kinetics of UV laser radiation defects in high performance glasses, Nucl. Instruments Methods Phys. Res. Sect. B-Beam Interact. with Mater. Atoms. 166 (2000) 470–475.

[21] P. Wang, M. Lu, F. Gao, H. Guo, Y. Xu, C. Hou, Z. Zhou, B. Peng, Luminescence in the fluoride-containing phosphate-based glasses: A possible origin of their high resistance to nanosecond pulse laser-induced damage, Sci. Rep. 5 (2015) 8593.

[22] C. A. G. Kalnins, H. E. Heidepriem, A. Dowler, T.M. Monro, Fabrication of fluoride phosphate glass optical fibres for UV applications, in: Proc. Int. Quantum Electron. Conf. Conf. Lasers Electro-Optics Pacific Rim 2011, Optical Society of America, Sydney (2011) 2051-2053.

[23] C.A.G. Kalnins, N.A. Spooner, T.M. Monro, H. Ebendorff-Heidepriem, E. Bailey, Surface Analysis and Treatment of Extruded Fluoride Phosphate Glass Preforms for Optical Fiber Fabrication, J. Am. Ceram. Soc. 99 (2016) 1874–1877.

[24] M. Boivin, M. El-Amraoui, Y. Ledemi, S. Morency, R. Vallée, Y. Messaddeq, Germanate-tellurite composite fibers with a high-contrast step-index design for nonlinear applications, Opt. Mater. Express. 4 (2014) 1740–1746.

[25] D. Manzani, Y. Ledemi, I. Skripachev, Y. Messaddeq, S.J.L. Ribeiro, R.E.P. De Oliveira, C.J.S. De Matos, Yb^{3+} Tm^{3+} and Ho^{3+} Triply-Doped Tellurite Core-Cladding Optical Fiber for White Light Generation, Opt. Mater. Express. 1 (2011) 1515–1526.

[26] G. Tao, H. Ebendorff-Heidepriem, A.M. Stolyarov, S. Danto, J. V. Badding, Y. Fink, J. Ballato, A.F. Abouraddy, Infrared Fibers, Adv. Opt. Photonics. 7 (2015) 379–458.

[27] H. Tokiwa, Y. Mimura, T. Nakai, O. Shinbori, Fabrication of Long Single-Mode and Multimode Fluoride Glass Fibres by the Double-Crucible Technique, Electronics Letters, 21 (1985) 1131-1132.

[28] P.A. Tick, N.F. Borrelli, I.M. Reaney, Relationship between structure and transparency in glass-ceramic materials, Opt. Mater. (Amst). 15 (2000) 81–91.

[29] A. Galstyan, S.H. Messaddeq, V. Fortin, I. Skripachev, R. Vallée, T. Galstian, Y. Messaddeq, Tm^{3+} doped Ga–As–S chalcogenide glasses and fibers, Opt. Mater. (Amst). 47 (2015) 518–523.

[30] M.F. Churbanov, V.S. Shiryaev, A.A. Pushkin, V.V. Gerasimenko, A.I. Suchkov, V.S. Polyakov, V.V. Koltashev, V.G. Plotnichenko, Origin of microinhomogeneities in As-S-Se glass fibers fabricated by the double-crucible method, Inorg. Mater. 43 (2007) 436–440.

[31] J. Sanghera, I. Aggarwal, L. Busse, P. Pureza, V. Nguyen, R. Miklos, F. Kung, R. Mossadegh, Development of low loss IR transmitting chalcogenide glass fibers, Proc. SPIE 2396, Biomedical Optoelectronic Instrumentation, 2396 (1995) 71–77.

[32] J. Lapointe, Y. Ledemi, S. Loranger, V.L. Iezzi, E.S. de Lima Filho, F. Parent, S. Morency, Y. Messaddeq, R. Kashyap, Fabrication of ultrafast laser written low-loss waveguides in flexible As_2S_3 chalcogenide glass tape, Opt. Lett. 41 (2016) 203–206.

[33] T.S. Gonçalves, R.J. Moreira Silva, M. De Oliveira Junior, C.R. Ferrari, G.Y. Poirier, H. Eckert, A.S.S. De Camargo, Structure-property relations in new fluorophosphate glasses singly- and co-doped with Er^{3+} and Yb^{3+}, Mater. Chem. Phys. 157 (2015) 45–55.

[34] D. Ehrt, Fluoroaluminate glasses for lasers and amplifiers, Curr. Opin. Solid State Mater. Sci. 7 (2003) 135–141.

[35] B. Karmakar, P. Kundu, R.N. Dwivedi, UV transparency and structure of fluorophosphate glasses, Mater. Lett. 57 (2002) 953–958.

[36] D. Ehrt, W. Seeber, Glass for high performance optics and laser technology, J. Non. Cryst. Solids. 129 (1991) 19–30.

[37] D. Ehrt, M. Carl, T. Kittel, M. Müller, W. Seeber, High-performance glass for the deep ultraviolet range, J. Non. Cryst. Solids. 177 (1994) 405–419.

[38] R.K. Brow, Review: the structure of simple phosphate glasses, J. Non. Cryst. Solids. 263 (2000) 1–28.

[39] H. Ebendorff-Heidepriem, T.M. Monro, Extrusion of complex preforms for microstructured optical fibers, Opt. Express. 15 (2007) 15086–15092.

[40] D.C. Tran, G.H. Sigel, B. Bendow, Heavy Metal Fluoride Glasses and Fibers: A Review, J. Light. Technol. 2 (1984) 566–586.

[41] T. Iqbal, M.R. Shahriari, P. Foy, G.H. Sigel, Preliminary study of fiber drawing of AlF_3-based glasses, Mater. Sci. Eng. B. 12 (1992) 299–303.

4. RARE-EARTH DOPED FLUORIDE PHOSPHATE GLASSES: STRUCTURAL FOUNDATIONS OF LUMINESCENCE PROPERTIES

This chapter is based on an article manuscript that discusses the structural foundations of luminescence properties of a serie of FP glasses with diferent fluoride/phosphate ratios. Raman and multinuclear solid-state nuclear magnetic resonance (NMR) spectroscopies were used to study the polyphosphate network transformation. The photoluminescence properties of these glasses doped with Eu^{3+} ion were correlated with their structural transformation.

RÉSUMÉ DE L´ARTICLE INSÉRÉ

Verre fluorophosphate dopées aux terres rares: fondations structurelles des propriétés de luminescence.

Ce travail décrit une étude structurelle détaillée d'une série de verre FP. Les spectroscopies RMN et Raman confirment que la structure du réseau de polyphosphates est transformée successivement en une structure dominée par les liaisons Al-O-P avec l'augmentation du AlF_3. Le nombre moyen de liaisons Al-O-P a été quantifié par des techniques de double résonance $^{27}Al/^{31}P$. La majorité des espèces de fluor sont trouvées dans un environnement riche en alcalino-terreux/aluminium. Les environnements locaux pour les ions de terres rares ont été caractérisés par la spectroscopie EPR des sondes Yb^{3+} et par des photoluminescences sur les ions Eu^{3+}. Les résultats indiquent des corrélations claires entre les propriétés luminescentes en fonction de la composition et confirment que, même au plus haut niveau de fluorure, il existe encore une certaine coordination résiduelle du phosphate avec les terres rares.

RARE-EARTH DOPED FLUORIDE PHOSPHATE GLASSES: STRUCTURAL FOUNDATIONS OF LUMINESCENCE PROPERTIES

Gustavo Galleani, Silvia Helena Santagneli, Younes Messaddeq, Marcos de Oliveira Jr.[3] and Hellmut Eckert

Institute of Chemistry, São Paulo State University/UNESP, Araraquara, Brazil

Center for Optics, Photonics and Lasers, Laval University, Québec-QC, Canada

Instituto de Física de São Carlos, Universidade de São Paulo, São Carlos. Brasil

Institut für Physikalische Chemie, Münster, Germany

ABSTRACT

We report a detailed structural investigation of a series of fluoride phosphate glasses with different phosphate/fluoride ratios in the system $xSr(PO_3)_2$-(100-x)[AlF_3-CaF_2-SrF_2-MgF_2] with x = 5, 10, 20, 40. Raman and multinuclear solid NMR spectroscopies confirm that the polyphosphate network structure is successively transformed to a structure dominated by Al-O-P linkages with increasing AlF_3 content. Average numbers of Al-O-P linkages have been quantified by $^{27}Al/^{31}P$ NMR double-resonance techniques. The majority

56

of the fluoride species are found in an alkaline earth metal/aluminum rich environment. The local environments for rare-earth ions have been characterized by EPR spectroscopy of Yb^{3+} ion spin probes and by photoluminescence experiments on Eu^{3+} dopant ions, including the $^5D_0 \rightarrow ^7F_2$ and $^5D_0 \rightarrow ^7F_1$ transition intensity ratio, the normalized phonon sideband intensities in the excitation spectra, and the lifetime of the $^5D_0$ excited state. The results indicate clear correlations between these parameters as a function of composition, and confirm that even at the highest fluoride levels, there is still some residual rare-earth phosphate coordination.

4.1. INTRODUCTION

A wide range of fluoride-phosphate (FP) glass systems have been produced over time by combining metal fluorides (mainly AlF_3, MF_2, YF_3, NaF), (M = Ba, Ca, Mg, Sr, Zn, Mn) and polyphosphates ($NaPO_3$, $Ba(PO_3)_2$, $Sr(PO_3)_2$, $Al(PO_3)_3$) in molten state syntheses.[1–4] They combine the desirable optical properties of fluoride glasses with the good glass forming ability and fiber drawing stability of phosphate glasses. The resulting fluoride-phosphate glasses have low refractive indices, long-term radiation resistance to UV light and a wide intrinsic transmission range from ~160 to 4000 nm when prepared from high-purity starting materials, as the main limitation is the extrinsic absorption caused by the presence of transition metal impurities in the ppm range.[3,5–7] The phosphate component ensures good glass-forming ability, high chemical durability and the ability to incorporate high concentrations of rare-earth (RE)- ions, whereas high fluorine contents are known to improve rare earth emission efficiency. The first coordination sphere of the rare-earth ions is deemed crucial in determining their emissive properties. The high ionicity of the RE-F bonds creates a rather low phonon energy environment, which suppresses vibrational relaxation processes thereby lengthening excited state lifetimes and quantum yields. Owing to the above mentioned properties, RE-doped FP glasses have great potential for applications in the design of lasers and other high efficiency photonic devices.[4,8–10]

Of special interest is the application of FP glasses in the form of optical fibers, which has been recently explored in the literature.[11–13] Some examples of applications in this field are: (i) a transmission medium of UV light for fast remote elemental analysis, where powerful

laser pulses are used to excite the sample and the optical fiber can be employed to collect and transmit the UV-light emitted from them;[13] (ii) a high performance optical fiber in the ultraviolet region;[6] (iii) optical fiber radiation dosimetry as probes and distributed sensing devices, where FP glasses can be doped with Ce^{3+} and Tb^{3+}, i.e. for detection of radiation by optically stimulated luminescence;[11,14] (iv) telecommunication, where FP glasses can be doped with RE- ions for fiber amplifiers;[8] and (v) Yb^{3+}- doped single-mode fiber lasers for remote sensing technology and astronomy and meteorological observation.[15] Unfortunately, many studies still face some issues in the fabrication process of FP optical glass fibers, such as superficial crystallization[12] or formation of bubbles during the fiber drawing process (commonly observed in the fabrication of fluoride fibers).[13] Concerning these issues, which limit the practical application of FP glass fibers, fundamental structural studies of FP glasses might open new possibilities for the development of optical fibers for the above mentioned applications.

Due to its element selectivity, local selectivity, and inherently quantitative character, solid state NMR is an important method for structural characterization of glasses, as previously illustrated for various different fluoride-phosphate glass systems.[8,16–21] Regarding RE-doped FP glasses, the combination of NMR with pulsed EPR techniques and optical spectroscopy defines a comprehensive integrated spectroscopic strategy to obtain important quantitative information on short and medium range order of the glass network and also on the RE ion coordination environment.[20,21]

In this paper, we report a detailed structural characterization of the well-established fluoride-phosphate glass system $Sr(PO_3)_2$-$(AlF_3$-CaF_2-SrF_2-$MgF_2)$,[4] with systematic variation of the phosphate/fluoride ratio. The compositional complexity arises from the need of mixing the various alkaline earth fluorides in the melt to suppress crystallization. In designing the compositional series selected, we chose to keep the relative ratios of the alkaline earth and aluminum fluoride constant, while varying the $Sr(PO_3)_2$/ total metal fluoride ratio. The ratio of the different metal fluorides was kept constant if at all possible, and only varied if necessary to ensure the formation of glassy materials. The network structure has been studied by comprehensive multinuclear single and double resonance NMR spectroscopy and Raman scattering. In addition, the local environments of the RE ions have

been characterized by pulsed EPR of Yb^{3+} doped glasses. The results are compared with the emission properties and photophysical parameters of Eu^{3+} dopants in these matrices, offering detailed structure/function correlations in these glasses.

4.2. EXPERIMENTAL PROCEDURE

4.2.1. Bulk glass synthesis:

10 g batches of fluoride-phosphate glasses within the composition range $xSr(PO_3)_2$-(100-x)$[AlF_3$-CaF_2-MgF_2-$SrF_2]$, x = 5, 10 20 and 40 mol %, as detailed in Table 1 were prepared by the conventional melt-quenching method from mixed fluorides, AlF_3 (MV labs, 99 %), SrF_2 (Alfa Aesar, 99 %), CaF_2 (Sigma-Aldrich, 99 %), MgF_2 (Sigma-Aldrich, 99.9 %) and strontium metaphosphate ($Sr(PO_3)_2$) glass. The $Sr(PO_3)_2$ glass was prepared from the solid state reaction of $NH_4H_2PO_4$ (J. T. Baker, 99.4 %) and $SrCO_3$ (Riedel – de Haen, 99 %) as shown below:

$$SrCO_{3(s)} + 2(NH_4)H_2PO_{4(s)} \rightarrow Sr(PO_3)_{2(s)} + CO_{2(g)} + 3H_2O_{(g)} + 2NH_{3(g)}$$

The powdered mixture was loaded in a platinum crucible and heated at 250 ºC at a rate of 5 °C·min^{-1} in an electric furnace. The mixture was kept at this temperature during 24 h to allow a complete reaction of the precursors, and was subsequently heated at 500 ºC for 1 h to evaporate the gaseous products formed during the reaction. After the reaction, the fluoride starting materials were mixed with the strontium polyphosphate glass in a capped platinum crucible and melted at 1000 °C in an electric furnace. The resulting liquid was kept at this temperature for 30 min to ensure homogenization and fining. Finally, the melted glasses were cooled rapidly in a brass mold kept at 20 °C below the glass transition temperature. The glass was then placed into a resistive oven at the annealing temperature 20 °C below the Tg value for 4 h and subsequently cooled down to room temperature in approximately 10 h to remove any residual stress induced during the quenching.

Table 1: Sample denomination, batch composition (mol%) and glass transition temperature (T_g) of the investigated glasses.

Glass Acronym	$Sr(PO_3)_2$	AlF_3	CaF_2	MgF_2	SrF_2	[P]/[F]	[P]/[Al]	T_g (°C)
5SrPF	5	38	25	11	21	0.05	0.26	439
10SrPF	10	35	30	10	15	0.10	0.56	451
20SrPF	20	32	21	9	18	0.22	1.22	499
40SrPF	40	24	16	5	15	0.52	3.33	527

Glass samples doped with 0.5 mol % Yb^{3+} and 0.5 mol % Eu^{3+} were prepared in an analogous fashion, for EPR and photophysical studies, respectively, using YbF_3 (Strem Chemicals, 99.9 %) and EuF_3 (Sigma-Aldrich, 99.99 %) The glass samples prepared are labeled as xSrPF_0.5Yb and xSrPF_0.5Eu, respectively, with x = 5, 10, 20 and 40. The effect of the fluorine loss upon the local structure and optical properties was also studied, by preparing a doped glass sample 5SrPF in an environment of excess fluoride, analogous to the refluorination procedure, reported in reference 18. To this end, 1g of NH_4HF_2 was added to the batch and kept at 330 °C for 3h, for removal of oxide impurities and decrease of fluorine losses, before melting-and quenching as described above. The samples were labeled as 5SrPF_0.5Eu_bif and 5SrPF_0.5Yb_bif.

4.2.2. Glass sample characterization:

DSC measurements were conducted with a TA Instruments 2910 calorimeter, using a heating rate of 10 °C min^{-1} and using +/- 25 mg glass pieces within Al pans. Visible photoluminescence excitation (PLE), emission (PL) and excited state lifetime measurements on Eu^{3+}-doped samples were performed in a Fluorolog FL-322 spectrofluorimeter from Horiba Jobin Yvon, equipped with a Hamamatsu photomultiplier for the 250–850 nm range.

Raman scattering measurements were performed at room temperature using a LabRam HR spectrometer, Horiba-Jobin Yvon. The 632 nm line from an argon ion laser was focused on the samples by an optical microscope using a long work distance 50X objective.

4.2.3. Solid state NMR.

Solid State ^{31}P and ^{27}Al NMR studies were carried out on a Bruker Avance III spectrometer operating at 400 MHz, equipped with a 4 mm probe. ^{27}Al MAS NMR spectra were recorded using short pulses of 1 μs length and a relaxation delay of 5 s. Chemical shifts are reported relative to a 1M $Al(NO_3)_3$ aqueous solution. ^{31}P MAS NMR spectra were recorded using π/2 pulses of 3.0 μs length and a relaxation delay of 150 s. In a separate set of measurements, double-quantum filtered spectra were obtained using the 1-D refocused INADEQUATE method.[22] This experiment results in the selective detection of only those ^{31}P nuclei that are involved in a P-O-P linkage ($Q^{(1)}$ and $Q^{(2)}$ units), giving rise to the excitation of a double quantum coherence through indirect [31]P-^{31}P spin-spin coupling. In contrast, the signals of isolated $Q^{(0)}$ units are suppressed by appropriate receiver phase cycling. Experimental conditions were: spinning speed 12.0 kHz, π/2 pulse length 3.0 μs, relaxation delay 150 s. The mixing time for DQ coherence creation was 16.6 ms, corresponding to a value of the indirect coupling constant $^2J(^{31}P-^{31}P)$ of 30 Hz. Chemical shifts were referenced against an external 85% H_3PO_4 standard. $^{27}Al\{^{31}P\}$ rotational echo double resonance (REDOR) measurements were conducted under the same conditions, using π recoupling pulses on the ^{31}P channel and acquisition of rotor-synchronized [27]Al spin echoes (the π pulse length was 6.0 μs in these experiments). The second moments $M_{2(Al-P)}$ characterizing the dipolar interaction between the quadrupolar observation nuclei ([27]Al in the present case) and the neighboring ^{31}P nuclei (I = ½), were obtained by applying a parabolic fit to the REDOR data within the range $S/S_0 \leq 0.2$, corresponding to the expression. [23]

$$\frac{\Delta S}{S_0} = \frac{4}{3\pi^2}(NT_R)^2 M_{2_{AlP}}$$

The experiments were carried out at two MAS frequencies (12.0 and 14.0 kHz) in order to have a considerable number of data points for short dephasing times. No ^{19}F decoupling

was done. From the obtained $M_{2_{AlP}}$ values, an average number of Al− O− P linkages can be estimated by comparison with REDOR data on the crystalline model compound $Al(PO_3)_3$ (six Al-O-P linkages). $^{31}P\{^{27}Al\}$ Rotational Echo Adiabatic Passage Double Resonance (REAPDOR) [24] experiments were carried out using a typical value for ^{31}P π -pulse duration of 5.8 μs and a spinning frequency of 12.0 kHz. A recycle delay of 120 s was applied in combination with a presaturation train of 10 π /2 pulses. To get quantitative information, the $^{31}P\{^{27}Al\}$ REAPDOR dephasing curves were simulated using the SIMPSON program package [25] and these simulations were based on the actual experimental values of the parameters obtained from ^{27}Al MAS-NMR. The dipolar coupling constant was calculated on the basis of the same internuclear distance (327 pm) as found in crystalline $Al(PO_3)_3$, and both $^{31}P-^{27}Al$ two-spin and $^{31}P(^{27}Al)_2$ three spin systems were calculated. For all the nuclei detected, spin− lattice relaxation times were measured using the saturation recovery sequence. Line shape analysis and deconvolutions were done using the DMFIT routine.[26] ^{19}F MAS NMR as well as $^{27}Al\{^{19}F\}$ and $^{19}F\{^{31}P\}$ REDOR experiments were performed on an Agilent DD2 spectrometer operating at 5.7 T. $^{27}Al\{^{19}F\}$ REDOR experiments were performed in a 4 mm probe which was operated at spinning rates up to 14.0 kHz using the standard Schaefer-Gullion sequence[29] (without compensation), with π recoupling pulses on the ^{19}F channel and acquisition of rotor-synchronized ^{27}Al spin echoes. ^{19}F MAS NMR spectra were recorded in 1.6 mm rotors spinning at 35.0 kHz, using a rotor-synchronized Hahn-Echo sequence with 4 to 8 rotor cycles for the echo formation in order to remove the probe background signal. Different evolution times were tested and the values used in the experiments do not influence the relative intensities of the resolved spectral components, indicating similar spin-spin relaxation times. 90° pulses of 1.65 μs length and relaxation delays of 20 s were used. Chemical shifts are reported relative to $CFCl_3$ using solid AlF_3 as a secondary reference (−172 ppm).[28] $^{19}F\{^{31}P\}$ REDOR measurements were carried out in a 3.2 mm probe operated at a spinning frequency of 25.0 kHz, using the compensation method[28] with π recoupling pulses on the ^{31}P channel and acquisition of rotor-synchronized ^{19}F spin echoes. In these experiments the π pulse length was 4.0 μs for both isotopes.

4.2.4. Solid state EPR:

Pulsed solid-state EPR experiments were performed on Yb-doped samples at 6 K on an E-580 BRUKER ELEXSYS X-band EPR spectrometer. The electronic configuration of an Yb^{3+} ion is [Xe] $4f^{13}$. Thus, one electron in the 4f shell is unpaired and therefore Yb^{3+} is a KRAMER ion with S = 1/2. The 4f configuration gives rise to a $^2F_{7/2}$ term in the ground state and a $^2F_{5/2}$ term in the first excited state (energy difference 10 000 cm^{-1} for the free Yb^{3+} ion). The $^2F_{5/2}$ term has little effect on the magnetic properties. Owing to the low dopant concentrations used (0.1 to 0.5 mole%) inter-electronic dipole interactions can be neglected.

Electron spin echo envelope modulation (ESEEM) spectra were obtained at external field strengths of 550 and 700 mT using the three-pulse sequence (t_p) - τ - (t_p) - T - (t_p) – echo,[29–31] with a $\pi/2$ pulse length t_p = 8 ns. Different τ values were tested to examine the possible occurrence of blind spots. Spectra measured for τ = 100 ns, 120 ns, 140 ns were co-added to give a blind-spot-free spectrum. The time interval T was incremented in 12-ns steps starting with T = 300 ns; 300 acquisitions were accumulated for each increment with repetition times of 300 μs and up to 20 scans were added up for signal averaging. A four-step phase cycle of the first and second pulse was used for echo detection to avoid unwanted primary echoes and FID distortions.[29] The resulting data were processed in the following way: the modulated echo decay was fitted to a biexponential function, which in turn is subtracted from the experimental data in order to isolate the oscillatory component. Following further apodization and zero-filling, the oscillating signal was Fourier-transformed, resulting in the ESEEM spectrum. The echo detected absorption spectra were recorded using the three-pulse stimulated echo sequence. The integrated echo intensities were measured as a function of the magnetic field strength over the range 10 – 1000 mT. The pulse spacing between the first two pulses (τ) was set to 100 ns, and for the time between the second and the third pulse (T) a value of 10 μs was chosen in order to suppress nuclear frequency modulation effects. The Fourier-transformed spectra showed no dependence on T within the data range 8-15 μs. Hyperfine sublevel correlation (HYSCORE) experiments were conducted at an external magnetic field strength of 500 mT using the four-pulse sequence (t_p) - τ - (t_p) - t_1 - $(2t_p)$ - t_2 - (t_p) – echo,[29,31] with τ = 80 ns. The echo intensity was measured as a function of t_1 and t_2, which were incremented in steps of 16 ns from the initial values of 300 ns. Pulses

of $t_p = 8$ ns length for the $\pi/2$ pulse and $2t_p = 16$ ns length for the π pulse were used to record a matrix of 160×160 data points. Following further apodization and zero-filling (to 512×512 points), the oscillating signal was Fourier-transformed in both dimensions, resulting in the HYSCORE spectrum. A 4-step phase cycle was used to eliminate unwanted echoes.

4.3.   RESULTS, DATA ANALYSIS AND INTERPRETATION

4.3.1. Glass Properties.

The glasses obtained after melting were visually transparent, homogeneous and chemically stable. Table 1 summarizes the glass batch compositions and their glass transition temperatures, T_g. T_g increases from 439 °C for 5SrPF to 522 °C for 40SrPF with increasing $Sr(PO_3)_2$ content, suggesting a strengthening of the covalent network. It is known from previous quantitative NMR work on related fluoride phosphate glasses,[20] that under the preparation conditions applied, substantial fluoride loss is encountered (about 20 % of the batch) via F/O exchange between melt and the surrounding furnace atmosphere. However, the qualitative conclusions from the NMR work reported in the present study are not affected by this exchange reaction.

4.3.2. Raman Spectroscopy.

Preliminary structural studies of fluoride-phosphate glasses based on $Sr(PO_3)_2$ and fluorides (CaF_2, MgF_2, SrF_2 and AlF_3) by Raman and solid state NMR spectroscopy have been previously reported.[16,19,32] The Raman spectra of our xSrPF (x = 5, 10, 20, 40) glasses (Fig. 4-1) are in good agreement with these earlier results. For the sample richest in fluoride (5SrPF), we observe two strong bands at 1075 and 1000 cm^{-1} which are assigned to the symmetric P-O stretching modes in $Q^{(1)}$ and $Q^{(0)}$ units, respectively. The band near 750 to 770 cm^{-1} is assigned to the P-O-P symmetric stretching mode of bridging oxygens between two phosphate tetrahedra, such as $Q^{(1)}$ species and the band at 550 cm^{-1} can be assigned to

64

the stretching vibration of $Al(F,O)_6$ polyhedra mostly in an octahedral coordination. Finally, the broad band around 300-400 cm^{-1} is attributed to the bending modes of phosphate units. The intensity of the band characteristic of the $Q^{(0)}$ units increases with an increase of the fluoride content. Consistent with this observation, the intensities of the bands near 760 cm^{-1} and 350 cm^{-1} decrease as the $Q^{(1)}$ contribution diminishes. In the sample richest in $Sr(PO_3)_2$ (40SrPF) the P-O-P stretching mode is observed at somewhat lower wave numbers (750 cm^{-1} compared to 770 cm^{-1}), suggesting an additional contribution from $Q^{(2)}$ units. The Raman data give no evidence of phosphorus-fluorine bonds, which would be expected to exhibit a band near 850 cm^{-1}.[16]
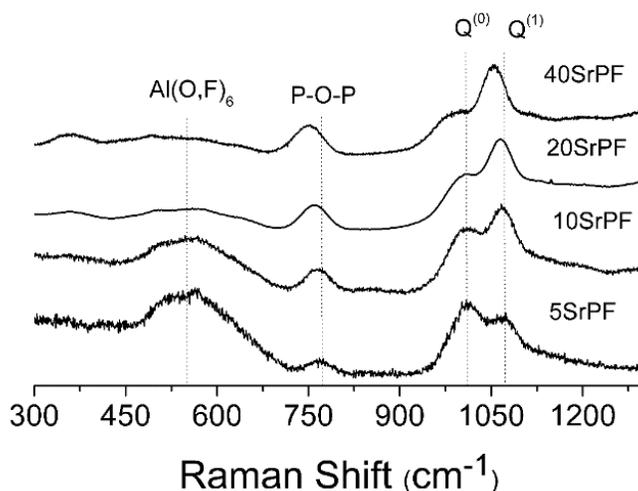
Figure 4-1. Raman spectra of the fluoride-phosphate glasses.

4.3.3. Solid state NMR.

4.3.3.1.   Single-pulse NMR.

The ^{31}P MAS NMR spectra of the glass samples (Fig. 4-2a) present a broad and asymmetric lineshape near -10 ppm, suggesting multiple contributions of $Q^{(n)}$ phosphate units. Based on previous NMR studies of alkali aluminophosphate glasses at least nine different phosphorus sites can be expected, depending on the number of P and Al next nearest

neighbors, namely $Q^{(2)}_{0Al}$, $Q^{(2)}_{1Al}$, $Q^{(1)}_{0Al}$, $Q^{(1)}_{1Al}$, $Q^{(1)}_{2Al}$, $Q^{(0)}_{0Al}$, $Q^{(0)}_{1Al}$, $Q^{(0)}_{2Al}$, and $Q^{(0)}_{3Al}$ species.[33] Unfortunately, the chemical shift ranges of these units are partially overlapping and thus the individual contributions of these units are difficult to sort out without further fitting constraints. To accomplish at least a partial deconvolution, we have conducted double-quantum filtering (refocused INADEQUATE) experiments (Fig. 4-2b). This experiment is based on the creation of double quantum coherences based on indirect ^{31}P-^{31}P spin spin coupling. Signals from $Q^{(0)}$ species, which lack P-O-P connectivity (and hence spin-spin coupling) are being suppressed in such experiments. This can be used to develop some constraints for their lineshape parameters chemical shift and linewidth. In contrast, the amplitudes of the Refocused INADEQUATE spectra cannot be used as fitting constraints as they are influenced by DQ excitation efficiencies and relaxation phenomena, and thus cannot be compared to the amplitudes of the single-pulse spectra. In the present case, based on this constraint only a simplified fitting model differentiating between $Q^{(0)}$, $Q^{(1)}$, and $Q^{(2)}$ units is possible (see Table 2) While the glass 40SrPF presents both $Q^{(2)}$ and $Q^{(1)}$ connectivity, in the 20SrPF sample the $Q^{(1)}$ units appear to be dominant. Finally, for the glass compositions 5SrPF and 10SrPF the INADEQUATE spectra document the dominance of $Q^{(0)}$ species and the (near-) absence of P-O-P connectivity. The chemical shift distribution obtained in this material must arise from various $Q^{(0)}_{mAl}$ environments. Our results are entirely consistent with our previous conclusions for related fluoride phosphate glass compositions.[8,20,21]
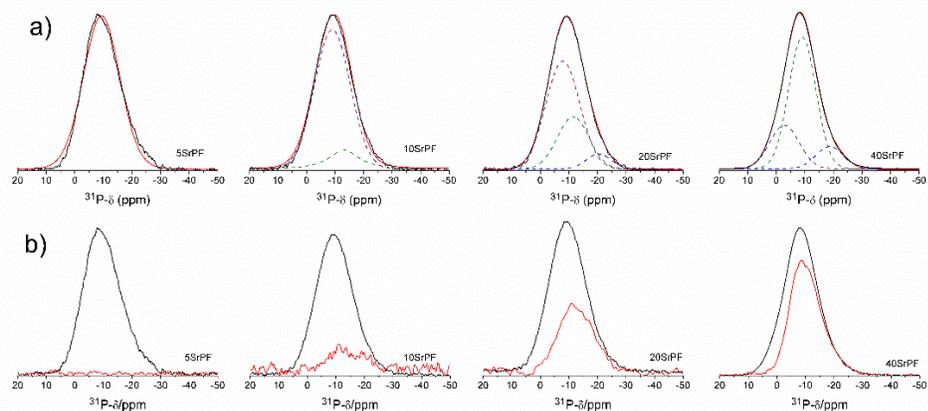
Figure 4-2. (a) Experimental single-pulse ^{31}P MAS NMR spectra and deconvolution model (b) Refocused INADEQUATE (red traces) and single pulse ^{31}P MAS NMR spectra (black

traces) of the investigated fluoride-phosphate glasses. Amplitudes of the black and red traces are chosen arbitrarily, and cannot be compared to each other.

Table 4.2. ^{31}P isotropic chemical shifts (±0.2 ppm) and relative area percentages (±1 %) of the individual Q$^{(n)}$ phosphate species, obtained from the deconvolution of the single pulse ^{31}P MAS NMR spectra of Figure 4-2, and ^{27}Al isotropic chemical shift ∂_{iso}^{CS} and second-order quadrupolar effects *SOQE* determined from fits of the ^{27}Al MAS NMR lineshape to the Czjzek model

Sample	Q$^{(0)}$		Q$^{(1)}$		Q$^{(2)}$		SOQE (MHz)	∂_{iso} (^{27}Al) (ppm)
	∂_{iso} (ppm)	Area (%)	∂_{iso} (ppm)	Area (%)	∂_{iso} (ppm)	Area (%)		
5SrPF	-9.3	100	-	-	-	-	4.1	-2.8
10SrPF	-9.1	76	-13.1	24	-	-	3.9	-1.5
20SrPF	-8.0	63	-11.5	29	-20.4	10	4.1	-1.3
40SrPF	-2.9	21	-9.1	67	-18.8	12	3.9	-1.5

The ^{27}Al MAS NMR spectra the studied glass samples are shown in Fig. 4-3. A dominant resonance near -10 ppm is observed for all the glass compositions, characteristic of six-coordinated aluminum environments. Only a small amount of five-fold coordinated aluminum, near 10 ppm is observed for the sample with highest phosphate content (40SrPF). Additional triple-quantum MAS NMR spectra were measured (data not shown) and the isotropic chemical shift ($\Delta\delta_{iso}^{cs}$) are similar to those obtained by MAS peak fitting (see Table 2). The δ_{iso}^{cs} values obtained in these glasses gradually shift towards higher frequencies with an increase in F/P ratio, suggesting that the coordination sphere of the six-coordinated Al species is made up by a mixture of fluoride and phosphate ions, whose ratio increases systematically with increasing F/P ratio of the glass composition.[34] Table 2 further lists the second-order quadrupolar effect (SOQE) values, defined by $SOQE = [C_Q^2(1+ {}^2/3)]^{1/2}$ [35] extracted from the TQMAS data.
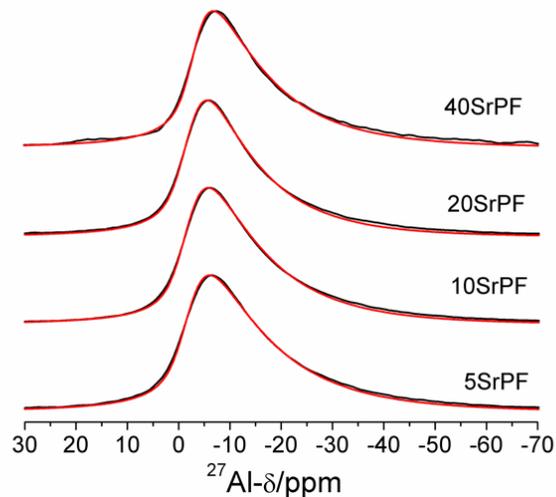
Figure 4-3. ^{27}Al MAS NMR spectra of the investigated fluoride-phosphate glasses (black curves). Red curves represent simulations of the data using the Czjzek model.

Fig. 4-4 shows the ^{19}F MAS NMR spectra. Three resonance lines are observed near -90, -130 and -160 ppm, respectively. The dominant resonance line near -130 ppm can be assigned to fluorine atoms in an alkaline earth metal/aluminum rich environment such as $SrAlF_5$/$CaAlF_5$/$MgAlF_5$, observed in several fluoride-phosphate[16,18,36] and fluoride glass systems.[28,37] The resonance line near -162 ppm can be assigned to Al-bound fluoride species, based on the chemical shift value at -172 ppm[38] in crystalline AlF_3 and on [19]F{[27]Al} REAPDOR results from Ref. 20. The component near -90 ppm suggests an alkaline-earth rich fluoride environment, based on NMR data on crystalline CaF_2 and SrF_2 and of glasses containing larger quantities of the latter.[28,37] No evidence of direct P-F bonding was observed, whose resonance line would be expected near -70 ppm.[16] This is further confirmed by [19]F{[31]P} REDOR results shown below.
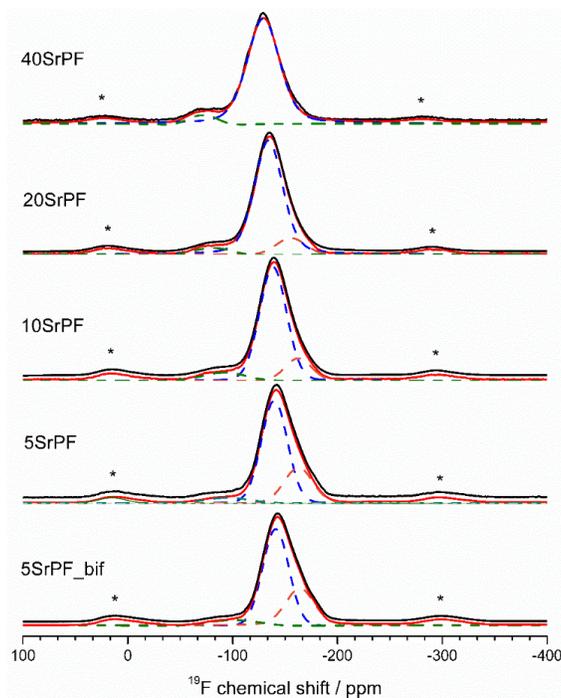
Figure 4-4. ^{19}F-MAS NMR spectra of the investigated fluoride-phosphate glasses. Dashed colored curves denote the deconvolutions into individual Gaussian components. Black curves denote experimental data. Spinning sidebands are marked with asterisks.

4.3.3.2. ^{31}P{^{27}Al} REAPDOR and ^{19}F{^{31}P} and ^{27}Al{^{31}P} REDOR.

One of the principal challenges involving the structures of vitreous materials is to address the connectivity of the different polyhedra that are present in the glasses. This can be done, in a quantitative manner, on the basis of heteronuclear magnetic dipole-dipole couplings, measured via double resonance experiments such as REDOR and REAPDOR. In the present work ^{31}P{^{27}Al} REAPDOR and ^{19}F{^{31}P} and ^{27}Al{^{31}P} REDOR experiments were carried out in order to obtain information about the F-P, Al-P and P-Al connectivities.

Fig. 4-5 shows the ^{19}F{^{31}P} REDOR curves for the fluorine NMR signal components at -95 ppm and at -135 ppm. The second moment of the dipolar coupling $M_{2(F-P)}$ was obtained by parabolic fitting using equation 1. The values are summarized in Table 3. The dipolar second moment for the Sr/Al rich environment (-135 ppm) is 4.7×10^6 rad^{2}s^{-2} for the 5SrPF sample and increases for the samples with increasing phosphate content, up to 23.9×10^6 rad^{2}s$^-$

[2] for the 40SrPF sample. For the resonance line at -95 ppm the second moments increase from 7.4×10^6 rad^2.s^{-2} for the 5SrPF sample to 32.6×10^6 rad^2.s^{-2} for the 40SrPF sample. These results show that the P species are not directly coordinated to F but clearly occur in the second and third coordination sphere of the ^{19}F nuclei. Direct P-F bonding would result in a much stronger dephasing characterized by a $M_{2(F-P)}$ value on the order of 10×10^8 rad^{2}s^{-2}, as obtained by van Vleck calculations[39] for crystalline Na$_2$PO$_3$F.[40] The absence of P-F bonding demonstrated by the ^{19}F{^{31}P} REDOR data is consistent with the ^{19}F chemical shift and Raman data discussed above.
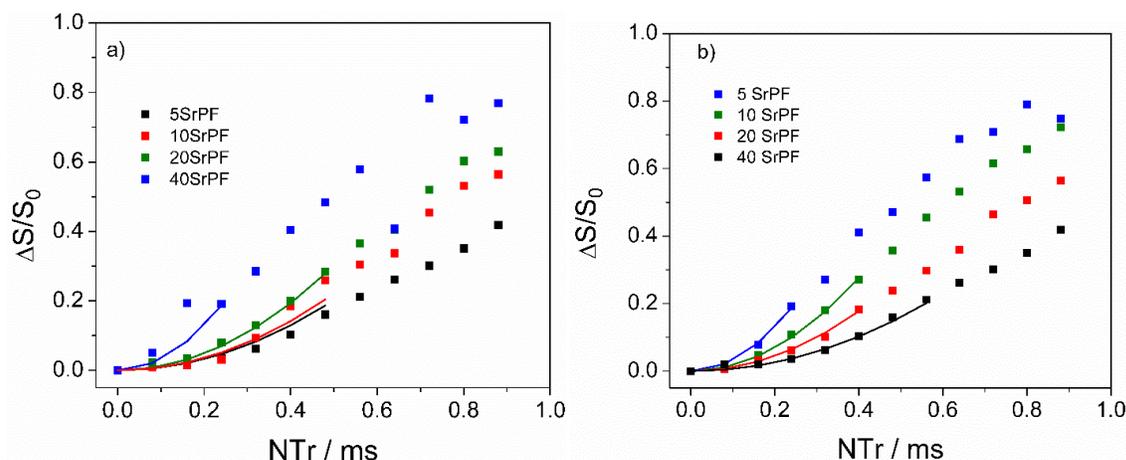
Figure 4-5. ^{19}F{^{31}P} REDOR results for the glasses under study. a) REDOR curves for the -95 ppm and b) Redor curves for the -135 ppm resonances (right). Solid curves show parabolic fits to the initial data range $\Delta S/S_0 \leq 0.2$. Squares represent experimental points.

Table 4.3. ^{19}F-MAS NMR spectral deconvolution parameters isotropic chemical shifts (± 0.5 ppm) and area contributions ($\pm 1\%$) and second moment $M_{2(F-P)}$ ($\pm 10\%$) measured by ^{19}F{^{31}P} REDOR on the investigated fluoride-phosphate glasses .

Sample	Sr/Al-F			Al-F			Sr-F		
	∂_{iso} (ppm)	Area (%)	$M_{2(F-P)}$ (x10^{6}rad^{2}s^{-2})	∂_{iso} (ppm)	Area (%)	$M_{2(F-P)}$ (x10^{6}rad^{2}s^{-2})	∂_{iso} (ppm)	Area (%)	$M_{2(F-P)}$ (x10^{6}rad^{2}s^{-2})
5SrPF_bif.	-141.1	64	-	-164.2	31	-	-101.6	5	-
5SrPF	-139.8	68	4.7	-162.7	26	3.3	-94.9	6	7.4
10SrPF	-138.5	77	8.2	-162.6	15	-	-91.9	8	7.2
20SrPF	-134.3	84	12.7	-155.6	11	-	-81.2	4	8.9
40SrPF	-129.3	96	23.9	-	-	-	-70.9	3	32.6

Fig. 4-6 shows the $^{27}Al\{^{31}P\}$ REDOR data. The $M_{2(Al-P)}$ values obtained from parabolic fits to eq. 1. are summarized in Table 4. As expected, the ^{27}Al-^{31}P magnetic dipole-dipole coupling strengths increase with increasing $Sr(PO_3)_2$ content, and are comparable to those obtained for other fluoride-phosphate glass systems,[8,20,21] By comparison of these $M_{2(Al-P)}$ values with the one measured in $Al(PO_3)_3$ (6 Al-O-P linkages at a distance of 327 pm) we can estimate the average number of P atoms in the second coordination sphere of Al in the glasses, N_P, using the formula $N_P = 6 \times M_{2(Al-P)}(exp)/M_{2(Al-P)}(AlPO_3)_3)$. The results, summarized in Table 4, illustrate that the average number of P atoms linked to Al increases with increasing phosphate content. Based on the ^{27}Al MAS NMR result that all of the Al species are six-coordinated in the present glasses, the average number of F atoms coordinated to Al is given by $N_F = 6 - N_P$ (see Table 4).
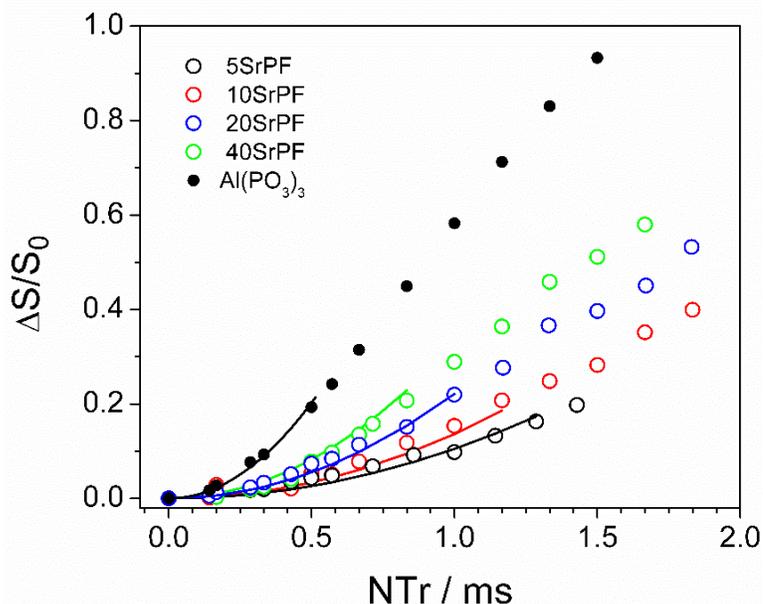
Figure 4-6. $^{27}Al\{^{31}P\}$ REDOR dephasing curves for the set of fluoride-phosphate samples. Circles represent experimental points obtained under MAS spinning speeds of 14.0 and 12.0 kHz. Solid curves are parabolic fits to the data, analyzed within the data range of $\Delta S/S_0 \leq 0.2$.

Table 4. Values of second moments $M_{2(Al-P)}$ ($\pm$10%) obtained from ^{27}Al$\{^{31}$P$\}$ REDOR experiments and connectivity data on glasses. N_P and (N_P/N_F) are respectively the number of P atoms and the fraction of P to F atoms in the Al coordination environment, obtained experimentally from REDOR results. N_{P-O-Al} (REDOR) is the total number of P-O-Al linkages obtained from the ^{27}Al$\{^{31}$P$\}$ REDOR experiments and N_{P-O-Al} (REAPDOR) is the total number of P-O-Al linkages obtained from the ^{31}P$\{^{27}$Al$\}$ REAPDOR experiments.

Sample	$M_{2(Al-P)}$ (x10^{6}rad^{2}s^{-2})	N_P	(N_P/N_F)$_{exp}$	N_{P-O-Al} (REDOR)	N_{P-O-Al} (REAPDOR)
5SrPF	0.77	0.8	0.15	30	20
10SrPF	1.01	1.0	0.20	37	40
20SrPF	1.64	1.7	0.40	54	52
40SrPF	2.4	2.5	0.71	60	80
Al(PO$_3$)$_3$	5.8	6	-	-	-

To estimate the average number of Al atoms in the P coordination environment we further carried out ^{31}P$\{^{27}$Al$\}$ REAPDOR experiments. Fig. 4-7 compares the experimental data with simulations considering spin-systems involving ^{31}P and one or two neighboring ^{27}Al nuclei, assuming the P-Al average distance observed in the crystalline Al(PO$_3$)$_3$ compound (327 pm) and an Al-P-Al angle of 109.4°, which is based on the O-P-O angle in the phosphorus tetrahedron. The average number of P-O-Al linkages per phosphate unit is close to 2.0 for glass with low phosphate concentration (5SrPF and 10SrPF), 1.3 for composition 20SrPF and 1.0 for composition 40SrPF. Finally, the REAPDOR data show no clear correlation between the ^{31}P-^{27}Al dipolar coupling strength and the ^{31}P chemical shift. Based on this finding, we conclude that the average numbers of P-O-Al linkages of the various Q$^{(n)}$ phosphate species are comparable to each other for a given glass composition.
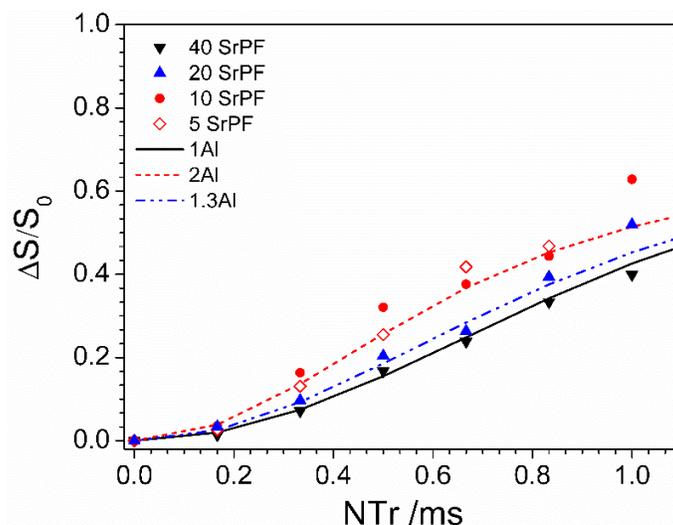
Figure 4-7. $^{31}P\{^{27}Al\}$ REAPDOR dephasing curves of the investigated for fluoride-phosphate glasses. The curves represent SIMPSON simulations of the REAPDOR curves for ^{31}P interacting with 1 (solid black curve), 1.3 (dashed blue curve) or 2 (dashed red curve) ^{27}Al neighbors at a distance of 3.27 Å.

The $^{31}P\{^{27}Al\}$ REAPDOR results show an increase in the average number of P-O-Al linkages for each P unit for decreasing P content. This behavior is expected in view of the decreasing extent of P-O-P linking noted in the ^{31}P MAS NMR and the Raman data. The main $Q^{(n)}$ depolymerization mechanism caused by the interaction of $Sr(PO_3)_2$ with AlF_3 in the melt is the breakage of the P-O-P connectivity with the concomitant formation of P-O-Al linkages. While this process is expected to also produce P-F linkages, the latter are not stable in this temperature range and are likely to be replaced by P-O- linkages, resulting in some fluorine losses via O/F exchange (typically about 20 %) as previously documented for other fluoride phosphate glass compositions.[20]

4.3.4. Photophysical characterization on Eu^{3+} fluoride-phosphate glass samples.

Fig. 4-8 shows the emission spectra obtained for the samples with different phosphate content doped with 0.5 mol % of Eu^{3+}. The excitation wavelength used was 464 nm, which

corresponds to the $^7F_0 \rightarrow {}^5D_2$ transition. All the emissions observed are assigned to the intraconfigurational f-f transitions of Eu^{3+} originating from the $^5D_0 \rightarrow {}^7F_J$ levels ($J = 0, 1, 2, 3$ and 4). The most intense emission around 620 nm is attributed to the hypersensitive electric dipole transition ($^5D_0 \rightarrow {}^7F_2$). This emission is strongly influenced by the chemical environment of Eu^{3+} ions in the host network. On the other hand, the $^5D_0 \rightarrow {}^7F_1$ transition occurs via the magnetic dipole mechanism and its intensity is not sensitive to the chemical environment of the Eu^{3+}. Therefore, in order to highlight the spectroscopic changes the spectra are internally normalized to the peak intensity at 595 nm ($^5D_0 \rightarrow {}^7F_1$). Table 5 lists the emission intensity ratio, $\alpha = I(^5D_0 \rightarrow {}^7F_2)/I(^5D_0 \rightarrow {}^7F_1)$ of these two transitions. The values are in the range for those reported in the literature, near 1.0 for glasses rich in fluoride and near 3.0 for pure phosphate glass,[41–45] and vary systematically with the fluoride/phosphate ratio of the glasses, as previously observed in related systems.[20,21] On the basis of combined NMR and EPR data we previously suggested that α reflects the average quantitative local ligand distribution (phosphate versus fluoride) of the Eu^{3+} ions in these glasses. Phosphate ligation produces higher bond covalency compared to fluoride ligation, resulting in a higher emission cross-section.
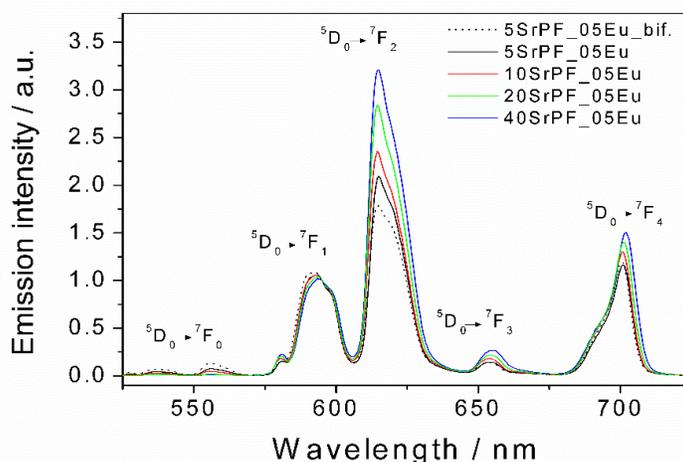
Figure 4-8. Visible emission spectra obtained of the 0.5 mol % Eu^{3+} containing fluoride-phosphate glass samples. The spectra are internally normalized to the peak intensity at 595 nm ($^5D_0 \rightarrow {}^7F_1$). The label 5SrF_05Eu_bif indicates the sample prepared with excess NH_4HF_2 present in the melt.

Table 5. Photophysical data obtained on the fluoride-phosphate glasses under study containing 0.5 mole % Eu. α is the intensity ratio of the emissions at 612 and 595 nm ($^5D_0\rightarrow{}^7F_2$ and $^5D_0\rightarrow{}^7F_1$), τ is the average excited state $^5D_0$ lifetime value. I (441 nm) denotes the phonon sideband intensity normalized to the dominant excitation peak intensity at 464 nm and CG denotes the center of gravity of the EPR line determined over the magnetic field region 1-10 kG (10 – 100 mT).

Sample	α (615/595 nm)	τ (ms)	I (441 nm)x10^{-3}	CG (kG)
5SrPF_0.5Eu_b*	1.78	4.78	4.0	7.38
5SrPF_0.5Eu	2.09	4.19	5.5	7.23
10SrPF_0.5Eu	2.33	3.71	7.9	7.42
20SrPF_0.5Eu	2.82	3.00	10.7	7.01
40SrPF_0.5Eu	3.21	2.21	14.4	6.10

*sample prepared with excess NH_4HF_2 present in the melt

Another parameter that is influenced by the chemical environment of Eu^{3+} is the phonon sideband peak at 441 nm associated with the electric-dipole allowed $^5D_0\rightarrow{}^7F_2$ transition and the most intense excitation line at 463 nm (inset of Fig. 4-9) in the excitation spectra of the monitored $^5D_0\rightarrow{}^7F_2$ emission at 611 nm (Fig. 4-9). This weak phonon side band reflects the vibrational wavenumber 1100 cm^{-1} which is attributed to the $Q^{(1)}$ species in the glasses. The decrease of the phonon sideband intensity with decreasing phosphate content is well correlated with the parallel decrease of $Q^{(1)}$ species concentration observed in both the Raman scattering and the ^{31}P solid state NMR spectra. For aluminum fluoride based glass reported in the literature, phonon sidebands were not observed.[46]
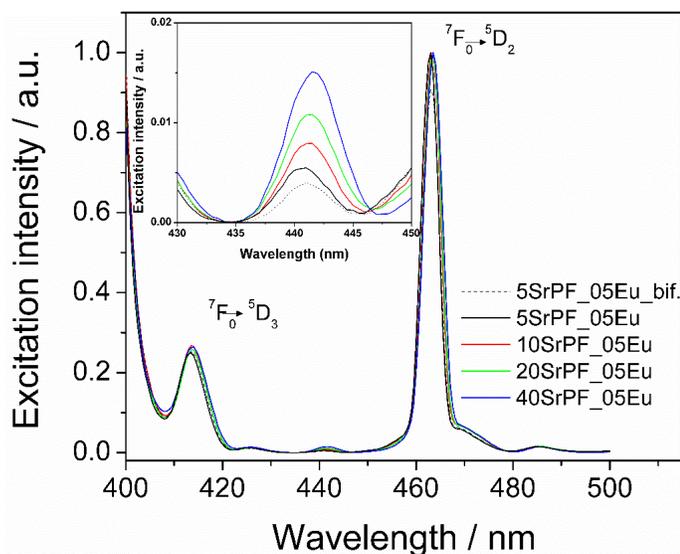
Figure 4-9. Photoluminescence excitation (PLE) spectra by monitoring the $^7F_2 \rightarrow ^5D_0$ transition at 611 nm. The inset shows the internally normalized phonon sideband transition at around 441 nm. The label 5SrF_05Eu_bif indicates the sample prepared with excess NH_4HF_2 present in the melt.

Fig. 4-10 shows mono-exponential emission decay curves for the Eu^{3+}: $^5D_0 \rightarrow ^7F_2$ (611nm) transition excited at 464 nm, corresponding to the excited-state lifetimes listed in Table 5. In agreement with literature data on related systems, the lifetimes strongly increase with decreasing phosphate content, indicating a diminution of vibrational de-excitation. For Eu^{3+} containing fluoride glass matrices, values up to 6.8 ms have been reported, while for phosphate glass matrices, lifetimes are within the range 2.0-2.5 ms.[41,43] The results obtained in the present study are similar to those reported for other fluoride-phosphate systems[42,43] and are in agreement with results reported for this glass system with 3, 10, 20 and 100 mol % phosphate.[10]

76
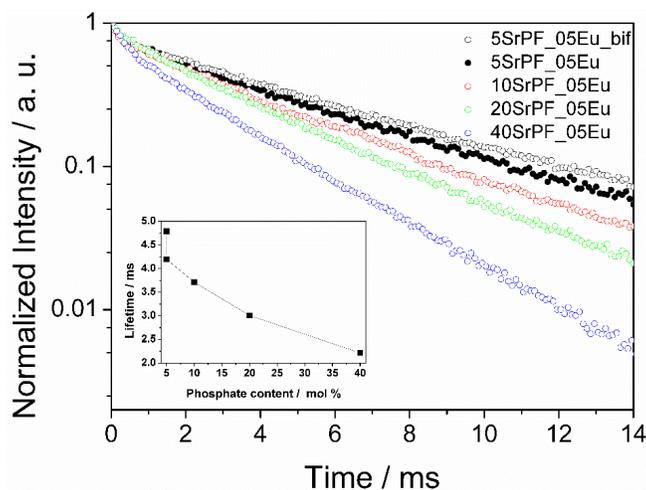
Figure 4-10. Decay curves obtained obtained for 0.5 mol % Eu^{3+} containing fluoride-phosphate glass samples for the $^5D_0 \rightarrow {}^7F_2$ (λ_{exc} = 464 nm) of Eu^{3+} dopants. The label 5SrF_05Eu_bif indicates the sample prepared with excess NH$_4$HF$_2$ present in the melt.

Finally, Figures 4-8 and 4-9 document the improved photophysical properties of glasses prepared in an environment of excess fluoride, leading to lower   -values and phonon sideband intensities as well as to higher excited state lifetimes. The ammonium bifluoride process has been shown to be effective in the production of higher quality fluoride glasses, by partly eliminating oxidic contaminations in the batch.[47]

4.3.5. Pulsed EPR Spectroscopy on Yb^{3+}-doped fluoride-phosphate glass samples.

Fig. 4-11 shows the echo detected field sweep (EDFS) EPR spectra for the set of Yb-doped glasses. No electron spin echo is detected at zero field, consistent with the absence of rare-earth clustering.[48] The observed lineshapes are similar to those previously obtained by us for different oxyfluoride glass systems.[20,21,49] The EDFS lineshapes show variations as a function of the fluoride content of these glasses, Fig. 4-11 shows a systematic displacement of the EDFS signal to higher magnetic fields with increasing fluoride content. The average spectral position (determined as the center of gravity of the EDFS spectra over the magnetic field range investigated) can be used as a quantitative measure of the observed spectroscopic variations. Fig. 4-12a shows the center of gravity of the EDFS spectra (the center of gravity

was taken considering the magnetic field region 10 mT to 1 T in order to ensure a fair comparison with previously measured data[20,21]) as a function of the phosphate/fluoride ratio in the glasses. Overall we observe a very good agreement for all the studied fluoride phosphate glass systems studied so far. Therefore, we attribute the changes observed in our EPR spectra to a systematic change of the oxide to fluoride ligand ratio around the Yb^{3+} ion.
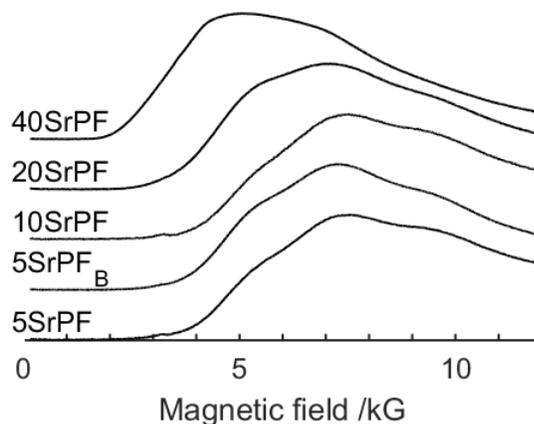
Figure 4-11. Echo-detected field-sweep (EDFS) EPR spectra for Yb-doped glasses (The label $5SrPF_B$ represents the sample prepared with excess NH_4HF_2 present in the melt).

Fig. 4-12b shows a 3D-plot of the center of gravity (*CG*) of the Yb^{3+} EDFS EPR spectra as a function of the α ratio and the excited-state lifetimes τ for the present glasses and for the previously published fluoride phosphate glasses.[20,21] This plot shows an excellent correlation between the two optical parameters, α and τ, which is expected, since both parameters are sensitive to the Eu^{3+} coordination environment (e.g. the phosphate/fluoride ratio). As observed for the previously studied glasses, a good correlation is also observed between *CG* and the optical parameters for the glasses studied in the present work. The good correlation observed in Fig.-12 for the different glass systems indicates that there is no preferential coordination for the rare-earth ions despite the differences in the glass composition.
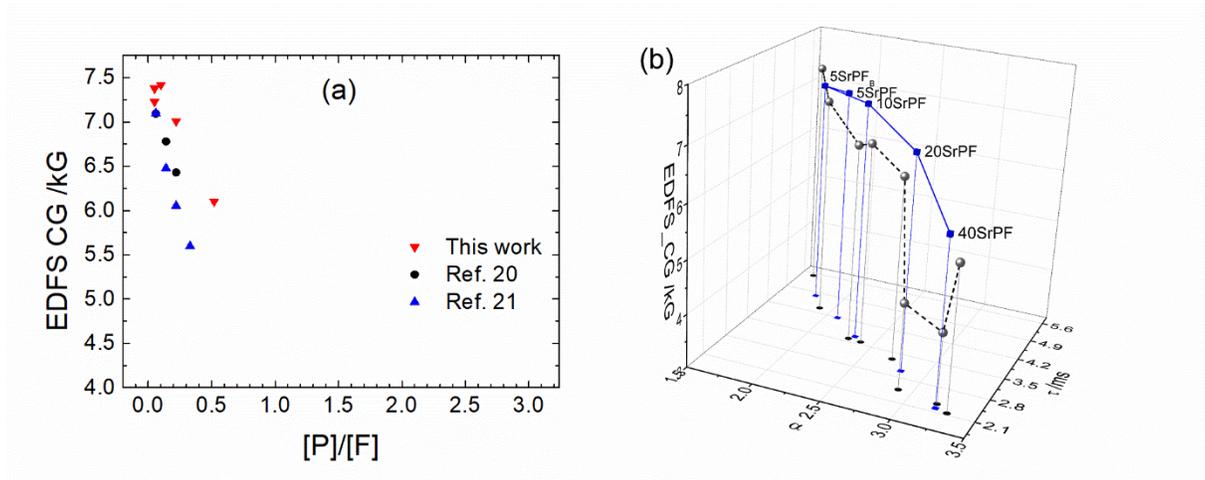
Figure 4-12. Center of gravity of the EDFS spectra taken in the magnetic field region 0.1 – 10 kG, for the glasses studied in the present work and for fluoride-phosphate glasses reported in the literature,[20,21] as a function of the P/F molar ratio (a) and as a function of the photophysical parameters α and τ. The code 5SrPF$_B$ denotes the sample melted in the presence of excess ammonium bifluoride.

Fig. 4-13 shows ESEEM spectra obtained at 700 mT for the set of Yb-doped glasses. It is well known that the three-pulse ESEEM spectra suffer from blind-spots at nuclear frequencies with a period of $1/\tau$, where τ is the first delay in the three-pulse sequence.[29] Because of this, each spectrum shown in Figure 4-13 is obtained from the co-addition of ESEEM spectra measured with different τ delays resulting in blind-spot free spectra. Clearly, the set of spectra reveal the Larmor frequencies of ^{27}Al (7.8 MHz), ^{31}P (12.0 MHz) and ^{19}F (28 MHz), suggesting that all three types of nuclei are interacting with the electron spins residing in the 4f orbitals of the Yb^{3+} ions. The indicated resonances lie in the weak-coupling limit, indicating that the hyperfine coupling constants (in Hz) are small compared to the nuclear Zeeman frequencies. Therefore, we conclude that these signals belong to nuclei in the second or higher order Yb^{3+} coordination spheres.
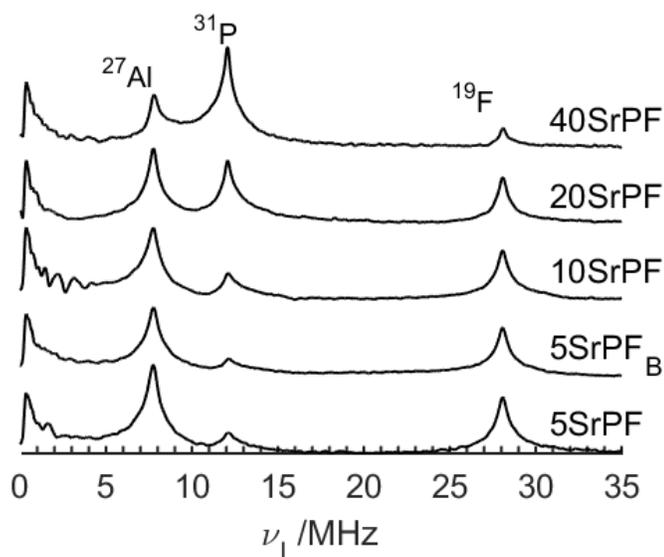
Figure 4-13. Three-pulse ESEEM spectra for the studied glasses. The code 5SrPF$_B$ denotes the sample melted in the presence of excess ammonium bifluoride. The spectra were recorded at magnetic field strength of 700 mT. Each spectrum was obtained from the co-addition of spectra for τ = 100 ns, 120 ns and 140 ns (τ is the first delay in the three-pulse sequence), resulting in blind-spot-free spectra. Resonances are marked with the correspondent nuclear species.

Each set of ESEEM spectra in Fig. 4-13 was measured under identical conditions, which allows us to compare the relative peak intensities of the observed resonances.[50] As expected from the batch compositions, the ^{27}Al/^{31}P peak amplitude ratio increases systematically with increasing Al/P ratio in the glasses and the same is true for the ^{31}P/^{19}F peak intensity ratio as a function of the P/F nominal ratio. This behavior indicates that the Yb^{3+} ions are well dispersed in the glassy matrix, i.e. there is no evidence of phase separation or sequestration of ytterbium. Fig. 4-14 shows the ^{31}P/^{19}F ESEEM peak intensity ratios $I(^{31}$P$)/I(^{19}$F$)$ as a function of the P/F ratio of the batch (red triangles) compared with data from the glass system 25BaF$_2$-25SrF$_2$-(30-x)Al(PO$_3$)$_3$-xAlF$_3$-20MF$_3$, where M = Y (blue triangles)[21] or Sc (black circles) and $10 \leq x \leq 25$.[20] The monotonic increase in this ratio suggests that the interaction of the Yb^{3+} ions with the fluoride ions is successively strengthened with increasing fluoride content of the glasses.
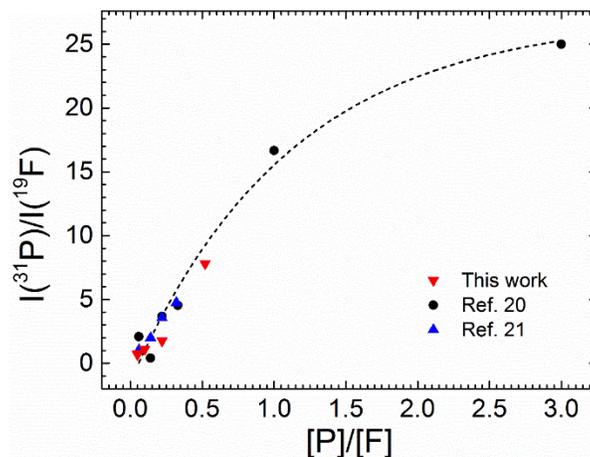
Figure 4-14. $^{31}P/^{19}F$ ESEEM peak intensity ratios $I(^{31}P)/I(^{19}F)$ as a function of the P/F ratio of the batch for the glasses studied in the present work (red triangles) compared with data from the glass system $25BaF_2$-$25SrF_2$-$(30-x)Al(PO_3)_3$-$xAlF_3$-$20MF_3$, where M = Y (blue triangles)[21] or Sc (black circles).[20] Dashed lines are drawn as guide to the eyes.

Fig. 4-15 shows the HYSCORE spectra obtained at 500 mT. All resonances were observed in the (+,+) quadrant of the spectra. The diagonal peaks correspond to the Zeeman frequencies of ^{27}Al, ^{31}P and ^{19}F nuclei. Such resonances near the diagonal indicate that the electron-nucleus interactions for these species correspond to the weak coupling-limit, as also observed in the ESEEM spectra discussed above. On the other hand, besides the diagonal peak at the ^{19}F Larmor frequency, a pair of non-diagonal resonances can be observed in the HYSCORE spectra, which are symmetrically displaced from the diagonal position corresponding to the ^{19}F Larmor frequency. These correlation peaks give direct evidence of ^{19}F species strongly interacting with the unpaired electron in Yb^{3+} and are attributed to direct Yb-F bonds. These off-diagonal signals are observed for all the samples, except for sample 40SrPF_Yb, with the same lineshape, but a systematic increase in intensity with increasing F/P ratio. This result indicates that the hyperfine coupling strength for these species is the same for all the samples, and that the intensity changes reflect a systematic increase in the total number of Yb-F bonds with increasing F/P ratio.
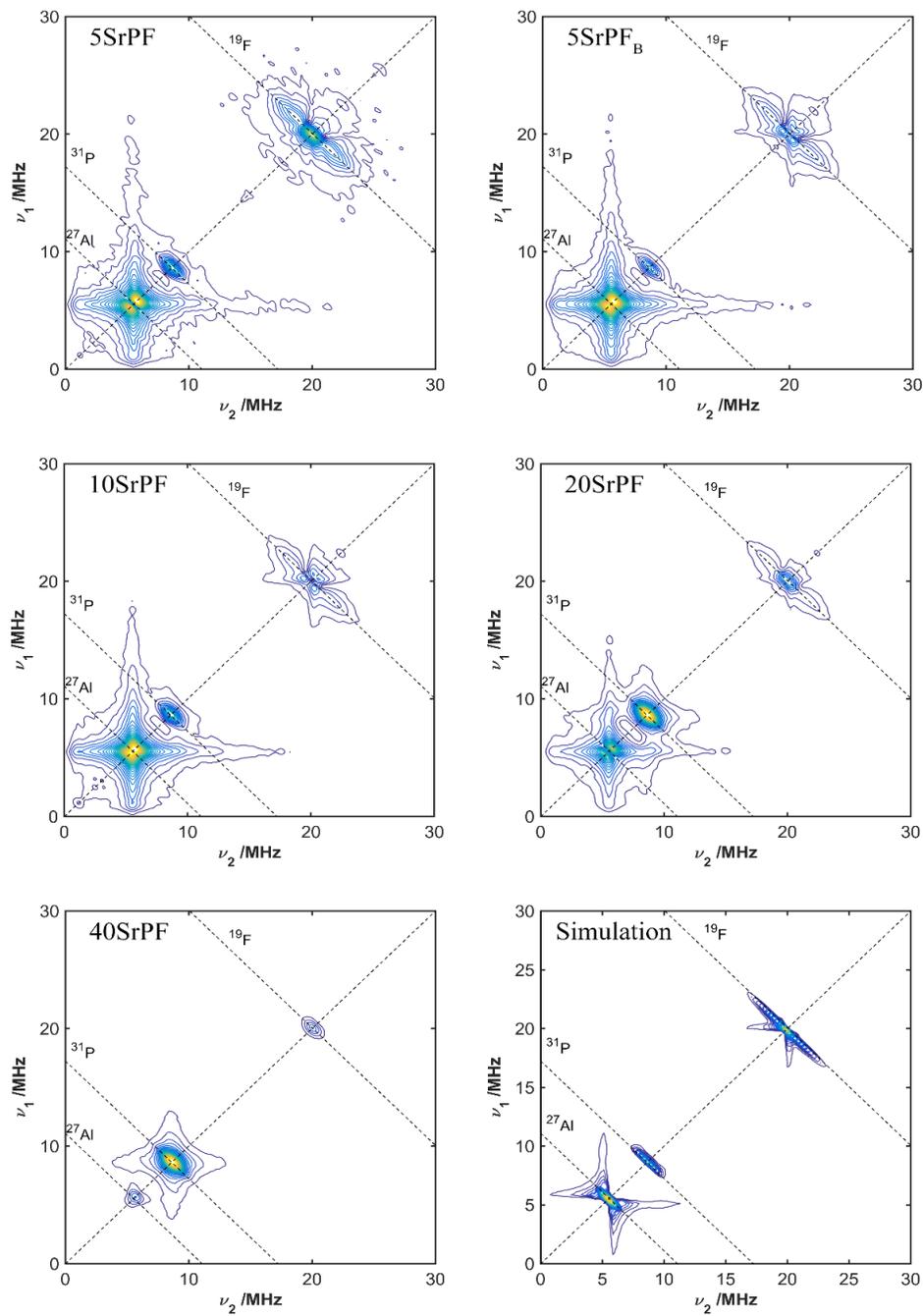
Figure 4-15. 2D-HYSCORE spectra recorded at a magnetic field strength of 500 mT for the studied glasses The code $5SrPF_B$ denotes the sample melted in the presence of excess ammonium bifluoride. The anti-diagonal dashed lines cross the diagonal at the nuclear Zeeman frequencies for the isotopes indicated in the plots. A simulation considering one [27]Al, one ^{31}P and two ^{19}F species interacting with the electron spin through the hyperfine interaction is also shown. The simulation parameters are described in the text.

In order to obtain an approximation of the electron-nuclear hyperfine coupling strengths a simplified simulation was performed with which the splittings observed experimentally were reproduced. The simulation considers an electron spin (S = ½) interacting with ^{27}Al, ^{31}P and ^{19}F isotopes. An axial g-tensor was assumed, with parameters $g_\perp = 1.4$ and $g_\parallel = 0.5$, which is an approximation for the distribution of g values observed in the EDFS spectra. No substantial changes are observed in the HYSCORE simulations for a variation of $\pm$ 0.5 in $g_\perp$ and $\pm$ 0.2 in $g_\parallel$. In order to reproduce the experimental data the simulation should consider that each Yb^{3+} ion is interacting with two distinct types of ^{19}F nuclei: a strongly coupled one, giving rise to the split signal and a weakly coupled one, with its resonance at the ^{19}F nuclear Zeeman frequency. For the ^{27}Al nucleus a quadrupole coupling parameter $C_Q = 3$ MHz and an asymmetry parameter $\eta_Q = 0.5$ was used in the simulations. This value of C_Q is the average value observed in the TQMAS experiments for the set of samples and a variation of $\pm$ 1 MHz does not change substantially the simulated lineshape. The hyperfine coupling parameters used in the simulations are: ^{27}Al $- A_\perp = 0.2 \pm$ 0.3 MHz, $A_\parallel = 1.7 \pm 0.7$ MHz; ^{31}P $- A_\perp = 0 \pm 0.5$ MHz, $A_\parallel = 3 \pm 1$ MHz; ^{19}F $- A_\perp = $ -0.4 $\pm$ 0.5 MHz, $A_\parallel = 0.8 \pm 1$ MHz for the weakly coupled site and $A_\perp = 1.0 \pm 0.5$ MHz, $A_\parallel = 10 \pm$ 2 MHz for the strongly coupled site.

4.4. CONCLUSIONS

In conclusion, we have provided quantitative insights into the network organization and rare-earth coordination in a well-established fluoride-phosphate glass system x Sr(PO$_3$)$_2$ $-$ (100-x) (AlF$_3$-CaF$_2$-SrF$_2$) with different P/F ratios by means of NMR, with the EPR probe Yb^{3+}and the optical probe Eu^{3+}. Raman and NMR data suggest that the network structure of the glasses is dominated by the formation of Al-O-P linkages which could be quantified by ^{27}Al/^{31}P double resonance NMR and by contributions of different Q$^{(n)}$ units. The fluoride ions are dominantly found in a mixed Al/Ca/Sr/Mg environment. The local environment of the rare-earth ions is characterized by mixed phosphate/fluoride ligation, which can be quantified by EPR and optical spectroscopy. Phosphate-rare earth ligation remains even at the highest

fluoride content in these glasses, as observed in previous literature reports on related systems.[8,20,21]

Acknowledgments

4.5. References

1   R. Lebullenger, L. A. O. Nunes and A. C. Hernandes, Properties of glasses from fluoride to phosphate composition, *J. Non. Cryst. Solids*, 2001, **284**, 55–60.

2   D. Ehrt, in *Proc. of SPIE*, eds. J. B. Breckinridge and A. J. Marker III, 1993, vol. 1761, pp. 213–222.

3   P. Wang, M. Lu, F. Gao, H. Guo, Y. Xu, C. Hou, Z. Zhou and B. Peng, Luminescence in the fluoride-containing phosphate-based glasses: A possible origin of their high resistance to nanosecond pulse laser-induced damage, *Sci. Rep.*, 2015, **5**, 8593.

4   D. Ehrt, REVIEW: Phosphate and fluoride phosphate optical glasses — properties, structure and applications, *Phys. Chem. Glas. Eur. J. Glas. Sci. Technol. Part B*, 2015, **56**, 217–234.

5   H. Ebendorff-Heidepriem and D. Ehrt, UV radiation effects in fluoride phosphate glasses, *J. Non. Cryst. Solids*, 1996, **196**, 113–117.

6   X. Zou and H. Toratani, Radiation resistance of fluorophosphate glasses for high performance optical fiber in the ultraviolet region, *J. Appl. Phys.*, 1997, **81**, 3354–3362.

7 D. Ehrt, M. Carl, T. Kittel, M. Müller and W. Seeber, High-performance glass for the deep ultraviolet range, *J. Non. Cryst. Solids*, 1994, **177**, 405–419.

8 T. S. Gonçalves, R. J. Moreira Silva, M. de Oliveira Junior, C. R. Ferrari, G. Y. Poirier, H. Eckert and A. S. S. de Camargo, Structure-property relations in new fluorophosphate glasses singly- and co-doped with Er^{3+} and Yb^{3+}, *Mater. Chem. Phys.*, 2015, **157**, 45–55.

9 J. F. Philipps, T. Töpfer, H. Ebendorff-Heidepriem, D. Ehrt and R. Sauerbrey, Spectroscopic and lasing properties of Er^{3+}:Yb^{3+}-doped fluoride phosphate glasses, *Appl. Phys. B*, 2001, **72**, 399–405.

10 H. Ebendorff-Heidepriem and D. Ehrt, Spectroscopic properties of Eu^{3+} and Tb^{3+} ions for local structure investigations of fluoride phosphate and phosphate glasses, *J. Non. Cryst. Solids*, 1996, **208**, 205–216.

11 C. A. G. Kalnins, H. Ebendorff-Heidepriem, N. A. Spooner and T. M. Monro, Enhanced radiation dosimetry of fluoride phosphate glass optical fibres by terbium (III) doping, *Opt. Mater. Express*, 2016, **6**, 3692.

12 C. A. G. Kalnins, H. E. Heidepriem, A. Dowler and T. M. Monro, in *2011 International Quantum Electronics Conference (IQEC) and Conference on Lasers and Electro-Optics (CLEO) Pacific Rim incorporating the Australasian Conference on Optics, Lasers and Spectroscopy and the Australian Conference on Optical Fibre Technology*, IEEE, 2011, pp. 2051–2053.

13 G. Galleani, Y. Ledemi, E. S. de Lima Filho, S. Morency, G. Delaizir, S. Chenu, J. R. Duclere and Y. Messaddeq, UV-transmitting step-index fluorophosphate glass fiber fabricated by the crucible technique, *Opt. Mater. (Amst).*, 2017, **64**, 524–532.

14 C. A. G. Kalnins, H. Ebendorff-Heidepriem, N. A. Spooner and T. M. Monro, Optically stimulated luminescence in fluoride-phosphate glass for radiation dosimetry, *J. Am. Ceram. Soc.*, 2011, **94**, 474–477.

15 C. Wang, P. Wang, X. Liu, L. Hu and L. Zhang, Influence of chemical polishing on fluorophosphate fiber preform, *Ceram. Int.*, 2016, **42**, 5629–5634.

16 D. Möncke, D. Ehrt, L. L. Velli, C. P. E. Varsamis, E. I. Kamitsos, S. Elbers and H. Eckert, Comparative spectroscopic investigation of different types of fluoride phosphate glasses, *Phys. Chem. Glas. - Eur. J. Glas. Sci. andTechnology Part B*, 2007, **48**, 399–402.

17 B. Karmakar, P. Kundu and R. N. Dwivedi, UV transparency and structure of fluorophosphate glasses, *Mater. Lett.*, 2002, **57**, 953–958.

18 R. K. Brow, Z. A. Osborne and R. J. Kirkpatrick, A multinuclear MAS NMR study of the short-range structure of fiuorophosphate glass, *J. Mater. Res.*, 1992, **7**, 1892–1899.

19 T. Djouama, M. Poulain, B. Bureau and R. Lebullenger, Structural investigation of fluorophosphate glasses by ^{19}F, ^{31}P MAS-NMR and IR spectroscopy, *J. Non. Cryst. Solids*, 2015, **414**, 16–20.

20 M. de Oliveira, T. S. Gonçalves, C. Ferrari, C. J. Magon, P. S. Pizani, A. S. S. de Camargo and H. Eckert, Structure–Property Relations in Fluorophosphate Glasses: An Integrated Spectroscopic Strategy, *J. Phys. Chem. C*, 2017, **121**, 2968–2986.

21 M. de Oliveira, T. Uesbeck, T. S. Gonçalves, C. J. Magon, P. S. Pizani, A. S. S. de Camargo and H. Eckert, Network Structure and Rare-Earth Ion Local Environments in Fluoride Phosphate Photonic Glasses Studied by Solid-State NMR and Electron Paramagnetic Resonance Spectroscopies, *J. Phys. Chem. C*, 2015, **119**, 24574–24587.

22 A. Lesage, M. Bardet and L. Emsley, Through-Bond Carbon- Carbon Connectivities in Disordered Solids by NMR, *J. Am. Chem. Soc*, 1999, **121**, 10987–10993.

23 M. Bertmer and H. Eckert, Dephasing of spin echoes by multiple heteronuclear dipolar interactions in rotational echo double resonance NMR experiments, *Solid State Nucl. Magn. Reson.*, 1999, **15**, 139–152.

24 T. Gullion, Measurement of dipolar interactions between spin- 1 2 and quadrupolar nuclei by rotational-echo, adiabatic-passage, double-resonance NMR, *Chem. Phys. Lett.*, 1995, **246**, 325–330.

25 M. Bak, J. T. Rasmussen and N. C. Nielsen, SIMPSON: A General Simulation Program for Solid-State NMR Spectroscopy, *J. Magn. Reson.*, 2000, **147**, 296–330.

26 D. Massiot, F. Fayon, M. Capron, I. King, L. Calv, B. Alonso, J. Durand, B. Bujoli, Z. Gan and G. Hoatson, Modelling one- and two-dimensional solid-state NMR spectra, 2002, **40**, 70–76.

27 T. Gullion and J. Schaefer, Rotational-Echo Double-Resonance NMR, *J. Magn. Reson.*, 1989, **81**, 196–200.

28 J. C. . Chan and H. Eckert, High-resolution [27]Al–[19]F solid-state double resonance NMR studies of AlF3–BaF2–CaF2 glasses, *J. Non. Cryst. Solids*, 2001, **284**, 16–21.

29 A. Schweiger and G. Jeschke, *Principles of Pulsed Electron Spin Resonance*, Oxford University Press, Oxford, 2001.

30 Y. Deligiannakis and A. W. Rutherford, Electron spin echo envelope modulation spectroscopy in photosystem I, *Biochim. Biophys. Acta - Bioenerg.*, 2001, **1507**, 226–246.

31 Y. Deligiannakis, M. Louloudi and N. Hadjiliadis, Electron spin echo envelope modulation (ESEEM) spectroscopy as a tool to investigate the coordination environment of metal centers, *Coord. Chem. Rev.*, 2000, **204**, 1–112.

32 D. Möncke, D. Ehrt, L. L. Velli, C. P. E. Varsamis and E. I. Kamitsos, Structure and properties of mixed phosphate and fluoride glasses, *Phys. Chem. Glas. J. Glas. Sci. Technol. Part B*, 2005, **46**, 67–71.

33 L. Zhang and H. Eckert, Short- and Medium-Range Order in Sodium Aluminophosphate Glasses: New Insights from High-Resolution Dipolar Solid-State NMR Spectroscopy, *J. Phys. Chem. B*, 2006, **110**, 8946–8958.

34 L. Zhang, C. C. De Araujo and H. Eckert, Structural role of fluoride in

aluminophosphate sol-gel glasses: High-resolution double-resonance NMR studies, *J. Phys. Chem. B*, 2007, **111**, 10402–10412.

35   A. Medek, J.S. Harwood and L. Frydman, Multiple-Quantum Magic- Angle Spinning NMR: A New Method for the Study of Quadrupolar Nuclei in Solids, *J. Am. Chem. Soc.*, 1995, **117**, 12779–12787.

36   J. P. Fletcher, S. H. Risbud and R. J. Kirkpatrick, MASS-NMR structural analysis of barium aluminofluorophosphate glasses with and without nitridation, *J. Mater. Res.*, 1990, **5**, 835–840.

37   T. J. Kiczenski and J. F. Stebbins, Fluorine sites in calcium and barium oxyfluorides: F-19 NMR on crystalline model compounds and glasses, *J. Non. Cryst. Solids*, 2002, **306**, 160–168.

38   A. Zheng, S.-B. Liu and F. Deng, [19]F Chemical Shift of Crystalline Metal Fluorides: Theoretical Predictions Based on Periodic Structure Models, *J. Phys. Chem. C*, 2009, **113**, 15018–15023.

39   J. H. Van Vleck, The Dipolar Broadening of Magnetic Resonance Lines in Crystals, *Phys. Rev.*, 1948, **74**, 1168–1183.

40   J. Durand, L. le Cot and J. L. Galigne, Etudes structurales de composes oxyfluores du P(V) II. Structure cristalline de Na2PO3F beta, *Acta Crystallogr. B*, 1974, **30**, 1565–1569.

41   T. V. Bocharova, A. M. Mironov and G. O. Karapetyan, Rare-earth-activated fluorophosphate glasses: Local environment of the activator and capture volume model, *Inorg. Mater.*, 2005, **41**, 892–899.

42   T. V. Bocharova, J. L. Adam, G. O. Karapetyan, F. Smektala, A. M. Mironov and N. O. Tagil'tseva, Analysis of rare-earth ion spatial distribution in fluorophosphate glasses in terms of segregation phenomenon, *J. Phys. Chem. Solids*, 2007, **68**, 978–982.

43   S. Tanabe, K. Hirao and N. Soga, Local structure of rare-earth ions in fluorophosphate glasses by phonon sideband and mössbauer spectroscopy, *J. Non. Cryst. Solids*, 1992, **142**, 148–154.

44   S. S. Babu, P. Babu, C. K. Jayasankar, W. Sievers, T. Tröster and G. Wortmann, Optical absorption and photoluminescence studies of Eu^{3+}-doped phosphate and fluorophosphate glasses, *J. Lumin.*, 2007, **126**, 109–120.

45   P. Babu, K. H. Jang, E. S. Kim, R. Vijaya, C. K. Jayasankar, V. Lavín and H. J. Seo, Local field dependent fluorescence properties of Eu^{3+} ions in a fluorometaphosphate laser glass, *J. Non. Cryst. Solids*, 2011, **357**, 2139–2147.

46   A. Kucuk and A. G. Clare, Optical properties of cerium and europium doped fluoroaluminate glasses, *Opt. Mater. (Amst).*, 1999, **13**, 279–287.

47   M. Poulain, a. Soufiane, Y. Messaddeq and M. a. Aegerter, Fluoride Glasses : Synthesis and Properties, *Brazilian J. Phys.*, 1992, **22**, 205–217.

48   S. Sen, R. Rakhmatullin, R. Gubaydullin and a. Silakov, A pulsed EPR study of clustering of Yb^{3+} ions incorporated in GeO_2 glass, *J. Non. Cryst. Solids*, 2004, **333**, 22–27.

49   R. Zhang, M. de Oliveira, Jr., Z. Wang, R. G. Fernandes, A. S. S. de Camargo, J. Ren, L. Zhang and H. Eckert, Structural Studies of Fluoroborate Laser Glasses by Solid State NMR and EPR Spectroscopies, *J. Phys. Chem. C*, 2017, **121**, 741–752.

50   H. Deters, J. F. J. F. de Lima, C. J. Magon, A. S. S. de Camargo, H. Eckert, Structural models for yttrium aluminium borate laser glasses: nmr and epr studies of the system $(Y_2O_3)(0.2)$-$(Al_2O_3)x$-$(B_2O_3)(0.8$-$X)$. *Phys. Chem. Chem. Phys.* **2011**, *13* (35), 16071–16083.

5. **Ultraviolet Upconversion Luminescence in a Highly Transparent Triply-Doped Gd^{3+}-Tm^{3+}-Yb^{3+} Fluoride-Phosphate Glasses.**

RÉSUMÉ DE L´ARTICLE INSÉRÉ

En raison de la haute transparence UV des verres FP, nous avons préparé des verres dopés avec des ions Gd^{3+}, Tm^{3+} et Yb^{3+} comme candidat potentiel pour la fabrication de lasers à fibre UV. Les propriétés de photoluminescence sous excitation au laser à diode de 980 nm ont été étudiées et l'effet du rapport fluorure/phosphate dans l'émission UV du Gd^{3+} a été vérifié. L'effet de la concentration du Gd^{3+} dans l'émission UV a également été étudié. Ensuite, en utilisant la technique de la double résonance ^{45}Sc/^{31}P, en utilisant le Scandium comme un mimétique diamagnétique pour les espèces luminescentes, la distribution du ligand entourant les ions a été quantifiée et l'efficacité de l'émission Gd^{3+} par rapport aux ions Tm^{3+} avec la structure a été effectuée.

Ultraviolet Upconversion Luminescence in a Highly Transparent Triply-Doped Gd³⁺-Tm³⁺-Yb³⁺ Fluoride-Phosphate Glasses

Gustavo Galleani[1], Silvia Helena Santagneli[1], Yannick Ledemi[2], Oliver Janka[3], Raigner Pottgen, Hellmut Eckert[4,5] Younes Messaddeq[1,2]

1. *Institute of Chemistry – São Paulo State University/UNESP – Araraquara-SP, Brazil*

2. *Center for Optics, Photonics and Lasers – Laval University – Québec-QC, Canada*

3. *Institut für Anorganische und Analytische Chemie, WWU Münster, Germany*

4. *Institut für Physikalische Chemie, WWU Münster, Germany*

5 *Instituto de Física de São Carlos, Universidade de São Paulo, São Carlos, SP. Brasil*

ABSTRACT

We report near infrared to ultraviolet (UV) upconversion emissions in triply-doped Gd³⁺-Tm³⁺-Yb³⁺ fluoride-phosphate glasses. Emission at 310 nm, originated from the Gd³⁺: $^6P_{7/2} \rightarrow {}^8S_{7/2}$ transition was observed for the first time in glasses. The high-purity glasses prepared exhibit extended transparency in the UV down to 200-250 nm. The mixed fluoride/phosphate environment of the rare-earth (RE) ions was characterized by means of NMR techniques using scandium as a diamagnetic mimic for the luminescent species, for which the ligand distribution was quantified by $^{45}Sc\{^{31}P\}$ rotational echo double resonance NMR. Both the intensity of the Gd³⁺ emission as well as those of the UV emissions at 290, 347 and 363 nm increase with increasing ratio of fluoride to phosphate ligands coordinating to the rare-earth ion.
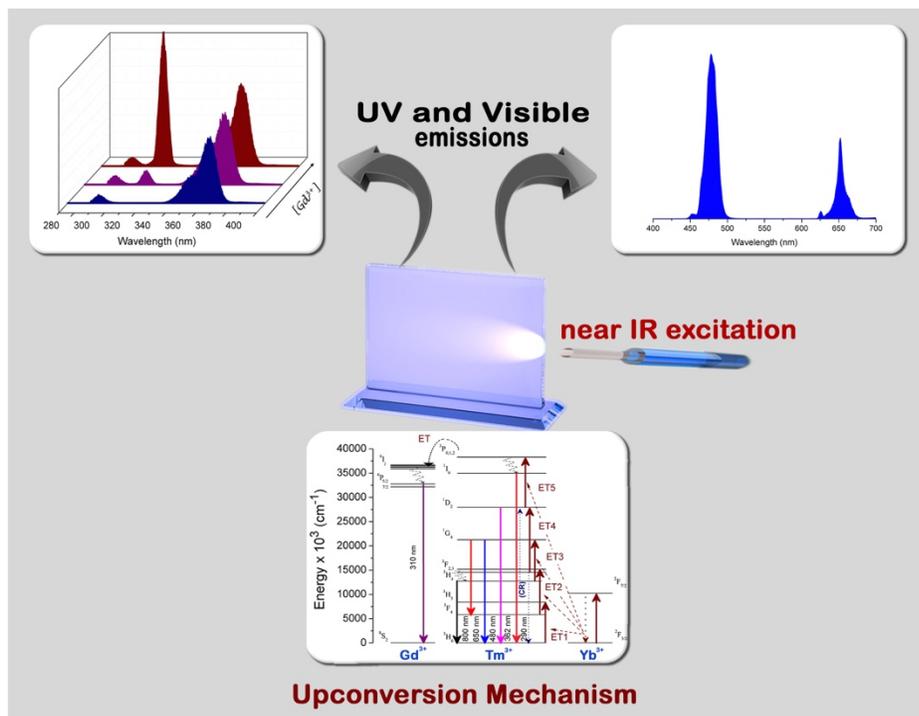
GRAPHICAL TABLE OF CONTENT

5.1. Introduction

Frequency upconversion (UC) of infrared (IR) light to ultraviolet (UV) light with trivalent rare-earth (RE) ions has received great attention in recent years thanks to the development and availability of laser diodes as a convenient source of near IR light. UV light is employed in a broad range of applications in commercial, industrial and healthcare settings such as curing of coating materials, microbial disinfection in surfaces, water treatment, counterfeit detection in financial documents, photolithography, phototherapy and in forensic investigations, to name a few.[1] UV solid-state and/or fiber lasers are also used in color displays, high density memories, IR radiation detection, optical storage, and environmental monitoring.[2–5]

To get improved UV emissions of RE embedded in solid-state host matrices upon longer-wavelength laser excitation, low-phonon hosts as fluoride crystals, fluoride and chalcogenide glasses doped with Nd^{3+}, Pr^{3+}, Ho^{3+} Tm^{3+} and Er^{3+} ions have been widely studied.[6–11] However, the production of fluoride crystals is expensive and not suitable for large-scale manufacturing, while fluoride glasses usually have poor mechanical properties and chemical stability, and chalcogenide glasses are not transparent in the UV regio. On the other hand, fluoride phosphate glasses offer the prospect of combining the desirable optical properties of fluoride hosts with the favorable mechanical properties of phosphate glasses[12–14] Fluoride-phosphate glasses and optical fibers, when produced with ultra-high purity reagents can be highly transparent in the UV (down to ~160 nm), contributing to the efficiency of photoemission in this region. [15–17]

There have been several reports on the spectroscopic and structural properties of RE^{3+}-doped fluoride-phosphate glasses [18–22], where the local environment of the RE ions was shown to be characterized by mixed fluoride/phosphate ligation. At sufficiently low P/F ratios the local environment of the rare earth ions seems to be dominated by fluoride ligation, important for higher emission efficiency and phonon-assisted energy transfer processes. Quantitative insights on the ligand distributions around the rare-earth ions can be obtained by using double resonance NMR studies involving the nuclear isotope ^{45}Sc (spin -7/2) as

diamagnetic mimics of the RE ions.[23] Sc^{3+}, with an ionic radius of 83 pm has may serve as a suitable model for small ions such as Yb^{3+} (86 pm) or Tm^{3+} (94 pm).

Recently, special attention has been paid to various materials, particularly low phonon fluoride nanocrystals as $NaYF_4$ and $NaGdF_4$. jointly doped with Tm^{3+} and Yb^{3+} and triply-doped with Gd^{3+}, Tm^{3+}, and Yb^{3+}, [24–27] Thulium ions have received increased interest because they have suitable metastable levels for UV UC emissions. Owing to their unique and simple energy level diagram with only a single transition ($^2F_{7/2}$ -> $^2F_{5/2}$) ytterbium ions are frequently introduced as a sensitizer centers at ~1 μm pumping wavelength, producing large enhancements of UC luminescence of Tm^{3+} ions activators. Thus, efficient UV UC emissions induced by near IR light have been reported for some Tm^{3+}-Yb^{3+} co-doped materials. [28–32] Owing to the large energy gap (32000 cm^{-1}) separating the Gd^{3+} ground state $^8S_{7/2}$ and the first excited state $^6P_{7/2}$, Gd^{3+} levels cannot be populated directly by IR pumping. On the other hand, introduction of Gd^{3+} to Tm^{3+}-Yb^{3+} co-doped materials can provide additional UV UC emissions, important for building UV compact devices. [24,25,33–35] Four UC emission peaks of Gd^{3+} were observed in the range 190 – 210 nm, [35] one in 253 nm, [25–27] three peaks in the range 270-281 nm [25–27] and one at 311 nm [24–27] involving up to seven photon processes. In glasses, some works report UV UC in Tm^{3+}-Yb^{3+} co-doped fluoride glasses, [36,37] with the shortest emission observed at 290 nm upon near IR excitation. UV UC emissions from Gd^{3+} upon near IR excitation have never been reported, to the best of our knowledge. Spectral properties of Gd^{3+} have been studied in glasses especially under UV and VUV excitation. [38]

Here, we report, to the best of our knowledge for the first time, a middle-UV UC emission of Gd^{3+} ions (310 nm) in Gd^{3+}-Tm^{3+}-Yb^{3+} triply-doped fluoride-phosphate glasses excited by a 980 nm laser diode. Also, middle and near-UV (290, 347 and 363 nm) and visible UC (480 and 650 nm) emissions of Tm^{3+} were observed. To better understand the structural and the local environment for the RE ions and its influence on the Gd^{3+} UV UC emission, glasses with different phosphate/fluoride ratios were prepared and studied by solid-state NMR techniques. To this end, the paramagnetic Gd^{3+}, Tm^{3+} and Yb^{3+} ions are replaced by their diamagnetic mimic, Sc^{3+}.

5.2. Experimental Procedure

5.2.1. Bulk glass synthesis:

Fluoride-phosphate vitreous samples were prepared by the conventional melt-quenching method as described in Ref. [15]. Starting materials were AlF_3 (MV labs, 99.999 %), SrF_2 (Sigma, 99.995 %), CaF_2 (Sigma, 99.99 %), MgF_2 (Cerac, 99.999%), GdF_3 (Sigma, 99.99 %), TmF_3 (MV labs, 99.99 %), YbF_3 (Alfa Aesar, 99.99%), ScF_3 and strontium phosphate $Sr(PO_3)_2$. $Sr(PO_3)_2$ was prepared from the solid-state reaction of $NH_4H_2PO_4$ (Sigma, 99.999%) with $SrCO_3$ (Alfa Aesar, 99.994%). ScF_3 was prepared by heating Sc_2O_3 (Strem Chemicals, 99.9%) with an excess of ammonium bifluoride (NH_4HF_2, Alfa Aesar, 95%) in a platinum crucible at 330 °C in air during 3 h. After the fluorination, the powder was heated to 700 °C during 30 min to ensure the complete elimination of NH_3 and HF from the decomposition of ammonium bifluoride. The identity of the ScF_3 prepared in this manner was confirmed by solid state NMR and x-ray powder diffraction (not shown here). All the components were weighed and mixed to obtain 10 g bulk glasses with molar compositions detailed in Table 5-1.

Table 5-1: Glass labels, composition (mol%) and glass transition temperature (T_g) of the investigated glasses.

Glass label	$Sr(PO_3)_2$ (mol%)	AlF_3 (mol%)	CaF_2 (mol%)	MgF_2 (mol%)	SrF_2 (mol%)	ScF_3 (mol%)	GdF_3 (mol%)	TmF_3 (mol%)	YbF_3 (mol%)	Tg (±2°C)
5PF	5.0	38.0	25.0	11.0	21.0	-	-	-	-	439
10PF	10.0	35.0	30.0	10.0	15.0	-	-	-	-	447
5PF6Sc	4.7	35.7	23.5	10.3	19.7	6.0	-	-	-	432
10PF6Sc	9.4	32.9	28.2	9.4	14.1	6.00	-	-	-	449
5PF2Gd	3.80	35.80	29.80	9.70	14.8	-	2.00	0.10	4.00	434

10PF0Gd	9.2	34.2	29.2	9.2	14.1	-	-	0.1	4.0	450
10PF2Gd	8.8	33.8	28.8	8.8	13.7	-	2.0	0.1	4.0	448
10PF4Gd	8.4	33.4	28.4	8.4	13.4	-	4.0	0.1	4.0	445

Semiquantitative EDX analyses of the polished glass pieces were carried out by the use of a Zeiss EVO® MA10 scanning electron microscope in variable pressure mode (60 Pa N_2) with the SiO_2, MgF_2, MgO, Al_2O_3, GaP, $Ca_3[Si_3O_9]$ (wollastonite), Sc, SrF_2 and the rare earth trifluorides REF_3 (RE = Gd, Tm, Yb) as standards. For each sample four spots and one area measurement was conducted. All measurements were in accordance with each other. The experimentally observed and weighed compositions are listed in Table S1 (Supporting Materials Section) and are in good agreement; no impurity elements were detected. The measurement error for the elements of Mg and the respective heavier ones is within 2 at.%, the error for O and F is at least 4-5 at. %. Due to the semiquantitative analysis and the subsequent determination problems for O and F, the respective deviations for the other elements are explained.

5.2.2. Glass sample characterization.

Differential scanning calorimetric (DSC) measurements were performed on ~ 20 mg glass pieces in Al pans using a TA Instruments 2910 calorimeter at a heating rate of 10 °C.min⁻¹ under nitrogen atmosphere. Electronic absorption spectra were measured from 180 to 1100 nm on polished samples of around 2 mm in thickness using a Cary 500 (Varian) double-beam spectrometer, Since oxygen from the ambient atmosphere absorbs in the range of 180-200 nm, the sample chamber was purged with N_2 during the measurements.

The UC emission spectra of the glass samples were recorded using a Horiba Jobin-Yvon Nanolog fluorimeter equipped with a photomultiplier tube (PMT) sensitive from 250 to 825 nm. A diode laser operating at 980 nm coupled with a standard multimode fiber (200 μm core diameter) was used to excite the bulk glass samples by focusing on the sample

surface through a lens with a 13-mm focal length. These measurements were performed at room temperature (~21.5 °C) and corrected by the instrumental response.

Solid State NMR spectra of the ^{31}P ,^{27}Al and ^{45}Sc nuclei were carried out on a Bruker Avance III spectrometer operating at 400 MHz, equipped with a 4 mm probe. ^{27}Al MAS-NMR spectra were recorded using short pulses of 1 μs length and a relaxation delay of 5 s. Chemical shifts are reported relative to a 1 mol.L^{-1} Al(NO$_3$)$_3$ aqueous solution. ^{45}Sc MAS-NMR spectra were recorded using short pulses of 0.5 μs length and a relaxation delay of 2 s. Chemical shifts are reported relative to a 1 M ScCl$_3$ aqueous solution, using solid ScF$_3$ as a secondary reference (δ = −52 ppm).[39] ^{31}P MAS-NMR spectra were recorded using a pulse of 3.3 μs length and a relaxation delay of 300 s. Chemical shifts were referenced against an external 85% H$_3$PO$_4$ standard.

^{27}Al{^{31}P} rotational echo double resonance (REDOR) measurements were done using the standard Gullion-Schaefer sequence with π recoupling pulses of 6.3 μs length on the ^{31}P channel and acquisition of rotor-synchronized ^{27}Al spin echoes. The second moments M$_{2(Al-P)}$ characterizing the dipolar interaction between the quadrupolar observation nuclei (^{27}Al in the present case) and the neighboring ^{31}P nuclei (I = ½), was obtained by applying a parabolic fit to the REDOR data within the S/S$_0$ ≤ 0.2 range, to the expression[40]

$$\frac{\Delta S}{S_0} = \frac{4}{3\pi^2}(NT_R)^2 M_{2(Al-P)} \qquad (1)$$

The experiments were carried out at two different MAS frequencies (12.0 and 14.0 kHz) in order to acquire a sufficient number of data points within the short mixing time limit. No ^{19}F decoupling was done. From the obtained M$_{2(Al-P)}$ values, an average number of Al−O−P linkages can be estimated by comparison with corresponding REDOR data measured on the crystalline model compound Al(PO$_3$)$_3$ (six Al-O-P linkages). ^{31}P{^{27}Al} Rotational Echo Adiabatic Passage Double Resonance (REAPDOR) [41] experiments were carried out using a ^{31}P π -pulse duration of 3.15 μs and a spinning frequency of 12.0 kHz. Dipolar recoupling was achieved via an adiabatic ^{27}Al mixing pulse lasting 1/3 of the rotor period. The ^{27}Al nutation frequency applied for these experiments was 52.1 kHz. A recycle delay of 250 s was applied in combination with a presaturation train of ten π /2 pulses. To get quantitative information, the ^{31}P{^{27}Al} REAPDOR dephasing curves were simulated

using the SIMPSON program package, [42] based on the nutation frequency used and the experimental values of the ^{27}Al quadrupolar coupling strength obtained from ^{27}Al MAS-NMR. The REAPDOR response of a ^{31}P(^{27}Al)$_2$ three spin system (present in the model compound Al(PO$_3$)$_3$) was calculated on the basis of the relevant internuclear distance of 327 pm. ^{45}Sc{^{31}P} REDOR experiments were done at a MAS frequency of 12.0 kHz using the Gullion-Schaefer sequence, and calibrated with ScPO$_4$. The second moments M$_{2(Sc-P)}$ characterizing the dipolar interaction between ^{45}Sc and the neighboring ^{31}P nuclei (I = ½), were again analyzed via eq. (1), applying a parabolic fit to the REDOR data within the S/S$_0$ ≤ 0.2 range.

^{19}F MAS-NMR spectra were measured on an Agilent DD2 spectrometer operating at 5.7 T. The spectra were recorded in 1.6 mm rotors spinning at 35.0 kHz, using a rotor-synchronized Hahn-Echo sequence with 4 to 8 rotor cycles for the echo formation in order to remove the probe background signal. Different evolution times were tested and it was found that the values used in the experiments do not influence the relative intensities of the resolved spectral components, indicating similar spin-spin relaxation times. 90° pulses of 1.65 μs length and relaxation delays of 20 s were used. Chemical shifts are reported relative to CFCl$_3$ using solid AlF$_3$ as a secondary reference (−172 ppm).[43]

5.3. Results and discussion

The glasses were visually transparent and homogeneous. Table 5-1 summarizes the glass compositions, and their respective glass transition temperatures, T_g. The latter are consistent with published values for glasses having similar compositions. [12,19,20,23]. While glasses containing 5 mol % of phosphate showed a small decrease of T_g upon rare-earth ion addition; this effect was not observed for samples containing 10 mol % of phosphate.

As fluoride losses and/or replacement by oxide species are an important issue in the preparation of fluoride-phosphate glasses, the atomic percentage (at %) of each element contained in the glass was analyzed by X-ray fluorescence (see Supporting Materials Section). Based on the results obtained we conclude that are no significant fluoride losses or oxygen incorporation occurred during the glass preparation.

To better understand the structural organization of the glasses and the influence of the local environment of the RE ions upon the UC emissions, the 5PF6Sc and 10PF6Sc glasses were studied by solid state NMR on samples in which the paramagnetic species Gd^{3+}, Tm^{3+} and Yb^{3+} were replaced by equal amounts of their diamagnetic mimic Sc^{3+}.

The single-pulse ^{31}P and ^{27}Al MAS NMR spectra of the glass samples (5PF6Sc and 10PF6Sc) are shown in Figure 5-1a and b respectively. ^{31}P MAS NMR spectra presented a broad and asymmetric lineshape near -10 ppm. Comparison of this lineshape with previously published spectra of similar glasses suggests multiple contributions of $Q^{(n)}$ phosphate units, with a dominance of $Q^{(0)}$ units species. [44]. The ^{27}Al MAS NMR spectra (Figure 5-1b) show an asymmetric lineshape typical of six-coordinated aluminum. Similar results were obtained previously on analogous glasses not containing scandium fluoride.
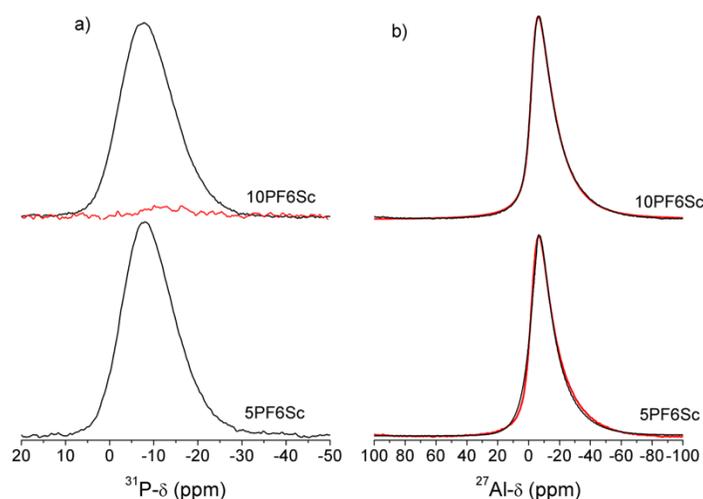

Figure 5-1. (a) Refocused INADEQUATE (red traces) and single-pulse ^{31}P MAS-NMR and (b) ^{27}Al MAS-NMR spectra of the 5PF6Sc and 10PF6Sc fluoride-phosphate glasses (black curves). Red curves represent simulations of the data using the Czjzek model.

Quantitative information regarding Al-O-P and P-O-Al connectivities was obtained by $^{27}Al\{^{31}P\}$ REDOR and $^{31}P\{^{27}Al\}$ REAPDOR experiments. Figure 5-2 shows the $^{27}Al\{^{31}P\}$ REDOR dephasing curves for the 5PF6Sc and 10PF6Sc samples and of the crystalline model

compound $Al(PO_3)_3$. For the latter compound the apparent $M_{2(Al-P)}$ value obtained via eq. (1) must be compared with the theoretical value of 6.4, resulting in a calibration factor of 1.1 Calibration factors of this order of magnitude are quite common, as off-resonance effects due to the chemical shift anisotropy of the I nuclei, pulse errors and other imperfection tend to reduce the efficiency of dipolar recoupling. The thus corrected $M_{2(Al-P)}$ values are summarized in Table 5-2. The $M_{2(Al-P)}$ values obtained $0.86 \times 10^6 \text{rad}^2\text{s}^{-2}$ (5PF6Sc) and $1.23 \times 10^6 \text{rad}^2\text{s}^{-2}$ (10PF6Sc) glasses are comparable with those of other fluoride-phosphate glasses previously studied. [19,20,23]
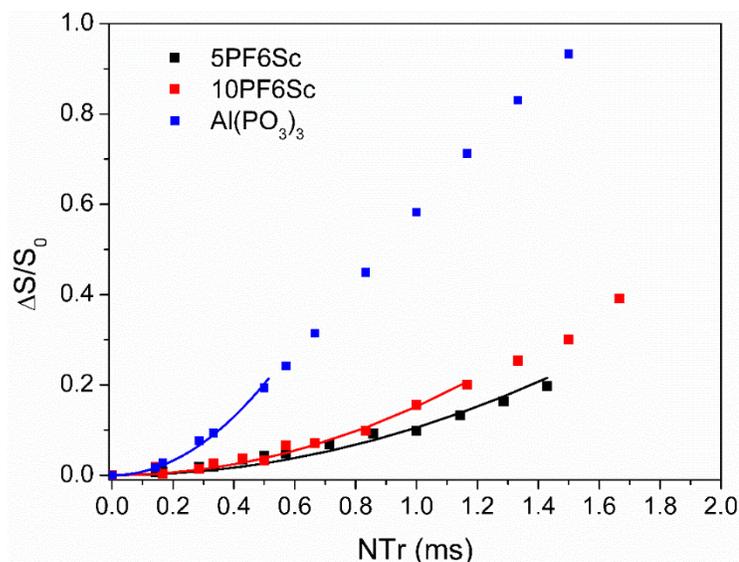

Figure 5.2. $^{27}Al\{^{31}P\}$ REDOR dephasing curves for the 5PF6Sc and 10PF6Sc glass samples and crystalline $Al(PO_3)_3$. Squares represent experimental data obtained under MAS spinning speeds of 14.0 and 12.0 kHz. Solid curves are parabolic fits to the data, analyzed within the data range of $\Delta S/S_0 \leq 0.2$.

The average number of P atoms in the second coordination sphere of Al in the glasses, N_{Al-O-P}, was obtained via the expression $N_{Al-O-P} = 6 \times M_{2(Al-P)}(exp)/M_{2(Al-P)}(Al(PO_3)_3)$ measured in $Al(PO_3)_3$ (6 Al-O-P linkages at a distance of 327 pm). We find N_{Al-O-P} values of 0.8 and 1.2 for the 5PF6Sc and 10PF6Sc glasses, respectively. Based on the ^{27}Al MAS NMR results that all of the Al species are six-coordinated in the glasses present, the average number

of F atoms coordinated to Al is given by $N_F = 6 - N_{Al-O-P}$ leading to 5.2 and 4.8 Al-F bonds for the 5PF6Sc and 10PF6Sc glasses, respectively. The number of Al-O-P linkages was obtained by multiplying the N_{Al-O-P} with the Al content of the glass (35.7 mol% for the 5PF6Sc sample and 32.9 mol% for the 10PFSc sample) and is summarized in Table 5-2. We found ~32 and ~43 Al-O-P linkages for the 5PF6Sc and 10PF6Sc samples, respectively. This number shows that the substitution of RE ions by scandium in the glasses has no significant influence on the Al-O-P linkage formation, as observed by Oliveira *et al.* [23] and by us in our previous work. [44]

Table 5-2. Values of second moments $M_{2(Al-P)}$ (±10%) obtained from $^{27}Al\{^{31}P\}$ REDOR experiments and connectivity data on glasses. N_P and N_F are respectively the number of P atoms and the number of F atoms in the six-coordinate Al-coordination environment, obtained experimentally from REDOR results. N_{Al-O-P} (REDOR) is the total number of Al-O-P linkages obtained from the $^{27}Al\{^{31}P\}$ REDOR experiments and N_{P-O-Al} (REAPDOR) is the total number of P-O-Al linkages obtained from the $^{31}P\{^{27}Al\}$ REAPDOR experiments.

Glass Sample	$M_{2(Al-P)}$ $(\times10^6 rad^2 s^{-2})$	N_P	N_F	N_{Al-O-P} (REDOR)	N_{P-O-Al} (REAPDOR)
5PF[a]	0.77	0.8	5.2	30	20
10PF[a]	1.01	1.0	5.0	37	40
5PF6Sc	0.86	0.9	5.1	32	19
10PF6Sc	1.23	1.3	4.7	43	38
Al(PO$_3$)$_3$	5.80	6.0	-	-	-

[a] Reference [44]

Figure 5-3 shows the $^{31}P\{^{27}Al\}$ REAPDOR dephasing curves for the 5PF6Sc and 10PF6Sc glasses. The experimental data matches with a simulation considering spin-systems involving ^{31}P and two ^{27}Al nuclei, assuming that the average P-Al distance across a P-O-Al linkage is 327 pm (as observed in the crystalline Al(PO$_3$)$_3$ compound) with an O-P-O angle of 109.4°. The results are detailed in Table 5-2. A nuclear electric quadrupolar coupling constant of 4.06 MHz, consistent with previous results[23] was assumed in these simulations.

Thus, the number of P-O-Al linkages N_{P-O-Al} was calculated by assuming that on average each P atom has two P-O-Al linkages; as indicated by the REAPDOR results. Table 5-2 indicates that this number is reasonably consistent with the corresponding number N_{Al-O-P} from the REDOR studies.
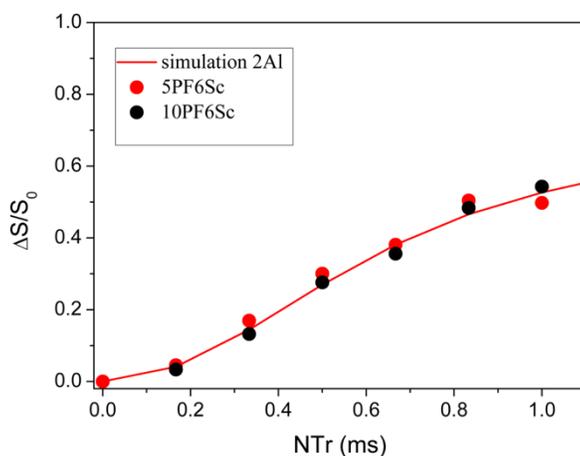

Figure 5-3. $^{31}P\{^{27}Al\}$ REAPDOR dephasing curves of the investigated fluoride-phosphate glasses. The solid red curve represents SIMPSON simulations of the REAPDOR curves for ^{31}P interacting with two ^{27}Al neighbors at a distance of 3.27 Å.

Figure 5-4 shows the ^{19}F MAS-NMR spectra of the 5PF6Sc and 10PF6Sc glasses. Four resonance lines are observed near −160, −130, −100 and −50 ppm. ^{19}F-MAS NMR spectral deconvolution parameters are detailed in Table 5-3. Comparison with our previous work in Sc-free 5FP and 10FP and with other analogous fluoride-phosphate glasses containing ScF_3, [23] indicate that the dominant resonance line near −130 pm can be assigned to fluorine atoms in an alkaline earth metal/aluminum rich environment, while the resonance line near −160 ppm and the component near −100 ppm can be assigned to Al-bound fluorine species and an alkaline-earth rich fluorine environment, respectively. The comparison with the chemical shift observed for the ScF_3 model compound, $\delta_{iso} = −36$ ppm, [39] and the work done by de Oliveira *et al.* [23] and by us suggest that the component near −50 ppm is assigned to F species bonded to Sc.
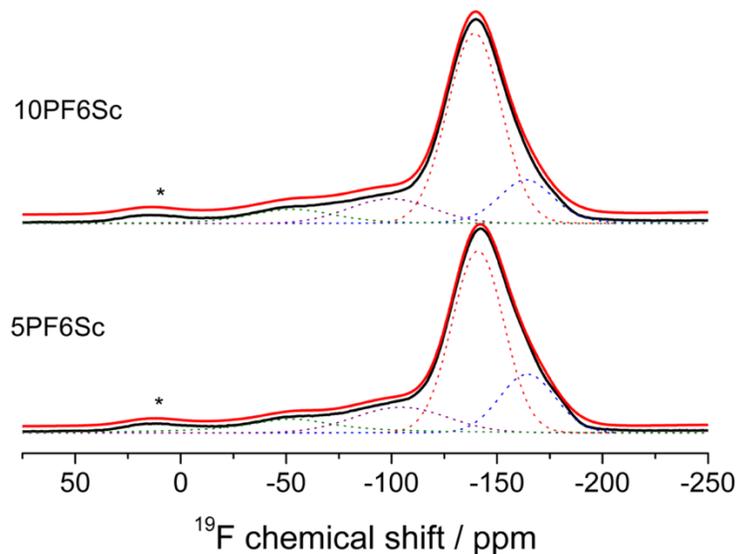
Figure 5-4. ^{19}F-MAS-NMR spectra of the 5PF6Sc and 10PF6Sc fluoride-phosphate glasses. Dashed colored curves denote the deconvolutions into individual Gaussian components. Black curves denote experimental data. Spinning sidebands are marked with asterisks.

Table 5-3. ^{19}F-MAS-NMR spectral deconvolution parameters isotropic chemical shifts (±0.5 ppm) and area contributions (± 1%) on the investigated 5PF6Sc and 10PF6Sc fluoride-phosphate glasses.

Sample	Sr/Al-F		Al-F		Sr-F		Sc-F	
	∂_{iso} (ppm)	Area (%)	∂_{iso} (ppm)	Area (%)	∂_{iso} (ppm)	Area (%)	∂_{iso} (ppm)	Area (%)
5PF6Sc	−140.9	57	−164.4	19	−104.4	14	−52.5	10
10PF6Sc	−139.2	63	−163.7	16	−99.5	13	−53.0	8

As mentioned above, Sc^{3+} ions have similar characteristics as the late RE ions, such as valence, ionic radius and electronegativity. These (I = $^7/_2$) nuclei have a 100% natural abundance, medium-sized magnetic moments and relaxation times on the order of magnitude of 1 s. In this structural study, the ^{45}Sc nuclei were used as diamagnetic mimics to probe the

ligand distribution around the rare-earth ions by measuring ^{45}Sc/^{31}P dipole-dipole interactions.

The ^{45}Sc MAS-NMR spectra for the 5PF6Sc and 10PF6Sc glasses (Figure 5-5) show a broad asymmetric lineshape, governed by a distribution of isotropic chemical shifts and second.order quadrupolar shifts, as typically observed for Sc- containing glasses.[23,45] The chemical shift indicates that the Sc species are six-coordinated and the Sc^{3+} ions are in a mixed phosphate/fluoride environment. De Oliveira *et al.* [23] have shown that Sc atoms, like aluminum, prefer ligation by phosphate rather than fluoride. Only in glasses with low P/F ratio a dominance of bonding to fluoride ions is possible. Based on the results shown above, the ^{45}Sc{^{31}P} REDOR experiment was used to provide information on the chemical environment of the RE ions.
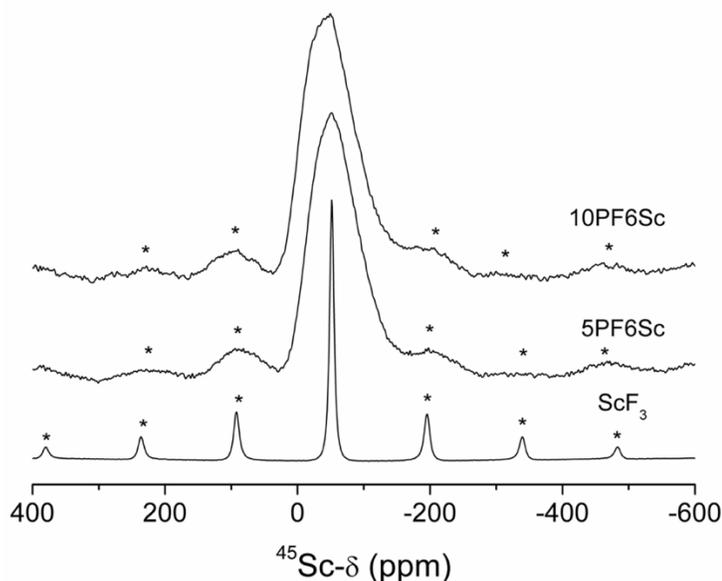
**Figure 5-5.** ^{45}Sc MAS-NMR spectra for the glasses 5PF6Sc and 10PF6Sc and crystalline ScF$_3$.

From the ^{45}Sc{^{31}P} REDOR results of the 5PF6Sc and 10PF6Sc glasses shown in Figure 5-6, the average number of P atoms (N_{Sc-O-P}) in the Sc-coordination could be deduced in the same fashion as explained earlier concerning the ligation of aluminum. $M_{2(Sc-P)}$ values

extracted from these REDOR curves were calibrated on parallel measurements of the model compound $ScPO_4$ for which all the internuclear $Sc\cdots P$ distances are well-known from the crystal structure.[46] In the present work the calibration factor was found to be 1.5, which was then used to correct the dipolar second moments obtained for the glasses from the parabolic analyses of the initial decay regime. We find that the $N_{Sc\text{-}O\text{-}P}$ values for the 5PF6Sc and 10PF6Sc glass compositions are 1.2 and 1.9, respectively. Assuming a Sc coordination number of six in the glasses, the average number of F atoms coordinated to Sc are $N_F = 4.8$ and 4.1 for 5PF6Sc and 10PF6Sc, respectively. The results show that the Sc^{3+} ions are predominantly linked to the fluorine atoms in these glasses and the $M_{2(Sc\text{-}P)}$ values are comparable to those obtained in other Sc-containing fluoride-phosphate glasses and are detailed in Table 5-4. [23]
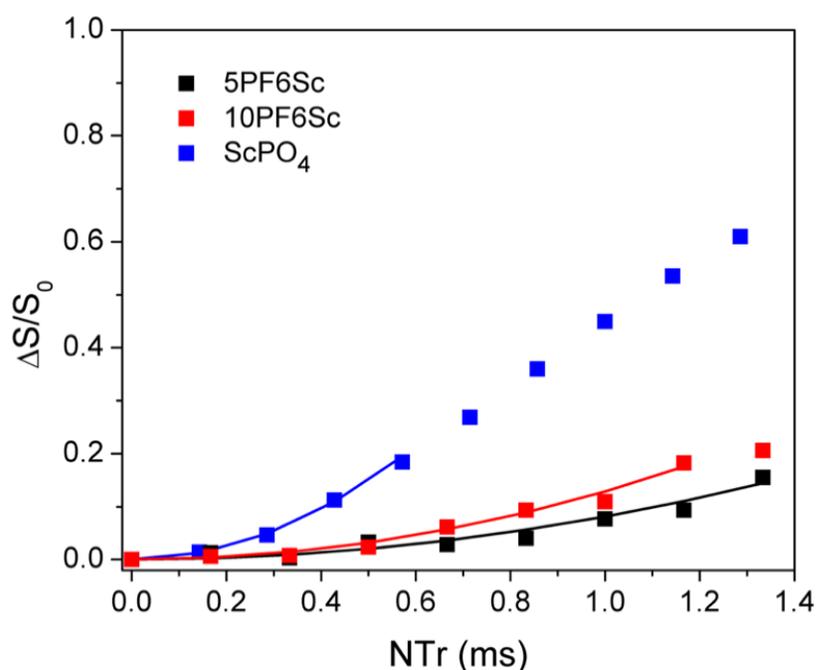
**Figure 5-6.** $^{45}Sc\{^{31}P\}$ REDOR dephasing curves of the 5PF6Sc and 10PF6Sc glasses. Squares represent experimental points obtained under MAS spinning speeds of 12.0 kHz Solid curves are parabolic fits to the data, analyzed within the data range $\Delta S/S_0 \leq 0.2$.

Table 5-4. Values of second moments $M_{2(P-Sc)}$ obtained from $^{45}Sc\{^{31}P\}$ REDOR experiments (corrected according to calibration with $ScPO_4$) and connectivity data on glasses. N_{Sc-O-P} and N_F are the numbers of phosphate and fluoride species in the Sc coordination environment derived respectively from the $M_{2(P-Sc)}$ values, considering that Sc is six-coordinated ($N_P + N_F = 6$).[53]

Glass Sample	$M_{2(P-Sc)}$ ($\times 10^6 rad^2 s^{-2}$)	N_{Sc-O-P}	N_F
5PF6Sc	0.91	1.2	4.8
10PF6Sc	1.44	1.9	4.1
ScPO$_4$[a]	6.6 (4.41)	-	-
Sc(PO$_3$)$_3$[b]	4.66	-	-

[a]van Vleck calculation based on crystallographic date from ref. [46]. Value in parenthesis gives the apparent value measured experimentally by analyzing $^{45}Sc\{^{31}P\}$ REDOR data via eq. (1), leading to the calibration factor of 1.5 [b] van Vleck calculation based on crystallographic data from ref. [53]

Absorption Spectroscopy: The absorption spectra in the range 180-1100 nm, obtained for the Tm^{3+}-Yb^{3+} co-doped (10PF0Gd) and Gd^{3+}-Tm^{3+}-Yb^{3+} triply-doped fluoride-phosphate glasses (10PF2Gd and 10PF4Gd) and (5PF2Gd) along with the host glasses (5PF and 10PF) as reference are shown in figure 5-7. The UV edge of fluoride-phosphate glasses containing 5-10 mol % phosphate was reported to be around 160 nm [13] and their cut-off edges are strongly influenced by extrinsic absorption from transition metal ion impurities present in the glasses, especially iron, which is the main trace impurity in fluoride/phosphate raw materials [12]. For the undoped glasses a small absorption peak at 220 nm is observed, which is due to Fe^{2+} impurities. Since the glasses were melted under reducing conditions (carbon crucible), it is known that they present better transmission in the UV due to the reduction of Fe^{3+} (absorption band at 250 nm and 185 nm) to Fe^{2+} (absorption band at 220 nm and 170 nm) with lower molar coefficient absorption $\varepsilon_{i\lambda}$ [47]. In the present samples, the lower purity of the rare-earth fluoride starting materials (GdF_3, YbF_3 and TmF_3) may be held responsible for shifting the UV edge to longer wavelengths.
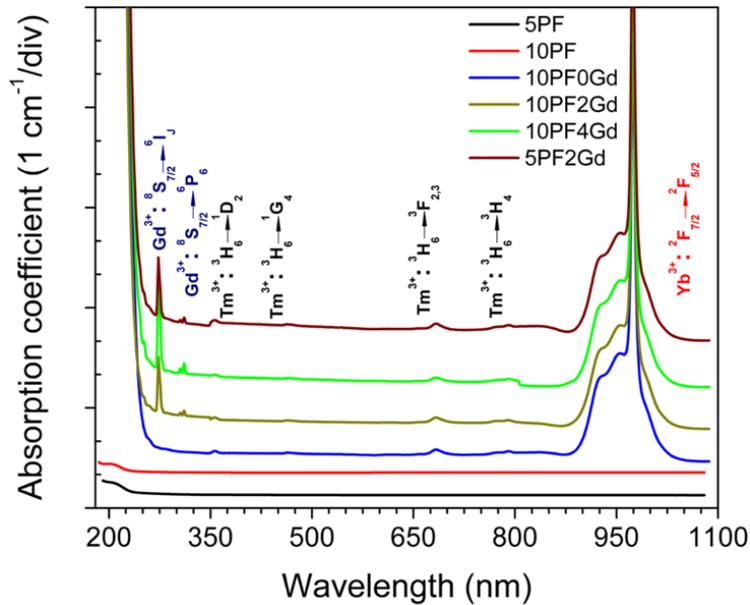
Figure 5-7. Absorption spectra obtained for the undoped and Gd^{3+}-Tm^{3+}-Yb^{3+} fluoride-phosphate glasses. Assignments of RE^{3+} absorption bands are shown in the figure. (The spectra have been vertically translated for better comparison).

For the co-doped glasses, the characteristic absorption bands of Gd^{3+} are observed at 275 and 312 nm in the UV region, assigned to the transitions from the ground state $^8S_{7/2}$ to the excited states ^6I_J and ^6P_J, respectively. The Tm^{3+} characteristic absorption bands are observed in the UV region at 355 nm and in the visible region at 465, 660, 685 and 785 nm, assigned to the transitions from the ground state $^3H_6$ to the excited states, $^1G_4$, $^3F_2$, $^3F_3$ and $^3H_4$, respectively. Finally, the absorption band observed at around 1000 nm is assigned to the transition from the Yb^{3+} ground state $^2F_{7/2}$ to the excited one $^2F_{5/2}$.

Gd^{3+}-Tm^{3+}-Yb^{3+} upconversion emission under 980 nm excitation: Figure 5-8 shows the representative upconversion emission spectrum in the range 275 – 700 nm under laser excitation at 980 nm (200 mW power) of the triply-doped fluoride phosphate glass sample 10PF4Gd. After the absorption of 980 nm excitation photons, Tm^{3+} emissions are observed in the UV and visible regions. In the visible region, characteristic blue (450 and 475 nm, process iv and iii, respectively) and red (650 nm, process iv) emissions from Tm^{3+}: $^1D_2 \rightarrow {}^3H_6$, $^1G_4 \rightarrow {}^3H_6$ and $^1G_4 \rightarrow {}^3F_4$ transitions, respectively, are observed. In the UV

106

region, a weak emission is observed at 290 nm due to the $^1I_6 \rightarrow {}^3H_6$ transition (process v) and a stronger one at 365 nm due to the $^1D_2 \rightarrow {}^3H_6$ transition (process iv) with a small shoulder at 347 nm due to the $^1I_6 \rightarrow {}^3F_4$ transition (process v). An aditional UC emission band at 310 nm is observed due to the Gd^{3+}: $^6P_{7/2} \rightarrow {}^8S_{7/2}$ transition (process v).[33,34]
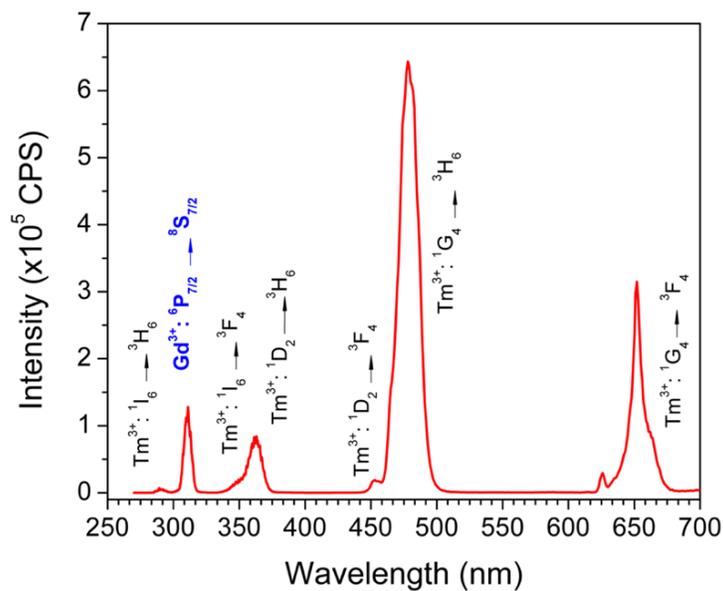

Figure 5-8. Upconversion emission spectrum under 200 mW 980 nm laser excitation for the representative glass sample 10PF4Gd. Assignments are shown in the figure.

The schematic energy level diagrams of Gd^{3+}, Tm^{3+} and Yb^{3+} ions with the possible upconversion processes involved in the UV-Vis conversion as discussed in [25,48] are illustrated in figure 5-9. Under 980 nm laser excitation, Yb^{3+} ions successively transfer energy to Tm^{3+} ions to populate the $^3H_5$, $^3F_3(^3F_2)$, $^1G_4$, $^1D_2$ and $^1I_6$ states. In turn, the Gd^{3+} $^6P_{7/2}$ state is populated by an energy transfer from Tm^{3+} ions. Because of the discrepancy of the energy levels, the dipole-dipole interaction has a non-resonant character and the energy transfer is non-radiative and has the participation of phonons [49], following these steps:

(i)   Upon 980 nm laser pumping, the Yb^{3+} ion is excited from the $^2F_{7/2}$ ground state to the $^2F_{5/2}$ excited one. The Yb^{3+} ion transfers its energy non-resonantly to Tm^{3+} ions in $^3H_6$ ground state exciting it to $^3H_5$ state, where the excess of energy ($\sim$1600 cm^{-1}) is dissipated by the highest phonon of fluoride-phosphate glass. The relatively short lifetime of

the $^3H_5$ state (and the small difference in energy) leads to a rapid population of the $^3F_4$ excited state of Tm^{3+} by multiphonon relaxation. [50]

(ii) The Tm^{3+} ions are subsequently excited by a resonant energy transfer from the excited Yb^{3+} ion to the Tm^{3+} ion in the intermediate $^3F_4$ state to the $^3F_2$ state, as a result of a rapid multiphonon relaxation (second energy transfer). Thus, the Tm^{3+} ions relaxes non-radiatively to the $^3H_4$ state, where the radiative emission $^3H_4 \rightarrow {}^3H_6$ (800 nm) occurs.

(iii) After this process, analogically, another excited Yb^{3+} ion can transfer its energy non-resonantly to the Tm^{3+} ion in the $^3H_4$ intermediate state exciting it to the $^1G_4$ state (third energy transfer). The energy excess ($\sim$ 1800 cm^{-1}) is dissipated by the fluoride-phosphate glass lattice vibrations, where the $^1G_4 \rightarrow {}^3F_4$ (650 nm) and $^1G_4 \rightarrow {}^3H_6$ (475 nm) radiative transitions can occurs, as a result of the three-photon process of excitation conversion.

(iv) A fourth energy transfer populates the $^1D_2$ excited state of Tm^{3+} via a non-resonant energy transfer from a Yb^{3+} ion to a Tm^{3+} ion in the $^1G_4$ level. Alternatively, the $^1D_2$ state may be populated through a cross relaxation process $^3F_3 \rightarrow {}^3H_6$: $^3F_3 \rightarrow {}^1D_2$. This process leads to the radiative transitions, $^1D_2 \rightarrow {}^3H_6$ (361 nm) and $^1D_2 \rightarrow {}^3F4$ (450 nm) in the ultraviolet and visible regions, respectively.

(v) After the $^1D_2$ was populated, $^3P_{2,1}$ states are excited by the fifth energy transfer from the Yb^{3+} ion to a Tm^{3+}. The $^3P_2$ state non-radiatively decay to the $^1I_6$ state of Tm^{3+} and the UV radiative transitions, $^1I_6 \rightarrow {}^3H_6$ (290 nm) and $^1I_6 \rightarrow {}^3F_4$ (347 nm) occurs. Alternatively, the Tm^{3+} in the $^3P_2$ state can radiatively decay to the $^3H_6$ ground state emitting at 310 nm, but such transition does not occurs in our system, as showed below in figure 5-8, alternatively, the energy is transferred to ^6I_j state of Gd^{3+} ions through the ET $^3P_3 \rightarrow {}^3H_6$ (Tm^{3+}):$^8S_{7/2} \rightarrow {}^6I_j$ (Gd^{3+}). The non-radiative relaxation from the $^6I_{7/2}$ to the $^6P_{5/2}$ states of Gd^{3+} results in the radiative transition $^6P_{7/2} \rightarrow {}^8S_{7/2}$ (310 nm) observed in our glasses. Because of the large energy gap between the $^8S_{7/2}$ ground state and the $^6P_{7/2}$ first excited state, the Gd^{3+} ion cannot absorb 980 nm photons directly.
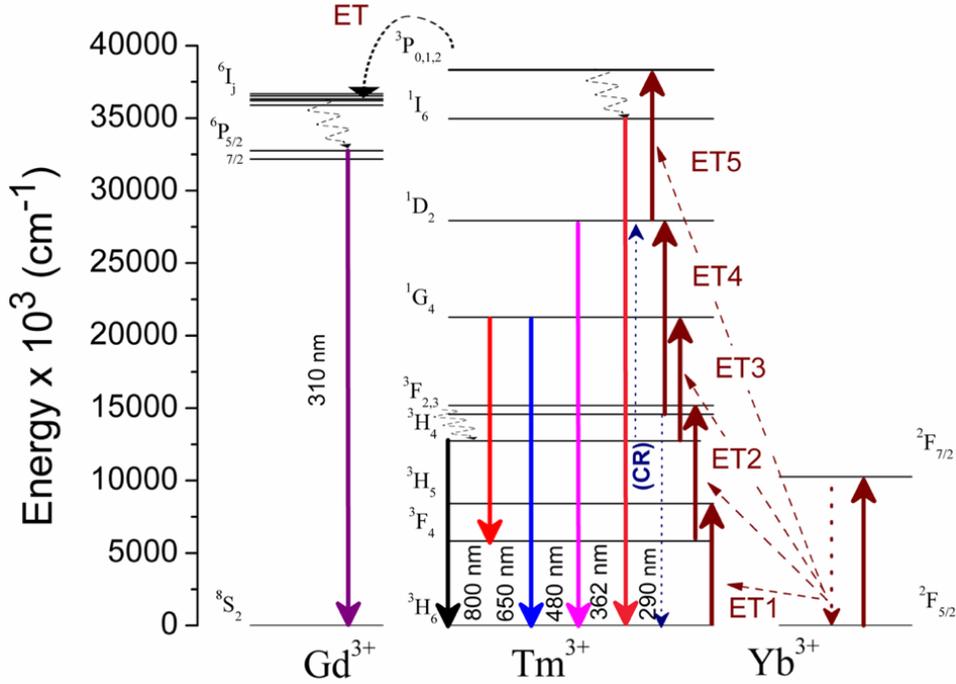
Figure 5-9. Energy level diagrams of Gd^{3+}, Tm^{3+} and Yb^{3+} ions with the possible upconversion process adapted from Ref. [47]. CR cross-relaxation; ET energy transfer

The 310 nm UC emission band under 980 nm excitation could be also resulting from the Tm^{3+}: $^3P_2 \rightarrow {}^3F_4$ transition as it has been previously observed in low phonon hosts like $NaYF_4$ microcrystals co-doped with Tm^{3+}-Yb^{3+} [51]. To verify and clarify the origin of this emission, the effect of Gd^{3+} content in the glasses was studied and compared with a sample without Gd^{3+} (10PF0Gd) (figure 5-10a). Spectra have been normalized to 290 nm band related to the Tm^{3+}:$^1I_6 \rightarrow {}^3H_6$ transition.

We can clearly see that the emission at 310 nm only occurs in the triply-doped samples (10PF2Gd and 10PF4Gd), confirming its origin from the $^6P_{7/2}$ excited state of Gd^{3+} ions. The fact is that the higher vibrational wavenumber found in fluoride-phosphate glasses, $\sim$1100 cm^{-1}, which is attributed to the $Q^{(1)}$ phosphate species, compared to that of the $NaYF_4$ microcrystals, increases the non-radiative transition probabilities $^3P_2 \rightarrow {}^3P_1 \rightarrow {}^3P_0 \rightarrow {}^1I_6$ [52]. The radiative transitions from the $^3P_2$ level are thus unlikely to occur due to its proximity with these states [51]. Nonetheless, to the best of our knowledge, this is the first report of such

emission at 310 nm upon 980 nm excitation in a glassy material. A ~10-fold relative enhancement is observed as we increase the Gd^{3+} content from 2 to 4 mol%.
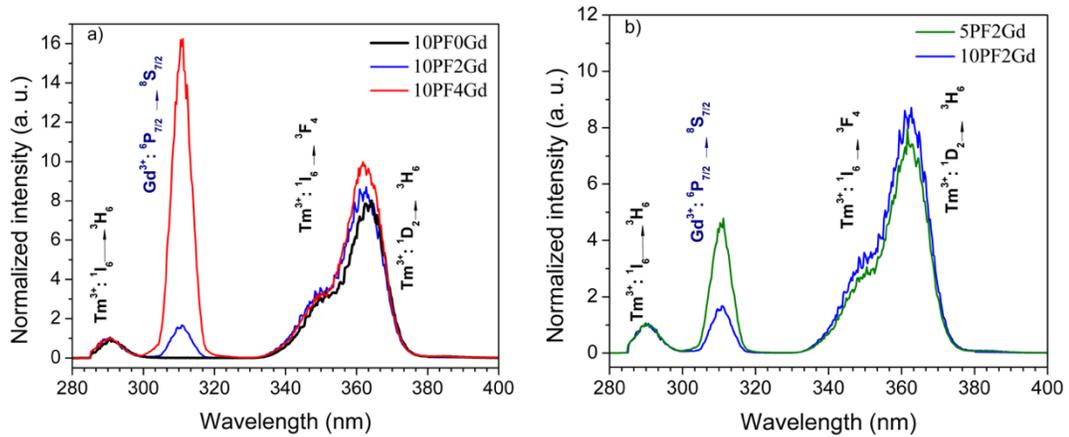

Figure 5-10. Ultraviolet upconversion spectra under 400mW 980 nm laser excitation of the fluoride-phosphate glass samples as a function of: (a) the Gd^{3+} content and (b) the fluoride/phosphate ratio. Spectra are normalized by the $Tm^{3+} : {}^1I_6 \rightarrow {}^3H_6$ (290 nm) band intensity. Assignments are shown in the figure.

The effect of the fluoride/phosphate ratio on the 310 nm Gd^{3+} upconverted emission is shown in figure 5-10b. It reveals a relative enhancement of Gd^{3+} emission intensity when the fluoride/phosphate ratio is larger (5PF2Gd glass sample). Since the local environment of the rare-earth ions is characterized by a mixture of fluoride and phosphate ligands, and the average quantitative local ligand distribution (phosphate versus fluoride) of the RE evolves with composition in the expected manner, the phonon-assisted energy transfer between Yb^{3+} and Tm^{3+} ions that leads to the population of the ${}^3P_{0,1,2}$, ${}^1I_6$ and ${}^1D_2$ states and consecutively the population of the ${}^6I_j$ states of the Gd^{3+} ions through an energy transfer from the Tm^{3+} ions [33,34] is more favorable for the sample with a higher fraction of fluoride ligands around the RE ions, (i..e. sample 5PF2Gd). The relative enhancement on the Gd^{3+} emission intensity indicates the importance of populating efficiently the $Tm^{3+}:{}^3P_j$ state in order to obtain intense UV UC emission at 310 nm.

To better understand the mechanism(s) proposed in Figure 5-9 in the population of the upper emitting states and the number of photons involved in populating the Tm^{3+} ${}^1D_2$ and ${}^1I_6$ states and the Gd^{3+} ${}^6P_{7/2}$ state, which leads to the UV upconverted emissions, we have

studied the dependence of the upconverted emission intensity on the 980 nm pump power from 100 to 250 mW for the representative sample 10P90F:2Gd^{3+}:0.1Tm^{3+}:4Yb^{3+} (figure 5-11a). The number of photons (n) required to populate the emitting state from an unsatured process can be determined from the slope of the plot of log(emission intensity) versus log(power pump) following the relation $I_{up} \propto P^n$, where the upconverted luminescence intensity is proportional to the nth of the low frequency power (P) [2].

The fitted slopes are shown in figure 5-11b and were determined to be four and five, indicating four photons upconversion process for the 362 nm emission and five photons upconversion process for 310 nm and 290 nm emission, similar to other works reported in the literature in fluoride crystals and nanoparticles triply-doped with Gd^{3+}-Tm^{3+}-Yb^{3+} ions [25,30,33,34,48] and in agreement with the schematic energy transfer process described above (figure 5-9).
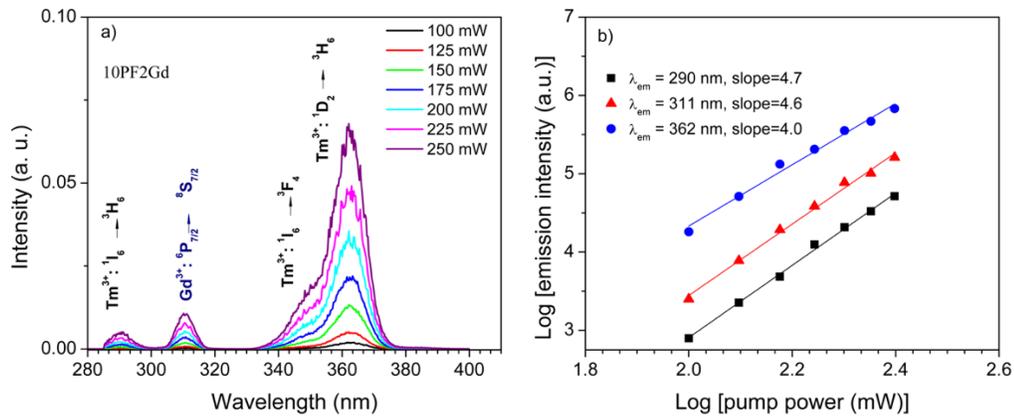

Figure 5-11. (a) Power dependence and (b) Log-log plot of the UV UC emissions at 290, 310 and 360 nm excited by 980 nm laser for the representative sample 10PF2Gd.

5.4. Conclusion

Near infrared to ultraviolet upconversion emission has been studied in triply-doped Gd^{3+}-Tm^{3+}-Yb^{3+} high purity fluoride-phosphate glasses. The emission intensity *vs* laser excitation power study suggests that the UV emissions at 362, 310 and 290 nm come from a five-photon, four-photon and three-photon upconversion processes, respectively. The emission of the Gd^{3+} ion upon 980 nm excitation is reported for the first time in glasses.

Using scandium as a diamagnetic mimic for the luminescent rare-earth species Tm^{3+} and Yb^{3+} with similar ionic radius, the ligand distribution surrounding the rare-earth ions could be quantified by $^{45}Sc/^{31}P$ rotational echo double resonance NMR. The rare-earth ions are found in a mixed fluoride / phosphate ligand environment, which evolves with fluoride/phosphate batch ratio in the expected manner. High F/PO_4^{3-} ratios favor high Gd^{3+} emission intensities. The network structure is characterized by Al-O-P linkages and the fluoride ions are found in a mixed Al/Ca/Sr/Mg environment. These results indicate that high-purity fluoride-phosphate glasses constitute a promising alternative to the existing nanocrystals and glass-ceramics for the development of solid-state and/or fiber UV photonic components and devices. The production of nanocrystals is expensive and not suitable for large scale manufacturing. On the other hand, glassy materials are easy to fabricate and to be obtained in various shapes and sizes and also as optical fibers.

Acknowledgments

References

[1]   D. Birtalan, W. Nunley, *Optoelectronics: Infrared-Visable-Ultraviolet Devices and Applications, Second Edition*, CRC Press, **2009**.

[2]   F. Auzel, *Chem. Rev.* **2004**, *104*, 139.

[3]   G. S. He, P. P. Markowicz, T.-C. Lin, P. N. Prasad, *Nature* **2002**, *415*, 767.

[4]   C. W. Thiel, T. Böttger, R. L. Cone, *J. Lumin.* **2011**, *131*, 353.

[5]   A. J. Kenyon, *Prog. Quantum Electron.* **2002**, *26*, 225.

[6]   J. Li, X. Wang, H. Yang, Z. Jiang, *Phys. B Condens. Matter* **2007**, *392*, 251.

[7]   F. Gan, J. Wang, Y. Chen, *J. Non. Cryst. Solids* **1997**, *213–214*, 261.

[8]   A. Kumar Singh, S. B. Rai, A. Rai, *Prog. Cryst. Growth Charact. Mater.* **2006**, *52*, 99.

[9]   D. CHEN, Y. WANG, Y. YU, F. LIU, P. HUANG, *J. Rare Earths* **2008**, *26*, 428.

[10]   G. Y. Chen, C. H. Yang, B. Aghahadi, H. J. Liang, Y. Liu, L. Li, Z. G. Zhang, *J. Opt. Soc. Am. B* **2010**, *27*, 1158.

[11]   C. L. Sun, J. F. Li, C. H. Hu, H. M. Jiang, Z. K. Jiang, *Eur. Phys. J. D* **2006**, *39*, 303.

[12]   D. Ehrt, *Phys. Chem. Glas. Eur. J. Glas. Sci. Technol. Part B* **2015**, *56*, 217.

[13]   D. Ehrt, P. Ebeling, U. Natura, *J. Non. Cryst. Solids* **2000**, *263–264*, 240.

[14]   D. Möncke, D. Ehrt, L. L. Velli, C. P. E. Varsamis, E. I. Kamitsos, *Phys. Chem. Glas. J. Glas. Sci. Technol. Part B* **2005**, *46*, 67.

[15]   G. Galleani, Y. Ledemi, E. S. de Lima Filho, S. Morency, G. Delaizir, S. Chenu, J. R. Duclere, Y. Messaddeq, *Opt. Mater. (Amst).* **2017**, *64*, 524.

[16]   C. A. G. Kalnins, H. E. Heidepriem, A. Dowler, T. M. Monro, in *2011 Int. Quantum Electron. Conf. Conf. Lasers Electro-Optics Pacific Rim Inc. Australas. Conf. Opt. Lasers Spectrosc. Aust. Conf. Opt. Fibre Technol.*, IEEE, **2011**, pp. 2051–2053.

[17]   X. Zou, K. Itoh, H. Toratani, *J. Non. Cryst. Solids* **1997**, *215*, 11.

[18]   T. V. Bocharova, A. M. Mironov, G. O. Karapetyan, *Inorg. Mater.* **2005**, *41*, 892.

[19]   M. de Oliveira, T. Uesbeck, T. S. Gonçalves, C. J. Magon, P. S. Pizani, A. S. S. de Camargo, H. Eckert, *J. Phys. Chem. C* **2015**, *119*, 24574.

[20]   T. S. Gonçalves, R. J. Moreira Silva, M. de Oliveira Junior, C. R. Ferrari, G. Y. Poirier, H. Eckert, A. S. S. de Camargo, *Mater. Chem. Phys.* **2015**, *157*, 45.

[21]   S. Tanabe, K. Hirao, N. Soga, *J. Non. Cryst. Solids* **1992**, *142*, 148.

[22]   P. Babu, K. H. Jang, E. S. Kim, R. Vijaya, C. K. Jayasankar, V. Lavín, H. J. Seo, *J. Non. Cryst. Solids* **2011**, *357*, 2139.

[23]   M. de Oliveira, T. S. Gonçalves, C. Ferrari, C. J. Magon, P. S. Pizani, A. S. S. de Camargo, H. Eckert, *J. Phys. Chem. C* **2017**, *121*, 2968.

[24]   M. Pokhrel, C. Valdes, Y. Mao, *Opt. Mater. (Amst).* **2016**, *58*, 67.

[25]   T. Jiang, Y. Liu, S. Liu, N. Liu, W. Qin, *J. Colloid Interface Sci.* **2012**, *377*, 81.

[26] K. Zheng, W. Qin, G. Wang, G. Wei, D. Zhang, L. Wang, R. Kim, N. Liu, F. Ding, X. Xue, T. Jiang, R. Yang, *J. Nanosci. Nanotechnol.* **2010**, *10*, 1920.

[27] C. Cao, W. Qin, J. Zhang, *Opt. Commun.* **2010**, *283*, 547.

[28] B. Zhou, L. Tao, W. Jin, Y. H. Tsang, *IEEE Photonics Technol. Lett.* **2012**, *24*, 1726.

[29] F. Güell, R. Solé, J. Gavaldà, M. Aguiló, M. Galán, F. Díaz, J. Massons, *Opt. Mater. (Amst).* **2007**, *30*, 222.

[30] F. Pandozzi, F. Vetrone, J.-C. Boyer, R. Naccache, J. A. Capobianco, A. Speghini, M. Bettinelli, *J. Phys. Chem. B* **2005**, *109*, 17400.

[31] C. He, D. Zhao, G. Qin, K. Zheng, W. Qin, *J. Nanosci. Nanotechnol.* **2011**, *11*, 9494.

[32] C. He, G. Qin, D. Zhao, X. Chuai, L. Wang, K. Zheng, W. Qin, *J. Nanosci. Nanotechnol.* **2014**, *14*, 3831.

[33] C. Cao, W. Qin, J. Zhang, Y. Wang, P. Zhu, G. Wei, G. Wang, R. Kim, L. Wang, *Opt. Lett.* **2008**, *33*, 857.

[34] W. Qin, C. Cao, L. Wang, J. Zhang, D. Zhang, K. Zheng, Y. Wang, G. Wei, G. Wang, P. Zhu, R. Kim, *Opt. Lett.* **2008**, *33*, 2167.

[35] K. Zheng, W. Qin, C. Cao, D. Zhao, L. Wang, *J. Phys. Chem. Lett.* **2015**, *6*, 556.

[36] X. Chen, Z. Song, Y. Wang, J. Xiong, G. Yang, S. Li, J. Zhou, F. Peng, G. Zhou, in *Inf. Opt. Photonics Technol. Ii* (Eds.: G. Mu, F. Song, F.T.S. Yu, S. Jutamulia), **2007**, p. 68370U.

[37] I. R. Martín, V. D. Rodríguez, V. Lavín, U. R. Rodríguez-Mendoza, *Spectrochim. Acta Part A Mol. Biomol. Spectrosc.* **1999**, *55*, 941.

[38] Y. Messaddeq, S. Inoue, C. T. M. Ribeiro, L. A. O. Nunes, *J. Non. Cryst. Solids* **1997**, *213*, 179.

[39] A. Y. H. Lo, V. Sudarsan, S. Sivakumar, F. van Veggel, R. W. Schurko, *J. Am. Chem. Soc.* **2007**, *129*, 4687.

[40] M. Bertmer, H. Eckert, *Solid State Nucl. Magn. Reson.* **1999**, *15*, 139.

[41] T. Gullion, *Chem. Phys. Lett.* **1995**, *246*, 325.

[42] M. Bak, J. T. Rasmussen, N. C. Nielsen, *J. Magn. Reson.* **2000**, *147*, 296.

[43] J. C. . Chan, H. Eckert, *J. Non. Cryst. Solids* **2001**, *284*, 16.

[44] G. Galleani, S. H. Santagneli, Y. Messaddeq, M. de Oliveira, H. Eckert, *Phys. Chem. Chem. Phys.* **2017**, *19*, 21612.

[45] D. Mohr, A. S. S. de Camargo, C. C. de Araujo, H. Eckert, *J. Mater. Chem.* **2007**, *17*, 3733.

[46] R. C. L. Mooney, *Acta Crystallogr.* **1956**, *9*, 677.

[47] D. Ehrt, M. Carl, T. Kittel, M. Müller, W. Seeber, *J. Non. Cryst. Solids* **1994**, *177*, 405.

[48] M. Pokhrel, C. Valdes, Y. Mao, *Opt. Mater. (Amst).* **2016**, *58*, 67.

[49] M. Kochanowicz, D. Dorosz, J. Zmojda, J. Dorosz, P. Miluski, *J. Lumin.* **2014**, *151*, 155.

[50] G. Özen, A. Kermaoui, J. P. Denis, X. Wu, F. Pelle, B. Blanzat, *J. Lumin.* **1995**, *63*, 85.

[51] G. Wang, W. Qin, L. Wang, G. Wei, P. Zhu, R. Kim, *Opt. Express* **2008**, *16*, 11907.

[52] W. T. Carnall, P. R. Fields, B. G. Wybourne, *J. Chem. Phys.* **1965**, *42*, 3797.

[53] Y. I. Smolin, Y. F. Shepelev, A. I. Domanskij, N. V. Belov, *Kristallografiya* **1978**, *23*, 187.

6. GENERAL CONCLUSION

The main goal of this Ph. D. research was to exploit the fluoride-phosphate properties in order to fabricate highly transparent optical fibers in the deep-ultraviolet and also to explore the structural and optical properties of the FP glasses for photonic applications.

Initially, FP glasses in the system 10 mol % $Ba(PO_3)_2$ and 90 mol % (AlF_3-CaF_2-SrF_2-MgF_2) have been prepared and showed to be suitable for fiber drawing thank to their excellent thermal stability against crystallization (> 100 ∘C). They also showed excellent optical transmittance when prepared from high-purity eagents, being transparent down to 180 nm in the DUV (75% for a 2 mm bulk sample). Core-cladding preforms where then produced by a modified build-in casting technique, preparing, separately, a tube for the clad, substituting the barium phosphate by strontium phosphate to decrease the refractive index and guarantee the guiding in the fiber by total internal reflection, and a rod for the core. Then the rod was inserted manually inside the tube and the fiber was then successfully fabricated from the as-prepared preforms through a fused silica crucible assembly. This alternative has shown to be suitable to overcome the superficial crystallization issues obtained during the preform method trials. An optical attenuation of 63 dB/m and 20-42 dB/m was measured on the produced step-index fibers at 244 nm and in the range 407-1750 nm, respectively. For the single-index fiber, the optical losses in the range 407-1750 nm are 0.7-5 dB/m. It is worth to mention that FP glass fibers fabricated by the crucible method were reported for the first time in the literature and constitutes a new route to address the challenges behind the complex fabrication of FP glass fibers and other glasses that suffer from superficial crystallization issues.

In the following step of the Ph. D. research, we have investigated the structural properties of a series of FP glasses with different F/P ratio to understand the structural evolution of these glasses, the origin of their thermal stability for fiber drawing and we also doped the glasses with RE ions to do a correlation between the structural and luminescence properties, important for photonic applications. We were able to provide a quantitative insight into the network organization by Raman and NMR techniques, and also the rare-earth coordination in these glasses as a function of the F/P ratio. The data suggest that as we decrease the F/P ratio, the network structure of these glasses is dominated by the formation

of Al-O-P linkages, which could also be quantified and the contribution of different $Q^{(n)}$ units. The glasses with higher F/P ratio are dominated by $Q^{(0)}$ species and the near-absence of P-O-P connectivity. As we decrease the F/P ratio both $Q^{(1)}$ and $Q^{(2)}$ units are present and dominant. The fluoride ions are found in a mixed Al/Ca/Sr/Mg environment and the local environment of the RE ions is characterized by a mixed fluoride/phosphate ligation, being quantified by EPR and optical spectroscopy. Some P-RE ligation remains even at the highest fluoride content in these glasses. The origin of their thermal stability, making these glasses suitable for fiber drawing, comes to the fact that this increase in connectivity by means of P-O-Al and P-O-P linkages, increases their thermal stability against crystallization, important for fiber drawing. Their high transparency in the DUV, comes from the high content of fluoride ions in a mixed alkaline earth environment, known to be highly transparent in this region due to their wide bandgap.

Finally, regarding the excellent luminescent properties found for the FP glasses with low phosphate content, we have prepared highly-pure fluoride-phosphate glasses co-doped with Gd^{3+}-Tm^{3+}-Yb^{3+}. First, using scandium as a diamagnetic mimic for the luminescent rare-earth species (Tm^{3+} and Yb^{3+}) with similar ionic radius, the ligand distribution surrounding the rare-earth ions has been quantified by $^{45}Sc/^{31}P$ rotational echo double resonance technique together with structural insights by means of other NMR techniques. The rare-earth ions have been found in a mixed fluoride/phosphate environment with a dominant fluoride ligation for these glasses and high F content. Second we have show upconverted emissions in UV region under 980 nm excitation from Tm^{3+} and Gd^{3+} ions for these glasses. The energy transfer mechanism between Gd^{3+}, Tm^{3+} and Yb^{3+} ions have been also proposed and suggests that UV emissions in 362, 310 and 290 nm may come from a five-photon, four-photon and three-photon energy transfer upconversion process, respectively. Emission of Gd^{3+} ion upon 980 nm excitation was observed for the first time in glasses. Highest average number of F atoms coordinate to rare-earth atoms are correlated with a more intense Gd^{3+} emission. The high transparency of these glasses also contributed to the high intense UV emissions observed.

RESUMO EXPANDIDO DA TESE EM PORTUGUÊS.

Esta seção apresenta resumidamente os principais resultados desta tese de doutoramento divido por cada um dos tres trabalhos publicados

Os vidros mistos fluoreto-fosfato com baixas quantidades de impurezas, são materiais altamente transparentes na região do UV-profundo e vácuo, oferecendo assim uma alternativa frente as fibras de silica utilizadas hoje. Estes vidros são produzidos pela mistura de fluoretos e polifosfatos com propriedades combinadas de ambos como, excelente capacidade de formação vítrea, baixo índice de refração e ampla janela de transmissão ($\sim$ 160 a 4000 nm), porem poucos trabalhos relatam a fabricação e a consequente perdas no UV de fibras opticas a partir destes. A única fibra de transmissão UV bem estabelecida existente até o momento consiste em fibras núcleo-casca de vidro de sílica dopado com OH/flúor. No entanto, a utilização de tais fibras é limitada pelo efeito de solarização que degrada a transmissão da luz UV após exposição prolongada.

O desenvolvimento de novas fibras ópticas capazes de operar na região do ultravioleta profundo (200-300 nm) e de vácuo (120-200 nm) beneficiariam aplicações em tecnologias a laser, técnicas de microlitografia (maior resolução espacial) e principalmente a detecção química elementar (detecção de fósforo e enxofre na agricultura), principal motivação deste trabalho. Além disso, os vidros mistos fluoreto-fosfato, quando dopados com íons terras-raras trivalentes, o ambiente de baixa energia de fônon dos fluoretos é favorável para emissões com alta eficiência quântica dos TRs, tornando-os então adequados para outras aplicações na área da fotônica também na forma de fibra e/ou bulk.

Portanto, no primeiro trabalho, intitulado como "*Fibra óptica de índice-degrau transmissora de luz UV a base de vidro fluorofosfato fabricada pela técnica do cadinho*", amostras no sistema vítreo $10Sr(PO_3)_2$-$90(AlF_3–CaF_2–SrF_2–MgF_2)$ e $xBa(PO_3)_2$-100-$x(AlF_3–CaF_2–SrF_2–MgF_2)$, com x = 5, 10 e 20 foram preparadas pelo método convencional de fusão-choque térmico a partir de reagentes de alta pureza ($\geq$5N) em ambiente redutor (cadinho de carbono vítreo). Os precursores, $Sr(PO_3)_2$ e $Ba(PO_3)_2$ de alta pureza foram preparados a partir da reação no estado sólido, partir do $NH_4H_2PO_4$ com o MCO_3.

As temperaturas características, assim como a janela de transmissão dos vidros foram determinadas em seguida. A Tg dos vidros aumentou de 439°C para 460°C com o aumento da quantidade de fosfato enquanto que um alargamento do pico de cristalização foi observado. O vidro com 10 mol% de fosfato de bário e 90 mol% fluoretos, com maior estabilidade térmica em comparação ao vidro com 5 mol% de fosfato e 95 mol% fluoretos, foi escolhido para a fabricação da fibra e $Ba(PO_3)_2$ foi substituído por $Sr(PO_3)_2$ na composição para diminuir o seu índice de refração em vista da preparação da preforma de índice degrau.

A transmissão na região UV (figura 1) para os vidros atinge 90% acima de 240 nm e é quase 75% a 180 nm. A 220 nm, observa-se uma pequena banda de absorção, que é devido à absorção de impurezas Fe^{2+}. Na região IV, a transmissão atinge 91% e se estende até 4000 nm. A banda de absorção em torno de 3000 nm é atribuído ao alongamento O-H. A borda de absorção IV a 4500 nm é devido à vibração P-O.
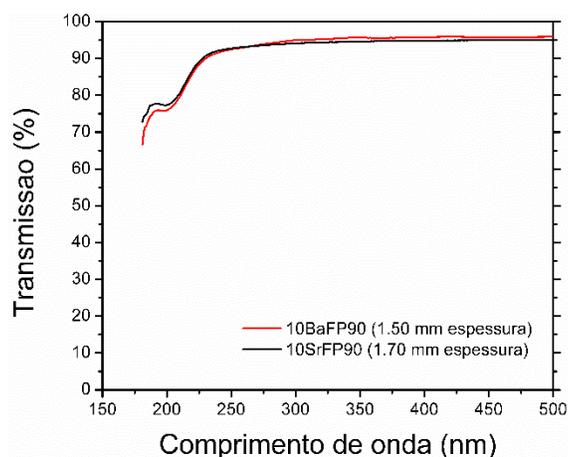

Figura 1. Espectro de transmissão na região do UV profundo para os vidros do núcleo e da casca, respectivamente.

Para preparação das fibras ópticas núcleo-casca, um método alternativo foi utilizado. Este método consiste em duas etapas: (i) preparação das preformas núcleo-casca pelo método "building-in casting" e (ii) puxamento das fibras a partir das preformas preparadas a partir de um cadinho de sílica. Primeiramente, um tubo cilíndrico de vidro com a composição da casca $[10Sr(PO_3)_2-90(AlF_3-CaF_2-MgF_2-SrF_2)]$ foi preparado e então um tarugo com a

composição da casca [10Ba(PO$_3$)$_2$-90(AlF$_3$-CaF$_2$-MgF$_2$-SrF$_2$)] foi preparado separadamente em seguida. Apos a etapa de fusão, os vidros foram refundidos sob vácuo a 730ºC durante 1 hora e vertidos em um molde de latão cilíndrico pré-aquecido à temperatura de transição vítrea e recozidos à mesma temperatura durante 6 horas. Para produzir os tarugos de vidro para o núcleo da preforma, utilizou-se um molde cilíndrico de 5 mm de diâmetro interno. Para produzir o tubo de vidro para a casca das preformas, (i) o vidro é vertido no molde pré-aquecido de 10 mm de diâmetro interno e quando em contato com as paredes do molde começa a se solidificar; (ii) é aberto um "obturador" colocado abaixo do molde, permitindo que a parte do vidro que ainda é líquido (centro) escoe, formando-se um tubo de vidro e; (iii) o mesmo obturador é fechado uma vez que o tubo se solidificou com o diâmetro e o comprimento desejados.

Em seguida, para produzir as fibras, o tarugo de vidro foi inserido manualmente no tubo de vidro e a preforma núcleo-casca, foi então colocada em um cadinho de sílica fundida. A montagem foi colocada no forno da torre de fibra óptica, a uma temperatura de 643ºC (Tg + 193°C) e o processo de puxamento da fibra foi iniciado. Uma fibra de índice único revestida com polímero curado por UV de baixo índice de refração também foi produzida pelo mesmo método, a partir de um tarugo com a composição do núcleo.

A etapa de pré fusão dos vidros sob vácuo, conforme descrito acima, se deu devido a observação da liberação de gás seguida pela formação de bolhas nas primeiras tentativas de puxamento das fibras, causando muitas imperfeições. O passo de pré fusão permitiu diminuir a quantidade de gás dissolvido na massa fundida, melhorando a qualidade da fibra obtida. Apos esta etapa a preforma que consiste em um tubo com a composição da casca e um tarugo com a composição do núcleo foi obtida.

O regime de temperatura de puxamento foi determinado ser na faixa de temperatura de viscosidade a partir de 10^2 - 10^3 P (para o método do cadinho) até 10$^{5.5}$-10^6 P (para o método de puxamento a partir de uma preforma) (figura 2). As temperaturas para puxamento da fibra estão no intervalo de 598-545°C (casca) e 585-540°C (núcleo). A faixa de temperatura para o puxamento da fibra é muito próxima a temperatura de inicio da cristalização para o núcleo e a casca, 597°C e 599°C, respectivamente. Portanto, velocidade alta de puxamento é necessária e uma pequena zona quente no forno onde a preforma fica exposta é necessária

para diminuir o tempo que o vidro fica exposto ao calor para reduzir o crescimento cristalino e aumentar a qualidade da fibra.
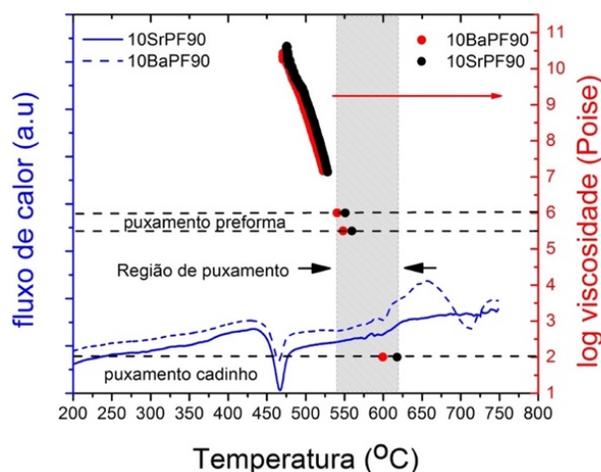

Figura 2. Curvas DSC e viscosidade medida pelo método de pratos paralelos em função da temperatura para os vidros de composição do núcleo (10BaPF90, linha preta) e casca (10SrPF90, linha vermelha). A taxa de aquecimento foi 10K/min para a analise térmica e 2K/min para as medidas de viscosidade.

Do ponto de vista experimental, a primeira metodologia explorada para produzir fibras de fluorofosfato foi simplesmente puxando uma preforma núcleo-casca pelo método convencional. No entanto, sérios problemas de cristalização na superfície da fibra durante o processo de puxamento foram enfrentados. E então um método alternativo foi utilizado.

Este método consistiu em preparar uma preforma núcleo-casca e puxa-la através de um cadinho de sílica fundida. A preforma núcleo-casca foi assim inserida no cadinho de sílica fundida e aquecido a 643°C. A fibra foi então retirada rapidamente da saída dos bocais no fundo do cadinho de sílica. Nenhum vestígio de cristalização foi observado. O diâmetro externo (casca) e interno (núcleo) da fibra obtida foram de 127 μm e 68 μm, respectivamente. As fibras de índice único de mesmo diâmetro feitas a partir do vidro 10BaPF90 também foram produzidas pela mesma técnica.

Para a fibra de índice degrau, a atenuação obtida a 244 nm foi de 63 dB/m (figura 3).
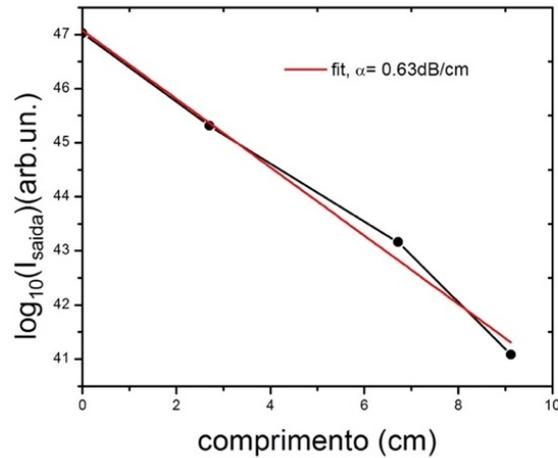
Figura 3. Potência na saída da fibra a 244 nm em função do comprimento adicional de fibra. Em vermelho: melhor ajuste linear da atenuação.

Uma segunda seção da fibra foi utilizaa para a medida de atenuação na região 350-1750 nm (figura 4). Para comparação, a mesma medida foi realizada na fibra de índice único. As perdas diminuem de 42 a 20 dB /m no intervalo 407-1750 nm. A 350 nm, um aumento abrupto nas perdas foi observado, possivelmente devido a presença de impurezas de metais de transição. Para a fibra de índice único, comportamento similar foi observado, porem as perdas são de aproximadamente uma ordem de magnitude menores, de 5 dB /m para um mínimo de ~0.7 dB/m. As altas perdas medidas na fibra núcleo-casca comparadas a fibra de índice único são provavelmente devido a perdas extrínsecas causadas por imperfeições na interface núcleo/casca e do contato da preforma com as paredes do cadinho de sílica. A presença de estrias no núcleo foi observada, causando também perdas extrínsecas. A presença de bolhas presas também foi observada na fibra, indicando que o processo ainda tem que ser melhorado.
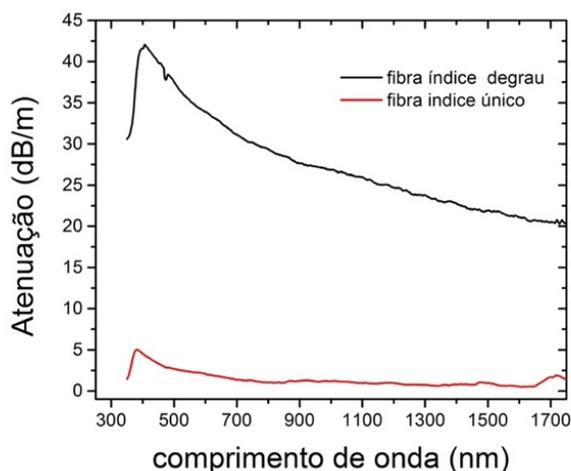
Figura 4. Atenuação medida no intervalo de 350-1750 nm.

Apesar da necessidade de melhoras em termos de pureza química de vidro e qualidade da fibra óptica para a utilização dessas fibras em aplicações ópticas, a abordagem alternativa de fabricação das fibras proposto neste trabalho constitui um novo caminho para enfrentar os desafios inerentes à fabricação complexa das fibras de vidro fluoreto-fosfato para fotônica.

Em seguida, no segundo trabalho, intitulado como "*Vidros fluoreto-fosfato dopados com terras-raras: Fundamentos estruturais das propriedades luminescentes*", envolveu a investigação estrutural de uma série de vidros FP com diferentes razões fluoreto/fosfato e a correlação das propriedades luminescentes dos vidros dopados com íons terras-raras com a estrutura.

Os vidros foram preparados na composição $xSr(PO_3)_2$-$(100-x)[AlF_3$-CaF_2-SrF_2-$MgF_2]$, $x = 5, 10, 20$ e 40 mol%, pelo método convencional de fusão-choque término em cadinho de platina. As amostras foram nomeadas como 5SrPF, 10SrPF, 20SrPF e 40SrPF, respectivamente.

Analogamente amostras vítreas com 0.5 mol% de Yb^{3+} e 0.5 mol de Eu^{3+} foram preparadas para estudo por EPR e de suas propriedades fotofísicas.

O efeito da perda de flúor sobre a estrutura local e as propriedades ópticas também foi estudado, preparando uma amostra de vidro 5SrPF dopada em um ambiente de excesso de fluoreto. Para este fim, 1g de NH_4HF_2 foi adicionado aos reagentes de partida, para remoção de impurezas de óxido e diminuição das perdas de flúor, antes da fusão. As amostras foram nomeadas como 5SrPF_0.5Eu_bif e 5SrPF_0.5Yb_bif.

Os vidros obtidos foram caracterizados por calorimetria exploratória diferencial, espectroscopia Raman e diferentes técnicas de Ressonância Magnética Nuclear (RMN) dos núcleos ^{31}P e ^{27}Al e ^{19}F. Nas amostras dopadas com Yb, experimentos de Ressonância Paramagnética Eletrônica foram realizadas e nas amostras dopadas com Eu^{3+} suas propriedades fotofísicas foram estudadas a partir de suas propriedades fotoluminescentes.

A Tg dos vidros aumentou de 439°C (5SrPF) para 522°C (40SrPF) com o aumento de $Sr(PO_3)_2$, sugerindo um aumento da conectividade da rede.

Os espectros Raman (figura 5), mostraram para amostra mais rica em fluoreto (5SrPF), bandas em 1075 e 1000 cm^{-1}, referentes aos modos de alongamento simétrico P-O em unidades $Q^{(1)}$ e $Q^{(0)}$, respectivamente. A faixa de 750 a 770 cm^{-1} é atribuída ao modo de estiramento simétrico P-O-P de oxigênio em ponte entre dois tetraedros de fosfato, tais como espécies $Q^{(1)}$ e a banda a 550 cm^{-1} pode ser atribuída à vibração de alongamento de poliedros $Al(F,O)_6$ principalmente em uma coordenação octaédrica. Finalmente, a banda larga em torno de 300-400 cm^{-1} é atribuída aos modos de flexão das unidades de fosfato. A intensidade da banda característica das unidades $Q^{(0)}$ aumenta com um aumento da concentração de fluoreto. As intensidades das bandas próximas de 760 cm^{-1} e 350 cm^{-1} diminuem à medida que a contribuição de $Q^{(1)}$ diminui. Na amostra mais rica em $Sr(PO_3)_2$ (40SrPF), o modo de alongamento P-O-P é observado em números de onda um tanto menores (750 cm^{-1} em comparação com 770 cm^{-1}), sugerindo uma contribuição adicional de unidades $Q^{(2)}$. Os dados de Raman não fornecem evidências de ligações de fósforo-flúor, que seriam observadas próximas de 850 cm^{-1}.
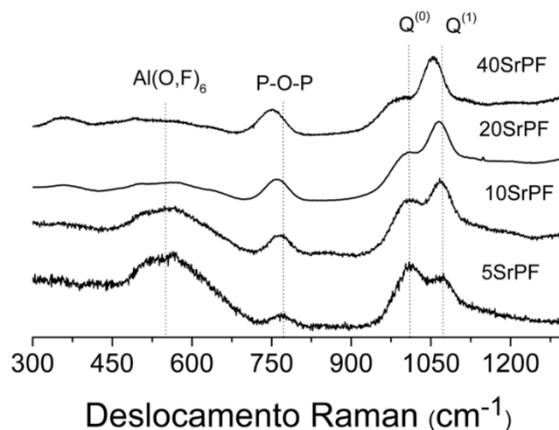
Figura 5. Espectro Raman dos vidros fluoreto-fosfato.

O espectro de RMN MAS do ^{31}P das amostras (figura 6), sugere múltiplas contribuições de unidades fosfatos $Q^{(n)}$.

A partir de doconvolução dos espectros, obsrvou-se que o vidro 40SrPF apresenta conectividades $Q^{(2)}$ e $Q^{(1)}$, na amostra 20SrPF, unidades $Q^{(1)}$ são dominantes. Para as composições 5SrPF e 10SrPF, os espectros são dominados por espécies $Q^{(0)}$ e a quase inexistência de conectividade P-O-P.
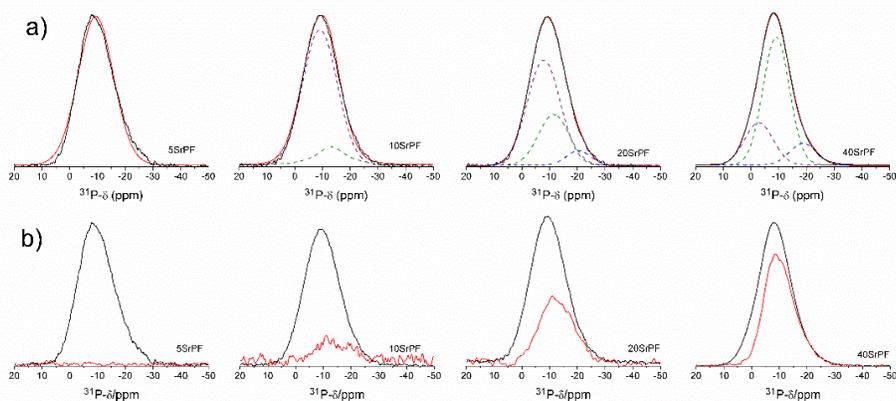

Figura 6. (a) Espectros experimentais de pulso único ^{31}P MAS RMR e modelo de deconvolução (b) Refocused INADEQUATE (traços vermelhos) e espectros de RMN de ^{31}P MAS de pulso único (traços pretos) dos vidros fluoreto-fosfato investigados. As amplitudes

dos traços preto e vermelho são escolhidas arbitrariamente e não podem ser comparadas entre si.

No espectro de RMN MAS do ^{27}Al das amostras, ressonância característica de alumínio em ambiente hexa-coordenado foi observada. Uma pequena quantidade de alumínio penta-coordenado foi observada apenas para a amostra 40SrPF.

No espectro de RMN MAS do ^{19}F (figura 7). Três linhas de ressonância foram observadas próximas. Uma linha dominante referente a átomos de flúor em um ambiente rico em metais alcalinos terrosos/alumínio, uma segunda linha que pode ser referente a espécies fluoreto ligadas a alumínio, e a terceira componente sugere um ambiente rico em alcalino terroso. Nenhuma evidencia de ligações diretas P-F foram observadas.
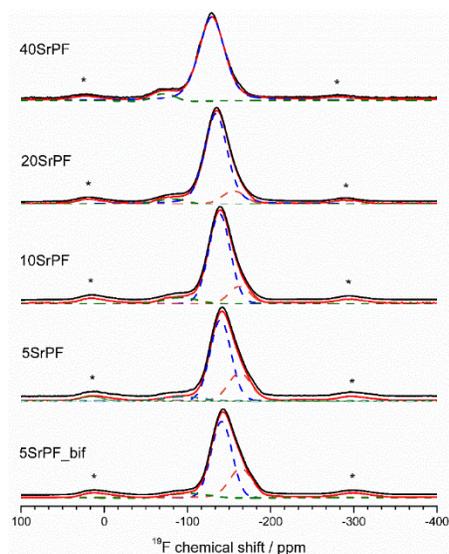

Figura 7. Espectro ^{19}F-MAS NMR dos vidros investigados. Curvas coloridas tracejadas representam as deconvolucoes em components Gaussianas individuais. Curvas pretas representam dados experimentais. Bandas laterais estao marcadas com asteriscos.

A partir das curvas REDOR de ^{19}F$\{^{31}$P$\}$, os resultados mostraram que as espécies P não estão diretamente coordenadas com F, mas que ocorrem claramente na segunda e terceira esfera de coordenação dos núcleos ^{19}F. Valores mais altos do segundo momento dipolar seriam observados se houvessem espécies P coordenadas diretamente com F.

A partir dos dados do REDOR ^{27}Al{^{31}P}. Os valores $M_{2(Al-P)}$ foram obtidos e conforme esperado, as forças de acoplamento dipolo-dipolo magnético ^{27}Al-^{31}P aumentam com o aumento da concentração de $Sr(PO_3)_2$. A comparação destes valores de $M_{2(Al-P)}$ com o medido em $Al(PO_3)_3$ (6 ligações Al-O-P a uma distância de 327 pm.), nos possibilitou estimar o número médio de átomos P na segunda esfera de coordenação do Al nos vidros, N_P, usando a fórmula $N_P = 6 \times M_{2(Al-P)}(exp)/M_{2(Al-P)}(AlPO_3)_3$. Os resultados, mostraram que o número médio de átomos de P ligado ao Al aumentam com o aumento da quantidade de fosfato. Com base no resultado de ^{27}Al MAS NMR, onde todas as espécies de Al são hexa-coordenadas, o número médio de átomos de F coordenados com Al pode ser calculado através da formula $N_F = 6 - N_P$. (tabela 1)

Tabela 1. Valores dos segundo momento $M_{2(Al-P)}$ (±10%) obtido a partir dos experimentos de ^{27}Al{^{31}P} REDOR e dados de conectividade nos vidros. N_P e (N_P/N_F) são respectivamente o numero de átomos de P e a fração de P sob átomos de F no ambiente de coordenação do Al, obtidos experimentalmente. N_{P-O-Al} (REDOR) é o número total de ligações P-O-Al obtidas por ^{27}Al{^{31}P} REDOR e N_{P-O-Al} (REAPDOR) é o número total de ligações P-O-Al obtidas por ^{31}P{^{27}Al} REAPDOR.

Amostra	$M_{2(Al-P)}$ (x10^{6}rad^{2}s^{-2})	N_P	(N_P/N_F)$_{exp}$	N_{P-O-Al} (REDOR)	N_{P-O-Al} (REAPDOR)
5SrPF	0.77	0.8	0.15	30	20
10SrPF	1.01	1.0	0.20	37	40
20SrPF	1.64	1.7	0.40	54	52
40SrPF	2.4	2.5	0.71	60	80
Al(PO$_3$)$_3$	5.8	6	-	-	-

O número médio de átomos de Al no ambiente de coordenação do P foi estimado através de experimentos de REAPDOR ^{31}P{^{27}Al} comparando os dados experimentais com simulações considerando sistemas de spin envolvendo ^{31}P e um ou dois núcleos vizinhos ^{27}Al, assumindo a distância média de P-Al observada no composto cristalino Al(PO$_3$)$_3$ (327 pm.) e um ângulo Al-P-Al de 109,4 °, que se baseia no ângulo OPO no tetraedro de fósforo. O número médio de ligações P-O-Al por unidade de fosfato é próximo de 2 para o vidro com

baixa concentração de fosfato (5SrPF e 10SrPF), 1,3 para a composição 20SrPF e 1 para a composição 40SrPF.

Em seguida, foi realizado a caracterização fotofísica nas amostras de fluoreto-fosfato dopadas com Eu^{3+} (figura 8). O comprimento de onda de excitação utilizado foi de 464 nm, o que corresponde à transição $^7F_0 \rightarrow {}^5D_2$. Todas as emissões observadas foram atribuídas às transições intraconfiguracionais de Eu^{3+} originadas nos níveis $^5D_0 \rightarrow {}^7F_J$ (J = 0, 1, 2, 3 e 4). A emissão mais intensa em torno de 620 nm é atribuída à transição de dipolo elétrico hipersensível ($^5D_0 \rightarrow {}^7F_2$), fortemente influenciada pelo ambiente químico dos íons Eu^{3+} na rede hospedeira. Por outro lado, a transição $^5D_0 \rightarrow {}^7F_1$ que ocorre através do mecanismo de dipolo magnético e sua intensidade não é sensível ao ambiente químico do Eu^{3+}. Portanto, para destacar as mudanças espectroscópicas, os espectros foram internamente normalizados para a intensidade do pico a 595 nm ($^5D_0 \rightarrow {}^7F_1$) e os valores de intensidade variaram sistematicamente com a relação fluoreto/fosfato nos vidros. Estes resultados refletem a distribuição quantitativa do ligante local (fosfato versus fluoreto) dos íons Eu^{3+} nestes vidros. A ligação com fosfato produz maior covalência da ligação em comparação com a ligação com flúor, resultando em uma maior seção transversal de emissão.
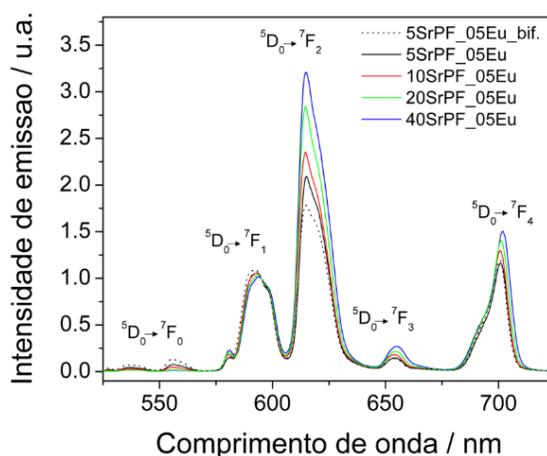

Figura 8. Espectro de emissão no visível para as amostras com 0,5 mol % de Eu^{3+}. O espectro esta internamente normalizado para a intensidade do pico 595 nm ($^5D_0 \rightarrow {}^7F_1$). A nomenclatura 5SrF_05Eu_bif indica que as amostras foram preparadas com excesso NH_4HF_2.

Outro parâmetro que é influenciado pelo ambiente químico de Eu^{3+} e foi estudado é a banda lateral de fônon a 441 nm associado à transição $^5D_0{\rightarrow}^7F_2$ permitida por dipolo elétrico e a linha de excitação mais intensa a 463 nm (figura 9). A diminuição da intensidade da banda com redução da concentração de fosfato está bem correlacionada com a diminuição paralela da concentração de espécies $Q^{(1)}$.
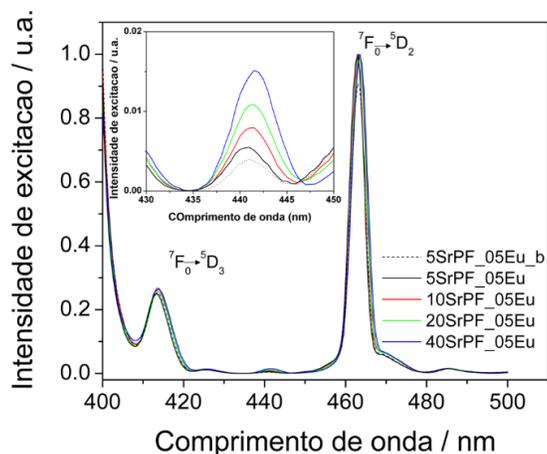

Figura 9. Espectro de excitação monitorando a transição $^7F_2{\rightarrow}^5D_0$ a 611 nm. O inset mostra a banda lateral de fônon da transição ao redor 441 nm. A nomenclatura 5SrF_05Eu_bif indica que a amostra foi preparada com excesso de NH_4HF_2.

O processo de fluoração utilizado demonstrou ser eficaz na produção de vidros de alta qualidade. Pois todos os parâmetros obtidos apresentaram melhores resultados quando comparado com as amostras sem a etapa de fluoração.

A espectroscopia de ressonância paramagnética eletrônica pulsada nas amostras dopadas com Yb^{3+} em função da relação fosfato/fluoreto nos vidros mostrou a partir do centro de gravidade dos espectros EDFS mudanças atribuídas a uma mudança sistemática da relação entre o oxigênio e o ligante fluoreto em torno do íon Yb^{3+}.

O conjunto de espectros revelou as frequências de Larmor de ^{27}Al(7,8 MHz), ^{31}P(12,0 MHz) e ^{19}F(28 MHz), sugerindo que os três tipos de núcleos estão interagindo com elétrons que residem nos orbitais 4f do Yb^{3+} e a partir dos espectros HYSCORE, as ressonâncias observadas indicaram que a interação elétron-núcleo para essas espécies está no limite de acoplamento fraco, como também observado nos espectros ESEEM. Por outro lado, além do pico diagonal na frequência de Larmor do ^{19}F, um par de ressonâncias não diagonais foram

observadas, que são deslocados simetricamente da posição diagonal correspondente à frequência de Larmor do ^{19}F. Esses picos de correlação forneceram evidências diretas de espécies ^{19}F que interagem fortemente com o elétron não compartilhado em Yb^{3+} e foram atribuídas a ligações Yb-F diretas. Este sinal foi observado para todas as amostras, exceto para a amostra 40SrPF_Yb, com a mesma forma de linha, mas um aumento sistemático de intensidade com aumento da relação F/P. Este resultado indicou que a força de acoplamento hiperfino para essas espécies é a mesma para todas as amostras e que as mudanças de intensidade refletem um aumento sistemático no número total de ligações Yb-F com aumento da relação F/P.

Em conclusão, foram fornecidas informações quantitativas sobre a organização da rede e a coordenação dos terras-raras por meio de RMN, com a sonda EPR Yb^{3+} e a sonda óptica Eu^{3+}. Os dados de Raman e RMN sugerem que a estrutura de rede dos vidros é dominada pela formação de ligações Al-O-P que podem ser quantificadas por RMN de ressonância dupla $^{27}Al/^{31}P$ e por contribuições de diferentes unidades $Q^{(n)}$. Os íons fluoreto são encontrados predominantemente em um ambiente misturado de Al/Ca/Sr/Mg. O ambiente local dos íons terras raras é caracterizado por ligações mistas de fosfato/fluoreto, que pode ser quantificada por EPR e espectroscopia óptica. A ligação de fosfato-terras raras permanece mesmo nas concentrações de fluoreto mais elevadas nestes vidros.

Por ultimo, no trabalho intitulado "*conversão ascendente de energia no ultravioleta e ambiente local em vidros fluoreto-fosfato dopados com Gd^{3+}-Tm^{3+}-Yb^{3+}*", as amostras que apresentaram melhores propriedades fotofísicas no estudo anterior, 5 e 10 mol% de fosfato, respectivamente, foram dopadas com os ions Gd^{3+}-Tm^{3+}-Yb^{3+} para o estudo de conversão ascendente de energia para possível fabricação de fibras laser no UV.

As amostras vítreas foram obtidas pelo método convencional de fusão-choque térmico. O precursor ScF_3 foi preparado pela mistura de Sc_2O_3 com excesso de $NH_4H_2F_4$. As amostras foram preparadas com diferentes concentrações de Gd^{3+}, e concentração fixa de Yb^{3+} (4% mol) e Tm^{3+} (0,1% mol).

Em seguida, a janela de absorção optica das amostras no intervalo de 180 a 1100 nm foi determinada, assim como os espectros de conversão ascendente foram obtidos a partir da excitação das amostras com laser de diodo a 980 nm na região de 250 a 750 nm. Suas

características estruturais foram determinadas por Ressonância Magnética Nuclear do ^{31}P e ^{27}Al. Estudos de ressonância dupla foram realizados nos núcleos ^{45}Sc/^{31}P e ^{27}Al/^{31}P

O espectro de RMN do ^{31}P (figura 10) apresentou uma linha alargada e assimétrica de ressonância a -10 ppm, sugerindo múltiplas contribuições de espécies fosfatos Q$^{(n)}$, com dominância de espécies Q$^{(0)}$ e quase ausência de conectividade P-O-P. No que diz respeito ao espectro RMN do ^{27}Al, observou-se uma ressonância dominante próxima a -10 ppm, característica de alumínio hexa-coordenado em um ambiente químico misto de fluoreto e fosfato. A adição de 6% de mol de íons Sc não afetou de forma representativa a estrutura vítrea e os espectros de RMN de ^{31}P e ^{27}Al MAS.
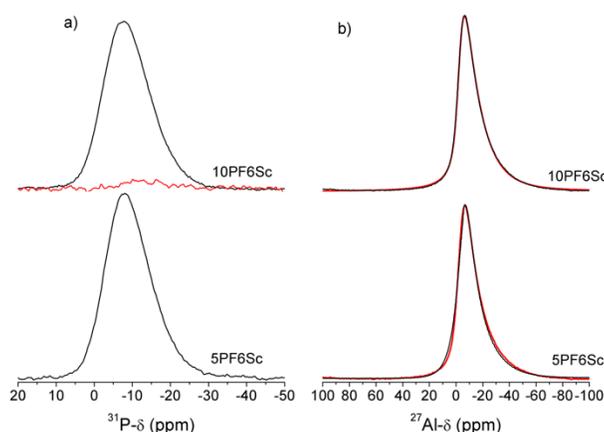

Figura 10. (a) Refocused INADEQUATE (vermelho) e single-pulse ^{31}P MAS-NMR de pulso único e (b) Espectro do ^{27}Al MAS-NMR das amostras 5PF6Sc e 10PF6Sc (preto). As curvas vermelhas representam simulações dos dados usando o modelo de Czjzek.

No espectro RMN do ^{19}F (figura 11), quatro linhas de ressonância foram observadas, atribuídas a átomos de flúor em um ambiente rico em metais alcalinos terrosos/alumínio, enquanto a linha de, espécies de flúor ligadas ao Al e um ambiente de flúor rico em metais de alcalinos terrosos. Uma nova componente em relação ao trabalho anterior, foi atribuída a espécies F em um ambiente com Sc.
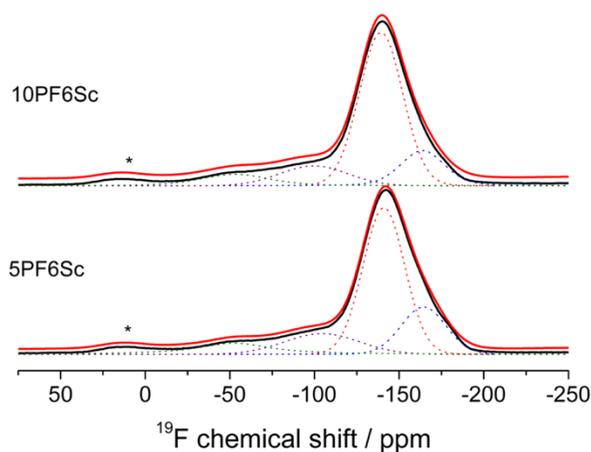
Figura 11. Espectro RMN ^{19}F das amostras 5PF6Sc e 10PF6Sc. Curvas coloridas pontilhadas representam deconvoluções em componentes Gaussianas individuais. Curvas em preto representam os dados experimentais. Bandas laterais estao marcadas com asterisco.

Medidas de ^{45}Sc{^{31}P} REDOR foram utilizadas para fornecer informações sobre o ambiente químico dos íons TRs. Os íons Sc, com raio iônico próximo do raio iônico do Tm^{3+} e Yb^{3+}, imitaram essas espécies luminescentes e forneceram uma informação mais quantitativa de sua coordenação com os átomos de P e F, nas quais resultam em diferentes energias de fônon, importantes para o processo de transferência de energia entre essas espécies. O número médio de átomos de P (N_P) na coordenação do átomo de Sc foi deduzido e determinados como 1,2 e 1,9 para 5PF6Sc e 10PF6Sc, respectivamente. O número médio de átomos de F coordenados para Sc é dado por $N_F = 6-N_P$ e foram 4,8 e 4,1 para amostra de vidro 5PF6Sc e 10PF6Sc, respectivamente. Os resultados mostraram uma ligação dominante em F para os vidros. A reação com $Sr(PO_3)_2$, AlF_3 e ScF_3 se deu com a criação de ligações P-O-Al e P-O-Sc as custas de ligações P-O-nos vidros.

Os espectros de absorção na região de 180-1100 nm, foram obtidos para os vidros fluoreto-fosfato tri-dopados com Gd^{3+}-Tm^{3+}-Yb^{3+} (10PF2Gd e 10PF4Gd) e (5PF2Gd) e co-dopados com Tm^{3+}-Yb^{3+} (10PF0Gd). A adição dos reagentes de partida de fluoretos de terras raras (GdF$_3$, YbF$_3$ e TmF$_3$), não tão puros, deslocou a borda UV para comprimentos de onda mais longos devido à introdução de impurezas de metal de transição.

Para os vidros tri-dopados, as bandas de absorção características do Gd^{3+} foram observadas a 275 e 312 nm na região UV, atribuídas à transição do estado fundamental $^8S_{7/2}$ para os estados excitados ^6I_J e ^6P_J, respectivamente. As bandas de absorção características do Tm^{3+} foram observadas no UV a 355 nm e visível a 465, 660, 685 e 785 nm, atribuídas às transições do estado fundamental $^3H_6$ para os estados excitados, $^1G_4$, $^3F_2$, $^3F_3$ e $^3H_4$, respectivamente. Finalmente, a banda de absorção observada em cerca de 1000 nm foi atribuída à transição do estado fundamental do Yb^{3+} $^2F_{7/2}$ para o excitado $^2F_{5/2}$. O espectro de absorçãoo esta mostrado na figura 12.
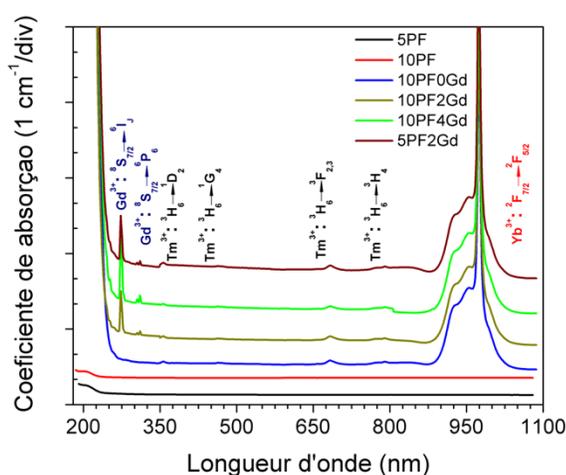

Figura 12. Espectro de absorção para as amostras sem dopagem e dopadas com Gd^{3+}-Tm^{3+}-Yb^{3+}. (o espectro foi transladado verticalmente para melhor comparação).

Após a absorção de fótons de excitação de 980 nm, as emissões do Tm^{3+} foram observadas nas regiões UV e visíveis (figura 13). Na região visível, as emissões características no azul (450 e 475 nm,) e no vermelho (650 nm) a partir das transições Tm^{3+}: $^1D_2 \rightarrow {}^3H_6$, $^1G_4 \rightarrow {}^3H_6$ e $^1G_4 \rightarrow {}^3F_4$, respectivamente, foram observadas. Na região UV, observou-se uma emissão fraca a 290 nm devido à transição $^1I_6 \rightarrow {}^3H_6$ e uma emissão mais forte a 365 nm devido à transição $^1D_2 \rightarrow {}^3H_6$ com um pequeno 347 nm devido a transição $^1I_6 \rightarrow {}^3F_4$. Uma emissão adicional a 310 nm foi observada devido à transição Gd^{3+}: $^6P_{7/2} \rightarrow {}^8S_{7/2}$.
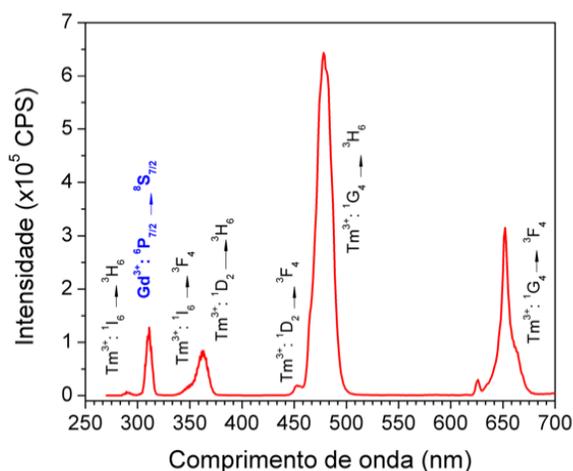
Figura 13. Espectro de emissão por conversão ascendente sob excitação a 980 nm, 200 mW para a amostra 10PF4Gd.

A banda de emissão a 310 nm sob excitação a 980 nm poderia ser também um resultado da transição do Tm^{3+}: $^3P_2 \rightarrow {}^3F_4$. Para verificar e esclarecer a origem dessa emissão, o efeito da quantidade de Gd^{3+} nos nos vidros foi estudado e comparado com uma amostra sem Gd^{3+}. Os espectros foram normalizados em relação a banda em 290 nm relacionada à transição Tm^{3+}: $^1I_6 \rightarrow {}^3H_6$.

Pudemos ver claramente que a emissão em 310 nm ocorre apenas nas amostras tri-dopados, confirmando sua origem a partir do estado excitado $^6P_{7/2}$ de íons Gd^{3+}. Essa emissão após a excitação de 980 nm foi observada pela primeira vez em vidros, e um aumento relativo de ~ 10 vezes foi observado à medida que a quantidade de Gd^{3+} foi aumentada de 2 a 4% mol nos vidros (Figura 14a).

O efeito da quantidade relativa fluoreto/fosfato na emissão por conversão ascendente do Gd^{3+} a 310 nm também foi mostrado e revelou um aumento relativo desta emissão quando a relação fluoreto/fosfato é maior. O aprimoramento relativo na emissão Gd^{3+} indicou a importância de popular o estado Tm^{3+}: ^3P_j de forma eficiente para obter uma emissão mais intensa a 310 nm (figura 14b).
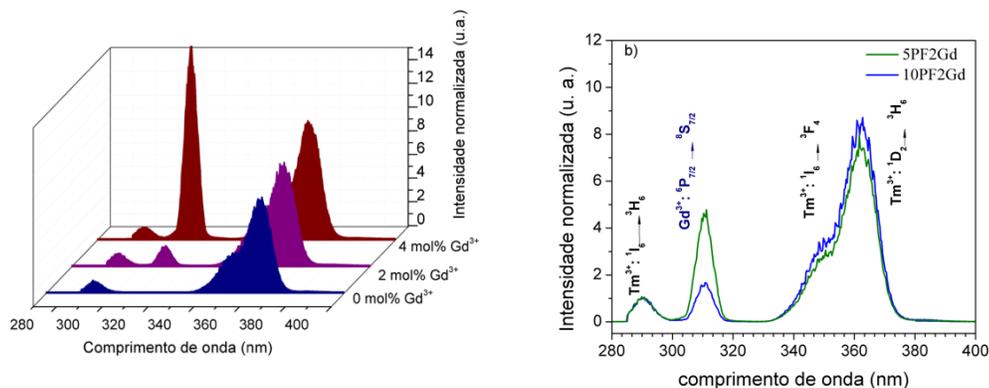
Figura 14. Espectro de emissao no UV por conversão ascendente sob excitação laser a 980 nm, 400 mW para as amostras vitreas em função da: (a) concentração de Gd^{3+} (b) da razão fluoride/phosphate. Espectros estão normalizados pela intensidade da banda $Tm^{3+} : {}^1I_6 \to {}^3H_6$ (290 nm).

O diagrama esquemático de níveis de energia dos íons Gd^{3+}, Tm^{3+} e Yb^{3+}, com os possíveis processos de conversão ascendente envolvidos nas emissões UV-Vis foi ilustrado (figura 15) e o mecanismo de transferência de energia proposto. Sob excitação de 980 nm, os íons Yb^{3+} transferem sucessivamente energia para os íons Tm^{3+} populando os níveis ${}^3H_5$, ${}^3F_3({}^3F_2)$, ${}^1G_4$, ${}^1D_2$ e ${}^1I_6$. Por sua vez, o nível ${}^6P_{7/2}$ do Gd^{3+} é populado por transferência de energia a partir dos íons Tm^{3+}. Devido à discrepância dos níveis de energia, a interação dipolo-dipolo tem um caráter não-ressonante e a transferência de energia é não-radiativa e tem a participação de fônons.
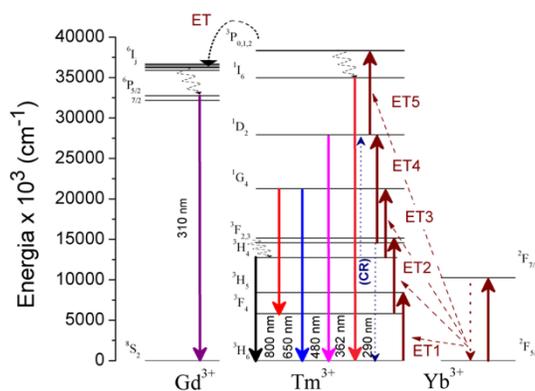

Figura 15. Diagrama de energia dos niveis do Gd^{3+}, Tm^{3+} and Yb^{3+} com os possiveis processos de conversao ascendente.

A dependência da intensidade de emissão versus a potência de excitação a 980 nm de 100 a 250 mW para a amostra representativa 10P90F: $2Gd^{3+}$: $0.1Tm^{3+}$: $4Yb^{3+}$ foi estudada (figura 16). O número de fótons (n) requeridos para popular os estados emissores foram determinados como sendo quatro e cinco, indicando processos de conversão ascendente envolvendo 4 fótons para a emissão de 362 nm e cinco fótons para as emissões a 310 nm e 290 nm, em concordância com o processo de transferência de energia descrito acima.
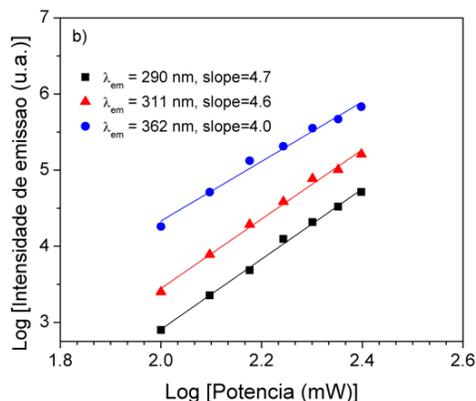

Figura 16. Plote Log-log das emissões a 290, 310 e 360 nm apos excitação a 980 nm para a 10PF2Gd.

Portanto, utilizando o Sc como um mímico diamagnético para as espécies de terra-raras luminescentes Tm^{3+} e Yb^{3+} com raio iônico semelhantes, a distribuição do ligante em torno dos íons terra-raras pode ser quantificada pela técnica de ressonância dupla $^{45}Sc/^{31}P$ REDOR juntamente com compreensões estruturais por meio de outras técnicas de RMN. A estrutura da rede pode ser caracterizada e o número médio mais alto de átomos de F coordenados a átomos de Sc (mimico para os terra-raras) resultou em uma emissão do Gd^{3+} mais intensa no UV.

RÉSUMÉ COMPLET DE LA THÈSE

Cette section résume les principaux résultats de cette thèse de doctorat publiés dans trois articles.

Les verres à base de *fluorophosphate* sont des matériaux hautement transparents dans l'UV lorsqu'ils possèdent de faibles quantités d'impuretés, offrant ainsi une alternative aux fibres de silice utilisées aujourd'hui dans cette région du spectre électromagnétique. Ces verres sont produits par le mélange de fluorures et polyphosphates et combinent ainsi leurs propriétés telles que : une excellente aptitude à vitrifier, un faible indice de réfraction et une large fenêtre de transmission (~ 160-4000 nm). Toutefois, peu d'études ont été rapportées à ce jour sur leur méthode de fabrication et par conséquent, les pertes optiques dans la région UV. La seule fibre connue pouvant opérer dans l'UV (~170-300 nm) est constituée de silice pure dopée avec OH/F. Cependant, l'utilisation de telles fibres est limitée par l'effet de solarisation qui dégrade la transmission de la lumière UV après une exposition prolongée.

Le développement de nouvelles fibres optiques capables de transmettre dans les régions de l'ultraviolet moyen (200-300 nm) et lointain (120-200 nm) bénéficierait aux techniques de microlithographie, aux technologies laser, et également à la détection chimique (détection du phosphore et du soufre pour l'agriculture), la principale motivation de ce travail. En outre, les verres mixtes fluorure/phosphate peuvent offrir un environnement de fluorures de faible énergie de phonons qui est favorable pour l'émission avec une grande efficacité quantique lorsqu'ils sont dopés avec des ions de terre rare trivalents. Une telle propriété rend alors leur utilisation attractive pour d'autres applications également sous forme de fibres et/ou verres massifs dans le domaine de la photonique.

Par conséquent, en ce qui concerne le premier papier intitulé *"Fibre optique à saut d'indice pour la transmission de lumière UV à base de verre fluorophosphate fabriqué par la technique du creuset"*, des échantillons vitreux dans les systèmes $10Sr(PO_3)_2$-90 (AlF_3, MgF_2, CaF_2, SrF_2) et $xBA(PO_3)_2$-100-x (AlF_3, CaF_2, SrF_2, MgF_2), avec x = 5, 10 et 20, ont été préparés par le procédé classique de fusion-trempe des réactifs de grande pureté chimique ($\geq$5N) dans un environnement réducteur (creuset en carbone vitreux).

Les températures caractéristiques ainsi que la fenêtre de transmission ont ensuite été déterminées. La Tg des verres augmente de 439°C à 460°C avec l'augmentation de la concentration en phosphate alors qui un élargissement du pic de cristallisation est observé. Le verre avec 10%mol de phosphate de baryum et 90%mol de fluorures offre une stabilité thermique plus élevée par rapport au verre avec 5%mol de phosphate. Il a donc été choisi pour la fabrication de la fibre. $Ba(PO_3)_2$ a été substitué par $Sr(PO_3)_2$ dans la composition pour diminuer son indice de réfraction en vue préparer une préforme à saut d'indice (coeur/gaine).

La transmission dans la région UV (figure 1) du verre pour une épaisseur de 1,5 mm atteint 90% au-dessus de 240 nm et est proche de 75% à 180 nm. Une petite bande d'absorption a été observée à 220 nm. Elle est due à l'absorption des impuretés Fe^{2+}. Dans la région infrarouge, la transmission atteint 91% et se prolonge.
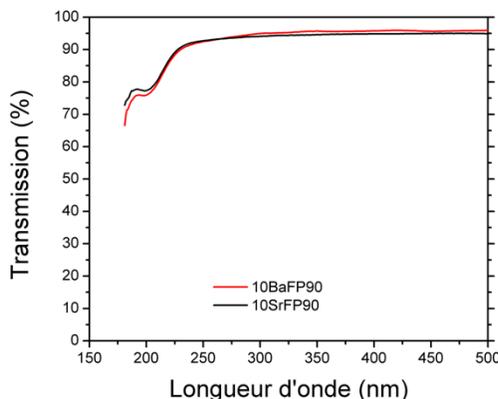

Figure 1. Spectre de transmission dans la région l'UV des verres pour la préforme.

Pour la préparation de la fibre optique à saut d'indice, une nouvelle méthode comprenant deux étapes a été utilisée : (i) préparer les préformes et ; (ii) étirer la fibre à partir de la préforme préparée à l'aide d'un creuset en silice. Tout d'abord, les verres de cœur (composition $[10Ba(PO_3)_2-90(AlF_3, CaF_2, MgF_2, SrF_2)]$) et de gaine $[10Sr (PO_3)_2-90(AlF_3, MgF_2, CaF_2, SrF_2)]$ ont été préparés puis refondus sous vide à 730ºC pendant 1 heure. Ensuite, un tube cylindrique du verre de gaine et un cylindre (rod) du verre ont été fabriqués séparément.

Du point de vue expérimental, la première méthode exploitée pour produire des fibres fluorophosphate consistait à étirer simplement une préforme par le procédé classique. Cependant, de sérieux problèmes de cristallisation sur la surface des fibres pendant le

processus d'étirage ont été observés. Une autre méthode a alors été mise en œuvre. Elle consiste à préparer une préforme puis à l'étirer à travers un creuset en silice fondue. La préforme est ainsi insérée dans le creuset en silice fondue et chauffée. Ensuite, la fibre est rapidement retirée de la buse de sortie dans le creuset de silice par le bas. Aucune trace de cristallisation n'est alors observée. Des fibres monoindices ont été également produites par la même technique.
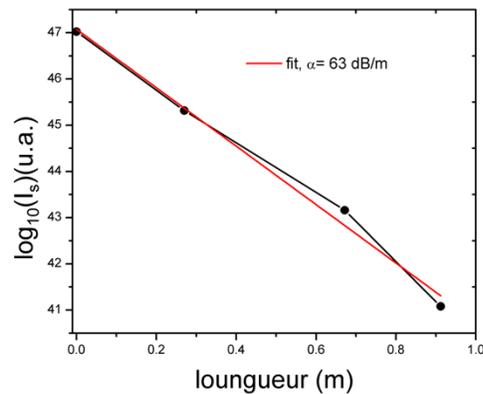

Figure 2. Puissance de sortie de la fibre à 244 nm par la longueur de fibre.

Pour la fibre à saut d'indice, l'atténuation obtenue à 244 nm était de 63 dB/m (figure 2). Les pertes diminuent (42-20 dB/m) dans la gamme 407-1750 nm (figure 3). À 350 nm, une augmentation brutale des pertes a été observée et probablement due à la présence d'impuretés de métaux de transition. À titre de comparaison, la même mesure a été effectuée sur une fibre monoindice. Pour cette dernière, un comportement similaire a été observé, mais les pertes sont inférieures d'environ un ordre de grandeur, soit 5 dB/m avec un minimum de ~ 0,7 dB/m. Les fortes pertes mesurées dans la fibre à saut d'indice par rapport à la fibre monoindice sont probablement dues à des pertes extrinsèques provoquées par des imperfections dans les interfaces de la préforme et de contact avec les parois du creuset en silice. La présence de striae dans la fibre a été observée, pouvant entraîner des pertes extrinsèques. La présence de bulles piégées dans la fibre a été également observée, ce qui indique que le processus doit encore être amélioré.
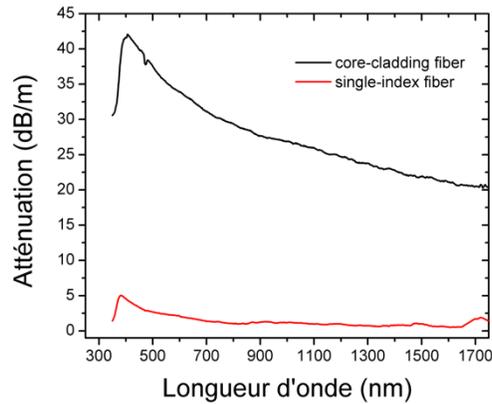
Figure 3. Atténuation dans la gamme de 350-1750 nm.

Malgré la nécessité d'amélioration en termes de pureté chimique du verre et de qualité optique pour leur utilisation dans des applications optiques, l'approche alternative à la production de fibres proposée ici est une nouvelle façon de relever les défis inhérents à la fabrication complexe des fibres fluorure/phosphate (FP) pour la photonique.

Le deuxième papier intitulé *"Verres de fluoruro/phosphate dopés avec des terres rares: Principes structurels de propriétés de luminescence"*, est composé de deux parties : l'étude structurale des verres FP avec différent ratios fluorure/phosphate et la corrélation des propriétés luminescentes de verres dopés avec des ions de terres rares avec leur structure.

Les verres de compositions $Sr(PO_3)_2$-(100-x)[AlF_3, CaF_2, SrF_2, MgF_2], x = 5, 10, 20 et 40%mol ont été préparés par le procédé classique. Les échantillons ont été désignés comme 5SrPF, 10SrPF, 20SrPF et 40SrPF, respectivement. De la même façon, des échantillons vitreux avec 0,5%mol de Yb^{3+} ou Eu^{3+} ont été préparés pour l'étude par EPR de leurs propriétés photophysiques.

L'effet de la perte de fluorures sur la structure locale et sur les propriétés optiques a été également étudié en préparant un échantillon de verre dopé 5SrPF dans une matrice vitreuse avec une concentration élevée en fluorures. Les échantillons ont été désignés par 5SrPF_0.5Eu_bif et 5SrPF_0.5Yb_bif. Les verres obtenus ont été caractérisés par différentes techniques, calorimétrie différentielle à balayage (DSC), spectroscopie Raman et résonance magnétique nucléaire à l'état solide (RMN).

L'analyse thermique par DSC a montré que la température de transition vitreuse Tg des verres préparés augmente de 439°C (5SrPF) à 522°C (40SrPF) avec l'augmentation de la concentration de $Sr(PO_3)_2$, ce qui suggère une augmentation de la connectivité du réseau.

De plus, les spectres Raman (figure 4) montrent deux bandes à 1075 et 1000 cm^{-1} pour les échantillons les plus riches en fluorures (5SrPF), attribuées aux modes d'étirement symétrique dans les unités phosphates $Q^{(1)}$ et $Q^{(0)}$, respectivement. En ce qui concerne la bande large située entre 750-770 cm^{-1}, elle est attribuée au mode de vibration P-O-P, oxygène pontant entre les deux tétraèdres de phosphate, tels que les espèces $Q^{(1)}$. La bande observée à 550 cm^{-1} est attribuée à la vibration d'étirement du polyèdres $Al(F,O)_6$. Enfin, la large bande autour de 300-400 cm^{-1} est attribuée à la flexion d'unités phosphates. L'intensité de la bande caractéristique des unités $Q^{(0)}$ augmente avec la concentration de fluorures. Les intensités des bandes proches de 760 cm^{-1} et 350 cm^{-1} diminuent à mesure que la quantité de $Q^{(1)}$ diminue. Dans l'échantillon le plus riche en $Sr(PO_3)_2$ (40SrPF), les modes d'étirement POP ont été observés à des nombres d'onde un peu plus faibles (750 cm^{-1} par rapport à 770 cm^{-1}), ce qui suggère une contribution supplémentaire de motifs $Q^{(2)}$.
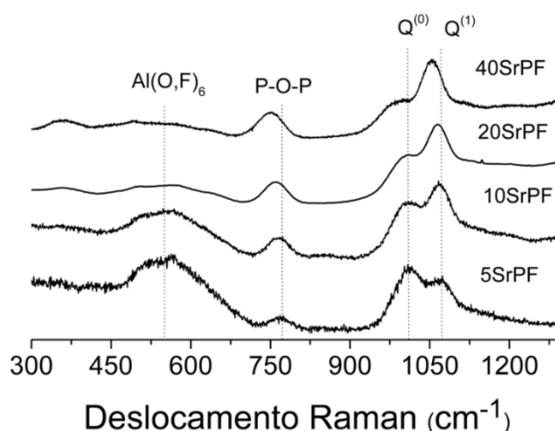

Figure 4. Spectre Raman des verres fluorophosphate.

Les spectres ^{31}P-RMN-MAS (figure 5) enregistrés sur les échantillons suggèrent les contributions de plusieurs unités phosphates $Q^{(n)}$. Avec la déconvolution spectrale, il a été observé que le verre 40SrPF a une connectivité $Q^{(2)}$ et $Q^{(1)}$, tandis que pour l'échantillon

20SrPF, les unités $Q^{(1)}$ sont dominantes. Pour les compositions 5SrPF et 10SrPF, les spectres sont dominés par des espèces $Q^{(0)}$ et presque aucune connectivité P-P n'est observée.
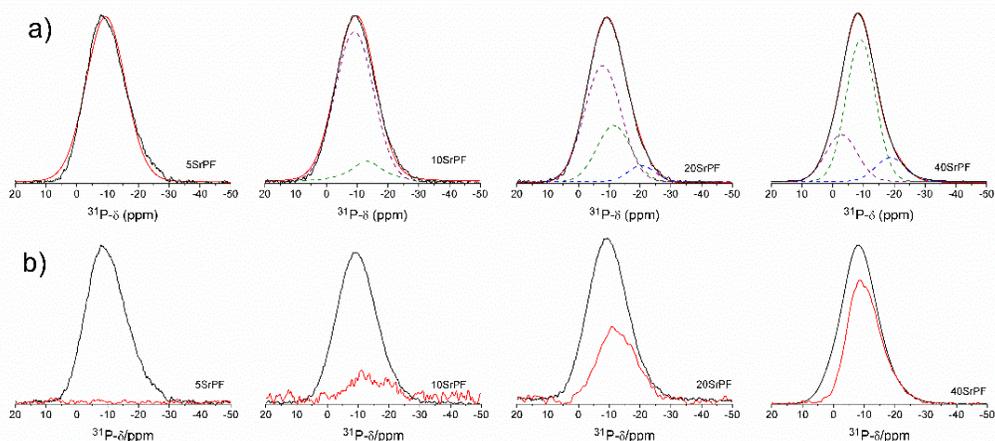

Figure 5. a) Spectres expérimentaux ^{31}P-MAS-RMN et déconvolution modèle. Refocused INADEQUATE (lignes rouges) et MAS RMN ^{31}P (lignes noires) des verres étudiés. Les amplitudes des traces noires et rouges sont choisies de façon arbitraire et ne peuvent pas être comparées.

Un environnement caractéristique des aluminiums en coordinance six a été observé. Une petite quantité d'aluminium penta-coordonné a été observée pour l'échantillon avec une teneur maximale en phosphate (40SrPF).

Dans les spectres ^{19}F-RMN-MAS (figure 6), trois signaux de résonance ont été observés. Un signal dominant référant à des atomes de fluor dans un environnement riche en métal alcalino-terreux/aluminium, un second signal relié à l'espèce fluorure d'aluminium et le troisième suggérant un environnement riche en alcalin. Aucune preuve de liens directs P-F n'a été observée.
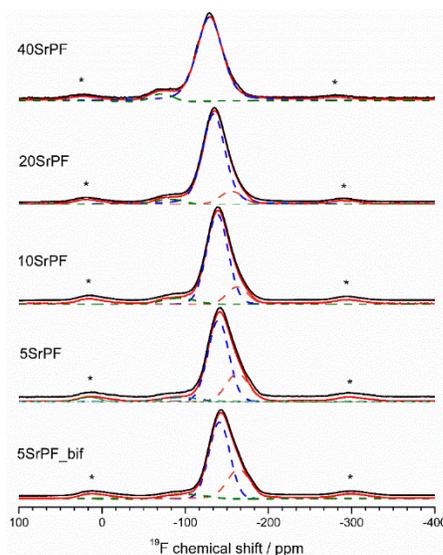
Figure 6. Spectre de ^{19}F-RMN des verres étudiés. Les courbes colóres en pointilles représentent les composants individuels dans la deconvolution gaussienne. Les courbes noires représentent les données expérimentales.

A partir des courbes REDOR ^{19}F$\{^{31}$P$\}$, les résultats ont montré que les espèces P ne sont pas directement coordonnées à F, mais plutôt dans la deuxième et la troisième sphère de coordination. Des valeurs plus élevées du deuxième moment dipolaire (M_2) seraient observés s'il y avait des espèces P coordonnées directement avec F.

A partir des données ^{27}Al$\{^{31}$P$\}$, les valeurs $M_{2(Al-P)}$ ont été obtenues et, comme prévu, les forces de couplage magnétique dipôle-dipôle augmentent avec l'augmentation de la concentration de Sr(PO$_3$)$_2$. Le nombre moyen d'atomes Al dans l'environnement de coordination de P a été estimé par des expériences REAPDOR ^{31}P$\{^{27}$Al$\}$ comparant les données expérimentales aux simulations. Le nombre moyen de liaisons P-O-Al par unité de phosphate est proche de 2 pour le verre avec une faible concentration de phosphate (5SrPF et 10SrPF), 1,3 pour la composition 20SrPF et 1 pour le verre 40SrPF.

Ensuite, la caractérisation photophysique a été réalisée sur les verres dopés avec Eu^{3+} (figure 7). La longueur d'onde d'excitation utilisée était de 464 nm, qui correspond à la transition ^{7}F$_0$→^{5}D$_2$. Toutes les émissions observées ont été attribuées aux transitions dans les niveaux ^{5}D$_0$→^{7}F$_J$ (J = 0, 1, 2, 3 e 4) de l'ion Eu^{3+}. L'émission la plus intense (620 nm) est attribuée à la transition dipolaire électrique hypersensible (^{5}D$_0$→^{7}F$_2$), fortement influencée par l'environnement chimique des ions Eu^{3+} dans le réseau-hôte. D'autre part, la transition

($^5D_0 \rightarrow ^7F_1$) se produit à travers le mécanisme de dipôle magnétique et son intensité n'est pas sensible à l'environnement chimique. Par conséquent, les changements spectroscopiques ont été normalisés à l'intensité du pic à 595 nm ($^5D_0 \rightarrow ^7F_1$) et les valeurs d'intensité varient de manière systématique avec l'augmentation de la concentration de phosphate. Ces résultats reflètent la distribution quantitative des phosphates par rapport aux fluorures autour des ions Eu^{3+}.
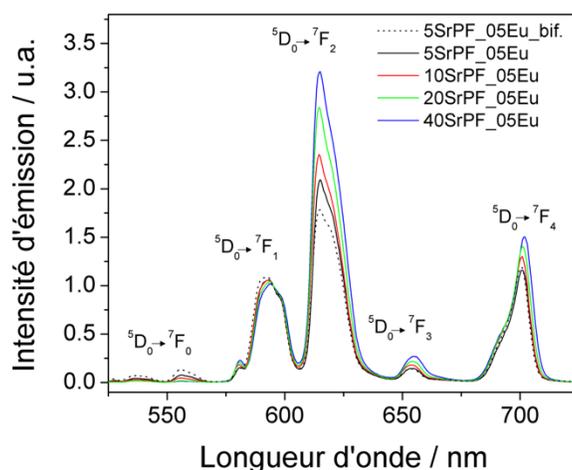

Figure 7. Spectre d'émission dans le visible pour des échantillons dopés avec 0,5% en mole de Eu^{3+}. Le spectre est normalisé à l'intensité de pic 595 nm. La nomenclature 5SrF_05Eu_bif indique que les échantillons ont été préparés avec excès de NH_4HF_2.

Un autre paramètre qui est influencé par l'environnement chimique de Eu^{3+} a été étudié, c'est la bande latérale de phonon associée à la transition 441 nm (figure 8) : $^5D_0 \rightarrow ^7F_2$. Une diminution de l'intensité de la bande avec une concentration réduite en phosphate est bien corrélée avec la diminution en parallèle de la concentration des espèces $Q^{(1)}$.
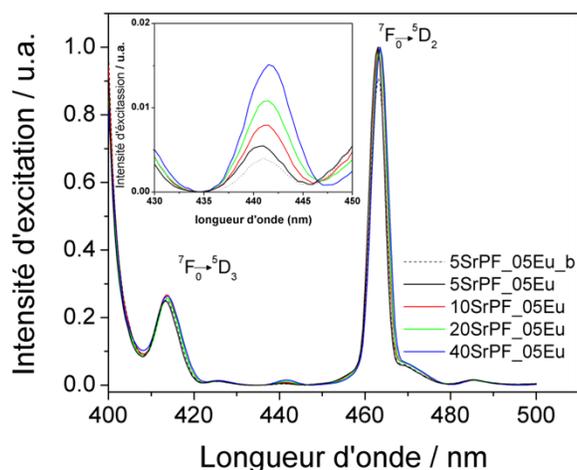
Figure 8. Spectre d'excitation (longueur d'onde d'émission à 611 nm). L'encart montre la bande latérale de phonons autour de 441 nm. La nomenclature 5SrF_05Eu_bif indique que l'échantillon a été préparé avec un excès de NH_4HF_2.

La spectroscopie EPR pulsée dans des échantillons dopés avec Yb^{3+} en fonction de la quantité relative fluorure/phosphate a montré des modifications systématiques de la relation entre l'oxygène et le fluorure autour de l'ion Yb^{3+}.

L'ensemble des spectres a révélé la fréquence de Larmor du ^{27}Al(7,8 MHz), ^{31}P(12,0 MHz) et ^{19}F(28MHz), ce qui suggère que les trois types de noyau sont en interaction avec les électrons résidants dans les orbitales 4f du Yb^{3+}. Les spectres ont fourni des preuves directes que les espèces ^{19}F interagissent fortement avec l'électron non partagé de Yb^{3+} et ont été attribués à diriger des liaisons Yb-F. Ce signal a été observé pour tous les échantillons, sauf pour l'échantillon 40SrPF_Yb avec la même ligne de forme, mais une augmentation systématique en intensité avec l'augmentation de la quantité relative fluorure/phosphate. Ce résultat indique que la force de couplage hyperfin de ces espèces est la même pour tous les échantillons et les changements d'intensité reflètent une augmentation systématique du nombre total de liaisons Yb-F avec l'augmentation de la quantité relative fluorure/phosphate.

En conclusion, les informations quantitatives ont été fournies sur l'organisation du réseau et la coordination des terres rares. Les données Raman et RMN suggèrent que la structure de réseau du verre est dominée par la formation de liaisons Al-P et les contributions des différentes unités $Q^{(n)}$. Les ions fluorures sont trouvés principalement dans un

145

environnement mixte Al/Ca/Sr/Mg. L'environnement local des ions de terres rares est caractérisé par des liaisons communes phosphate/fluorure. La liaison phosphate-terre rare est toujours présente, même aux concentrations les plus élevées en fluorures dans ces verres.

Enfin, dans l'article intitulé *″L´émission UV par upconversion dans un verre très transparent dopé avec Gd^{3+}-Tm^{3+}-Yb^{3+}″*, les échantillons étudiés présentent de meilleures propriétés photophysiques que ceux des études précédentes. Ces verres contiennent 5 et 10% en moles de phosphate, 5PF6Sc et 10PF6Sc respectivement, et ont été dopés avec des ions Gd^{3+}-Tm^{3+}-Yb^{3+} pour l'étude des émissions par upconversion après excitation dans l'infrarouge. Leurs propriétés structurales ont également été explorées par la résonance magnétique nucléaire du ^{45}Sc, incorporé pour imiter les ions de terres rares dans la matrice vitreuse.

Les résultats ont montré que l'addition de 6 %mol d'ions Sc n'a pas affecté la structure du verre de manière significative (figure 9). Dans le spectre du ^{19}F-RMN-MAS, un nouvel élément par rapport au travail précédent a été attribué à des espèces F dans un environnement avec Sc (figure 10).
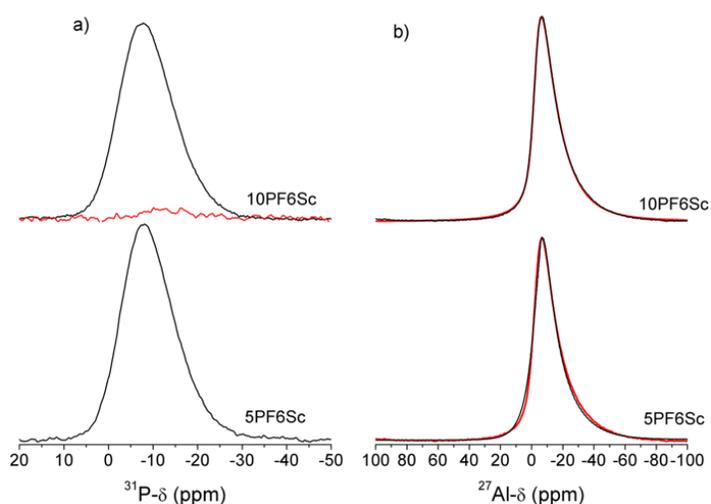

Figure 9. (a) Refocused INADEQUATE (rouge) et ^{31}P-NMR-MAS (b) Spectre ^{27}Al-NMR-MAS des verres 5PF6Sc et 10PF6Sc (noire). Les courbes rouges représentent des données de simulation à l'aide du modèle Czjzek.

Les mesures de Redor $^{31}P\{^{45}Sc\}$ ont été utilisées pour fournir des informations sur l'environnement chimique des trois ions de terres rares. Les ions Sc ayant un rayon ionique proche du rayon ionique de Tm^{3+} et Yb^{3+}, imitent ces espèces luminescentes et ont fourni une information plus quantitative de leur coordination avec les atomes de P et F, lesquelles se traduisent par différentes énergie de phonon, importantes pour les processus de transfert d'énergie entre ces espèces. Le nombre moyen d'atomes de P liés à l'atome de Sc a été déterminé comme étant de 1,2 et de 1,9 pour les verres 5PF6Sc et 10PF6Sc, respectivement. Les résultats montrent que les ions Sc^{3+} sont principalement liés aux atomes de fluor dans ces verres.
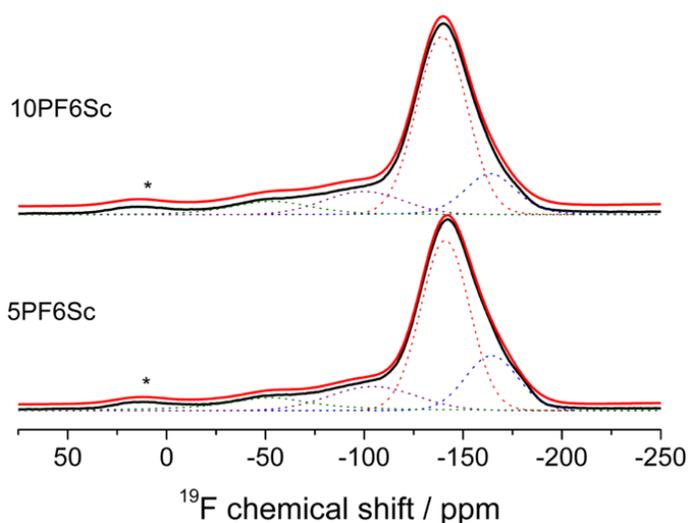

Figure 10. Spectre ^{19}F-RMN des échantillons 5PF6Sc 10PF6Sc. Les courbes en pointillés colorés représentent des composantes de déconvolution gaussienne individuelle. Les courbes en noir représentent les données expérimentales.

Les spectres d'absorption dans la région de 180-1100 nm (figure 11) ont été obtenus pour les verres de fluorure/phosphate tri-dopés avec Gd^{3+}-Tm^{3+}-Yb^{3+}. Les bandes d'absorption caractéristiques du Gd^{3+} ont été observées dans les domaines UV et visible, ainsi que les absorptions caractéristiques du Tm^{3+}. Enfin, la bande d'absorption de l'ion Yb^{3+} a été observée dans la région infrarouge proche.
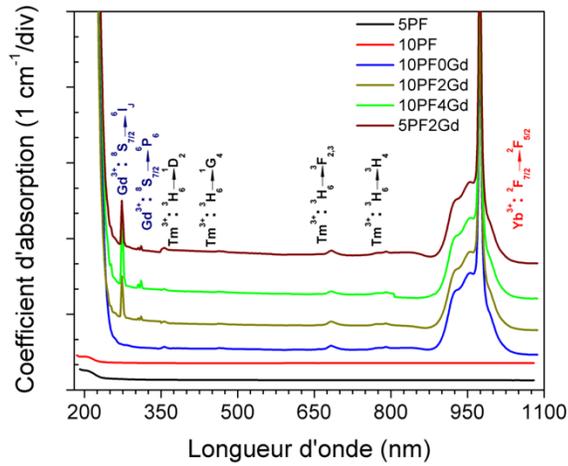
Figure 11. Spectres d'absorption pour les échantillons non-dopés et dopés Tm^{3+}- Gd^{3+}- Yb^{3+}. (Les spectres ont été déplacé verticalement pour une meilleure comparaison).

Après l´absorption de photons d'excitation à 980 nm, l'émission de Tm^{3+} a été observée dans les régions UV et visible (figure 12). Une émission supplémentaire à 310 nm a été observée en raison de l'émission du Gd^{3+}. Cette émission a augmenté avec l'augmentation de Gd^{3+} dans les verres.
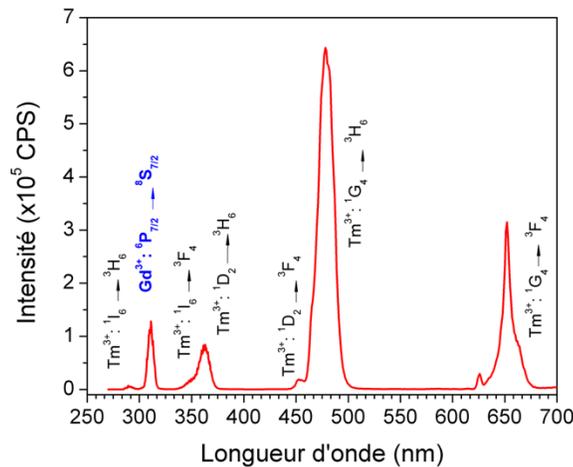

Figure 12. Spectre d'émission par upconversion sous excitation à 980 nm, 200 mW pour l'échantillon 10PF4Gd.

L'effet de la quantité relative fluorure/phosphate sur l'émission par upconversion du Gd^{3+} à 310 nm été montré (figure 13a) et il y a une augmentation relative de cette émission lorsque la quantité relative fluorure/phosphate augmente (figure 12b).
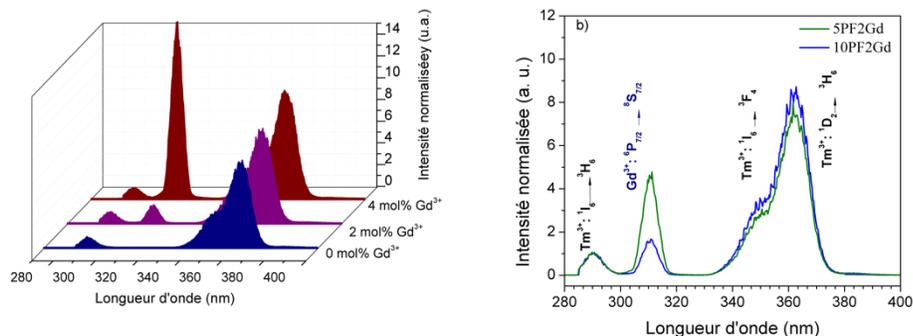

Figure 13. Spectre d'émission dans l'UV par upconversion sous excitation laser à 980 nm, 400 mW. a) Gd^{3+} contenu, b) quantité relative fluorure/phosphate.

Le schéma des niveaux d'énergie des ions Gd^{3+}, Tm^{3+} et Yb^{3+}, avec des processus possibles de upconversion a été montré et le mécanisme de transfert d'énergie proposé (figure 14). Sous excitation à 980 nm, les ions Yb^{3+} transfèrent l'énergie successivement aux ions Tm^{3+}. À son tour, le niveau excité du Gd^{3+} est peuplé par transfert d'énergie à partir des ions Tm^{3+}.
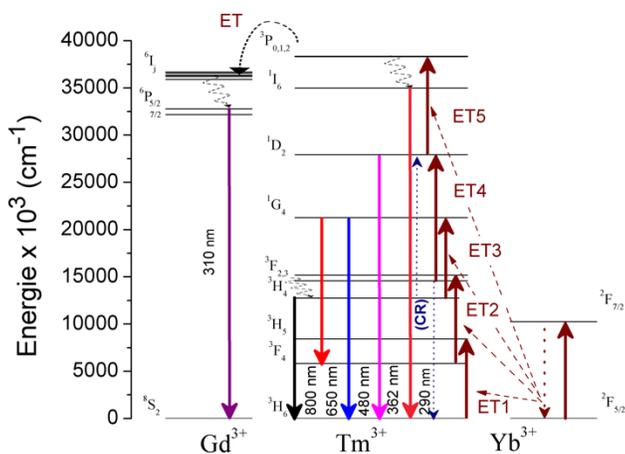

Figure 14. Diagramme des niveaux d'énergie de Gd^{3+}, Tm^{3+} et Yb^{3+} avec les processus possibles de upconversion.

La dépendance de l'intensité d'émission en fonction de la puissance d'excitation à 980 nm de 100 à 250 mW a été étudiée (figure 15). Le nombre de photons nécessaires pour remplir les états d'émission a été déterminé, étant 4 et 5, indiquant un processus de upconversion impliquant quatre photons à l'émission de 362 nm et cinq photons pour des émissions à 310 nm et 290 nm.

Par conséquent, en utilisant le [45]Sc comme remplaçant diamagnétique pour imiter les espèces de terres rares luminescents, l'environnement autour des ions de terres rares peut être quantifié par la technique de double résonance. Le plus grand nombre moyen d'ions de fluorures coordonnés aux Sc a conduit à une émission plus intense dans l'UV du Gd^{3+}.
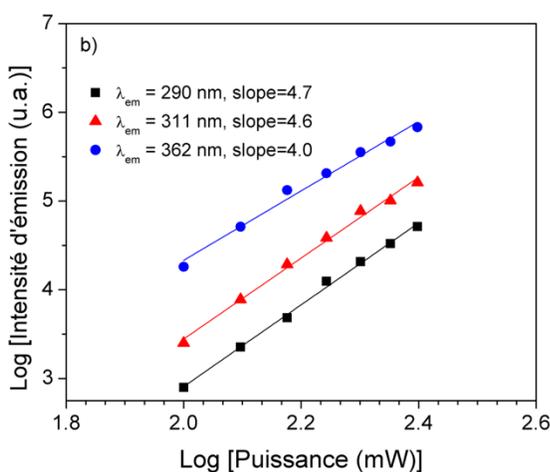

Figure 15. Log-log de l'émission à 290, 310 et 360 nm après excitation à 980 nm.

REFERENCES

ANDREW, E. R.; BRADBURY, A.; EADES, R. G. Removal of Dipolar Broadening of Nuclear Magnetic Resonance Spectra of Solids by Specimen Rotation. **Nature**, v. 183, p. 1802–1803, 1959.

BACH, H.; NEUROTH, N. **The properties of optical glass**. 2nd ed. Berlin: Springer, 1998. 414 p.

BERSUKER, I. B. Electronic structure and chemical bonding. In: **Electronic structure and properties of transition metal compounds**. Hoboken: John Wiley & Sons, 2010. Chap. 6, p. 238-323.

BRINKMANN, M. Optical materials and their properties. In: TRÄGER, F. (Ed.). **Springer handbook of lasers and optics**. New York: Springer, 2007. p. 249-372.

COOK, L.; MADER, K. H. Ultraviolet transmission characteristics of a fluorophosphate laser glass. **Journal of the American Ceramic Society**, v. 65, n. 12, p. 597-601, 1982.

CAMPOS, R. C. de; CORREIA, C. L. T.; VIEIRA, F.; SAINT'PIERRE, T.D.; OLIVEIRA, A. C.; GONÇALVES, R. Direct determination of P in biodiesel by high-resolution continuum source graphite furnace atomic absorption spectrometry. **Spectrochimica Acta Part B**: Atomic Spectroscopy, v. 66, n. 5, p. 352-355, 2011.

OLIVEIRA, M. de; UESBECK, T.; GONÇALVES, T. S.; MAGON, C. J.; PIZANI P. S. de CAMARGO A. S. S.; ECKERT, H. Network structure and rare-earth ion local environments in fluoride phosphate photonic glasses studied by solid-state NMR and electron paramagnetic resonance spectroscopies. **The Journal of Physical Chemistry C**, v. 119, n. 43, p. 24574-24587, 2015.

EHRT, D.; CARL, M.; KITTEL, T.; MULLER, M.; SEEBER, W. High-performance glass for the deep ultraviolet range. **Journal of Non-Crystalline Solids**, v. 177, p. 405-419, 1994.

EHRT, D. Redox behaviour of polyvalent ions in the ppm range. **Journal of Non-Crystalline Solids**, v. 196, p. 304-308, 1996.

EHRT, D. Review: Phosphate and fluoride phosphate optical glasses — properties, structure and applications. **European Journal of Glass Science and Technology Part B**: Physics and Chemistry of Glasses, v. 56, n. 6, p. 217-234, 2015.

EHRT, D.; LEISTER, M.; MATTHAI, A. Polyvalent elements iron, tin and titanium in silicate, phosphate and fluoride glasses and melts. **Physics and Chemistry of Glasses**, v. 42, n. 3, p. 231-239, 2001.

EHRT, D.; SEEBER, W. Glass for high performance optics and laser technology. **Journal of Non-Crystalline Solids**, v. 129, n. 1/3, p. 19-30, 1991.

GULLION, T. Measurement of dipolar interactions between spin- 1 2 and quadrupolar nuclei by rotational-echo, adiabatic-passage, double-resonance NMR. **Chemical Physics Letters**, v. 246, n. 3, p. 325–330, 1995.

GUPTA, P. K. Non-crystalline solids: glasses and amorphous solids. **Journal of Non-Crystalline Solids**, v. 195, n. 1/2, p. 158-164, 1996.

JIANG, X.; JOLY, Y. N.; FINGER, A. M.; BABIC, F.; WONG, G. K. L.; TRAVERS, J. C.; RUSSEL, P. S. J. Deep-ultraviolet to mid-infrared supercontinuum generated in solid-core ZBLAN photonic crystal fibre. **Nature Photonics**, v. 9, n. 2, p. 133-139, 2015.

KALNINS, C. A. G.; HEIDEPRIEM, H. E.; DOWLER, A.; MONRO, T. M. Fabrication of fluoride phosphate glass optical fibres for UV applications. In: **INTERNATIONAL QUANTUM ELECTRONIC CONFERENCE; CONFERENCE LASERS ELECTRO-OPTICS**, Sydney, 2011. [Washington, DC]: AOS, 2011. p. 2051-2053. CD ROM.

KITAMURA, N.; HAYAKAWA, J.; YAMASHITA, H. Optical properties of fluoroaluminate glasses in the UV region. **Journal of Non-Crystalline Solids**, v. 126, n. 1/2, p. 155-160, 1990.

LUCAS, J.; SMEKTALA, F.; ADAM, J. L. Fluorine in optics. **Journal of Fluorine Chemistry**, v. 114, n. 2, p. 113-118, 2002.

MATTHAI, A.; EHRT, D.; RÜSSEL, C. Redox behaviour of polyvalent ions in phosphate glass melts and phosphate glasses. **Glass Science and Technology**, v. 71, n. 7, p. 187-192, 1998.

MIMURA, Y.; NAKAI, T. Optical fiber loss mechanisms. In: AGGARWAL, I. D.; LU, G. (Ed.). **Fluoride glass fiber optics**. NewYork: Elsevier, 1991. p. 235-274.

MÖNCKE, D.; EHRT, D.; VELLI, L. L.; VARSAMIS, C. P. E., KAMITSOS, E. I. Structure and properties of mixed phosphate and fluoride glasses. Physics and Chemistry of Glasses-**European Journal of Glass Science and Technology Part B**: v. 46, n. 2, p. 67-71, 2005.

NALIN, M.; RIBEIRO, S. J. L., MANZANI, D.; GONÇALVES, R. R.; POIRIER, G.; MATOS, C. J. S.; CASSANGES, F. C.; MENDONÇA, R. C.; BONI, L.; MISOGUTI, L.; MALTA, O.; LEDEMI, Y.; MESSADDEQ, S.; MESSADDEQ, Y. Glassy materials and light: part 1. **Química Nova**, v. 39, n. 3, p. 340-351, 2016.

OTO, M.; KIKUGAWA, S.; SARUKURA, N.; HIRANO, M.; HOSONO, H. Optical fiber for deep ultraviolet light. **IEEE Photonics Technology Letters**, v. 13, n. 9, p. 978-980, 2001.

PHILLIPS, C. J. **Glass, its industrial applications**. New York: Reinhold, 1960.

RAO, M. A Brief Introduction to Excimer Lasers: Fundamental Study. **International Journal of Advances in Pharmacy, Biology and Chemistry**, v. 2, n. 3, p. 533–536, 2013.

SKUJA, L.; HOSONO, H.; HIRANO, M.; KOICHI, K. Advances in silica-based glasses for UV and vacuum UV laser optics. **Proceedings of the SPIE**: the International Society for Optical Materials, v. 5122, p. 1-14, 2013.

VAN VLECK, J. H. The Dipolar Broadening of Magnetic Resonance Lines in Crystals. **Physical Review**, v. 74, p. 1168–1183, 1948.

VYDRA, J.; SCHOETZ, G. F. Improved all-silica fibers for deep-UV applications. **Proceedings of the SPIE**: the International Society for Optical Engineering, v. 3596, p. 165-175, 1999.

WANG, P.; LU, M.; GAO, F.; XU, Y.; HOU, C.; ZHOU,; Z. PENG, B. Luminescence in the fluoride-containing phosphate-based glasses: a possible origin of their high resistance to nanosecond pulse laser-induced damage. **Scientific Reports**, 2015. doi:10.1038/srep08593.

WELZ, B.; SPERLING, M. **Physical principles**: Atomic absorption spectrometry, 3rd ed. New Jersey: Wiley-VCH, 1998. 965 p.

WILLIAMS, R. T.; NAGEL, D. J.; KLEIN, P. H. Vacuum ultraviolet properties of beryllium fluoride glass. **Journal of Applied Physics**, v. 52, n. 10, p. 6279-6284, 1981.

ZARZYCKI, J. **Glasses and the vitreous state.** Cambridge: Cambridge University Press, 1991. 505 p.

ZOU, X.; ITOH, K.; TORATANI, H. Transmission loss characteristics of fluorophosphate optical fibers in the ultraviolet to visible wavelength region. **Journal of Non-Crystalline Solids**, v. 215, n. 1, p. 11-20, 1997.

ZOU, X.; TORATANI, H. Radiation resistance of fluorophosphate glasses for high performance optical fiber in the ultraviolet region. **Journal of Applied Physics**, v. 81, n. 8, p. 3354-3362, 2015.